NEUTRON SCATTERING STUDIES OF STRONG DYNAMIC CORRELATIONS IN UNCONVENTIONAL SUPERCONDUCTORS: LOOKING THROUGH THE HOUR-GLASS TO HYBRIDIZATION AND A SUPERCONDUCTING SPIN RESONANCE

NEUTRON SCATTERING STUDIES OF STRONG DYNAMIC CORRELATIONS IN UNCONVENTIONAL SUPERCONDUCTORS: LOOKING THROUGH THE HOUR-GLASS TO HYBRIDIZATION AND A SUPERCONDUCTING SPIN RESONANCE

By J. J. Wagman, Hon. B.Sc. Phys. M.Sc. Phys.

A Thesis Submitted to the School of Graduate Studies in Partial Fulfillment of the Requirements for the Degree Doctor of Philosophy

McMaster University DOCTOR OF PHILOSOPHY (2013) Hamilton, Ontario (Physics)
TITLE: Neutron Scattering Studies of Strong Dynamic Correlations in Unconventional Superconductors: Looking Through the Hour-Glass to Hybridization and a Superconducting Spin Resonance
AUTHOR: J. J. Wagman, H.B.Sc., (University of Toronto), M.Sc. (McMaster University)
SUPERVISOR: Professor Bruce D. Gaulin
NUMBER OF PAGES: ix, 102

Abstract

A series of neutron scattering studies of unconventional superconductors is presented. These measurements are split into two parts. The first part considers the purely magnetic scattering in low-doped $La_{2-x}Ba_xCuO_4$. This study is comprehensive and elucidates much of the doping and temperature dependence of the low energy magnetic scattering in this system. It also clearly demonstrates that two dimensional incommensurate magnetic order in this system forms at the expense of three dimensional commensurate magnetic order. The remainder of the thesis is concerned with characterizing and determining the physics underlying pronounced enhancements of the inelastic scattering found to exist at 20 meV at equivalent two dimensional magnetic zone centers in both $La_{2-x}Ba_xCuO_4$ and $La_{2-x}Sr_xCuO_4$. Arguments are presented to interpret these features as a result spin-phonon hybridization in 214 cuprate superconductors. The measurements also explore the temperature and doping dependence of these features, determining that the enhancements are largely insensitive to doping and only present parametric response at temperatures relevant for three dimensional magnetic order in this system. In addition, the first evidence for a superconducting spin gap in $La_{2-x}Ba_xCuO_4$ is presented. The implications of these findings are discussed.

Acknowledgements

Dedicated to Charles Wagman, Francine Sherkin, Anne Murray, Ruth Sherkin, Joe Sherkin, Birdie and Dana Doidge

This thesis has been seven years in the making. It would be impossible to properly thank everyone who contributed to this work: from scientific discussions to the love of family and friends and everything in between. I will endeavour to thank each person who played a role in enabling me to arrive at this point as best I can, though it is impossible to truly capture everything in a short acknowledgements section such as this.

First, I would like to thank my supervisor Prof. Bruce Gaulin. It has been 8 years since I met Bruce. I have always been truly grateful for his tireless support and guidance in our work together. He taught me all of the key experimental methodologies I routinely employ, the importance of interleaving scans, double checking that the spectrometer really can scan the whole range of angles, and the vital importance of being able to communicate via presentations and written publications. These are skills that I can cherish and benefit from for a lifetime, and for which I am grateful. Of course, I must acknowledge that without Bruce, I never would have known the delicious experience that is Big Ed's Pizza!

Second, I would like to thank my committee members: Profs. Graeme Luke and Maikel Rheinstadter. Your insights through our many conversations and committee meetings have been instrumental in guiding the direction and presentation of the results of this thesis. You were always encouraging and thought provoking.

Thank you to all my committee members and Prof. Gaulin for your edits and suggestions to all of the chapters and publications that comprise this work.

I next need to acknowledge and thank Dr. Gabe Devenyi. He created the original .tex files/templates for this thesis and provided instructions on their operation. I greatly appreciate all of his assistance and generosity.

I would next like to thank my friends/condensed matter physics colleagues who have been a tremendous support throughout my studies: Dr. Pat 'Clancy-pants' Clancy, Dr. Ed Taylor, Dr. Travis Williams, Dr. Adam 'Crazy Craczel' Aczel, Ms. Casey Marjerison, Cpt. Tim Munsie, Mr. Jonathan Gaudet and Prof. Jeremy P. Carlo. You have all been a tremendous help in my work and I truly appreciate all you have done.

This work would, of course, not have been possible without the help of Scientific Associates and Technicians of McMaster University, Oak Ridge, NIST and Chalk River. I would like to thank, in particular,

From Oak Ridge - Dr. Andrei Savici, Dr. Barry Winn, Dr. Garrett Granroth, Dr. Matt Stone, Dr. Douglas Abernathy, Dr. Jennifer Niedziela, Dr. Sasha Koleshnikov, Dr. Steven Nagler, Dr. Melissa Graves-Brookes, Dr. Lisa Debeer-Schmidt, and Mr. Todd Sherline.

From NIST - Dr. Jose Rodriguez, Dr. Chris Stock, Dr. Yiming Qiu, Dr. Yan Zhao, Dr. Jeff Lynn, Dr. Daniel Parshall and Prof. Collin Broholm.

From McMaster - Dr. Hannah Dabkowska, Dr. Antoni Dabkowski, Mr. Meric Kiela, Mr. Paul Kiela, Mr. Jonathan Gaudet and Dr. Jim Garrett.

From Chalk River - Dr. Zin Tun and Dr. Zahra Yamani.

I would now like to thank my friends for being there for all the years that I worked on this thesis, tireless friendship and support, and more.

Among my friends, I need to thank Mr. Nick 'Powerman' Concepcion, Mr. Jon 'Dry Loop' Gold, Mrs. Irene Passos-Gold, Mr. Jono Elias, Sgt. Dr. Matt 'Zarbon' Minnick, Mr. Ben Jackel, Mrs. Margaret Jackel, Dr. Diana Glennie, Ms. Sarah McNeil, Mr. Andrew Parker, and Mr. Bram 'Crazy-Pants' Smagalla. Be it introducing me to Dungeons and Dragons, helping whenever you can, playing sports with me, teaching me how to swing a sword, or just generally being awesome, thank you so much for everything.

I would now like to take the opportunity to thank my Family.

First, I would like to thank my family I have joined by marriage: Mark 'Marko-Man' Doidge, Viki 'Mamush' Doidge, Ashley (Dashley) Doidge, Ima Gabay and Charlie Doidge. I can always count on you to be a highlight to the week and to bring a huge smile to my soul. You are the warmest, kindest and most genuine people I know. I cannot wait to become a member of your family!

I would now like to thank my always-family: Mom (Francine), Dad (Charles), Anne, Boo-Boo (Ruth), Zaidy (Joe) and Birdie. You have been there for me since the very beginning. From taking me to and from school, helping me with my homework (including this thesis), and being the best family I could ask for. I dedicate this thesis in part to you. Extra special thank you to my Dad who proof-read both of my theses!

Lastly, but as far from least as can be, I want to thank my wife Dana. You are my bescharet. I look forward to all the years we will have together, and thank you for all

the years we have had so far. Thank you for inspiring me to always reach higher. You brighten every day and, like with my Dad, I greatly appreciate all your help in proof reading this thesis. I dedicate this thesis also in part to you.

Thank you all.

Contents

List of Figures

Part I

Experimental Methods

Chapter 1

Introduction to Neutron Scattering

1.1 Introduction

In this chapter, the underlying principles of unpolarized neutron scattering is outlined. These concepts are well motivated by a number of different texts including G. L. Squires. *"Introduction to the Theory of Thermal Neutron Scattering"*. Dover Publications, 1978 and G. Shirane, S. M. Shapiro, and J. M. Tranquada. *"Neutron Scattering with a Triple-Axis Spectrometer"*. Cambridge University Press, 2002 and J. J. Wagman. *Neutron Scattering Studies of Underdoped Single Crystal* $La_{2-x}Ba_xCuO_4$. McMaster University, 2010. This chapter will borrow heavily on concepts raised predominantly in these three references. Where not specifically mentioned otherwise, the term "neutron scattering" refers to unpolarized neutron scattering.

It has been jestingly suggested by some that no system could be considered truly solved until a comprehensive neutron scattering experiment was performed. This is, of course, somewhat of a gross exaggeration. However, the jest was made in view of the tremendous importance neutron scattering has had to the study of condensed matter.

Neutrons are nucleons composed of quarks that possess a $S = \frac{1}{2}$ magnetic moment[4]. Consequently, the mediating interactions for neutron scattering are the nuclear (strong) interaction and magnetic interactions. This dual interaction nature leads to a plurality of distinctions from other scattering probes. These distinctions place the neutron advantageously as a robust complement of other probes of matter and often in a unique position to study physics not easily accessible otherwise.

Historically, the main limitation of neutron scattering in experimental practice is that neutrons are produced at low fluxes and high costs. For condensed matter research applications, neutrons are created at either reactors, like the NRU at Chalk River Laboratories, or spallation sources, like the Spallation Neutron Source at Oak Ridge National Laboratories. Indeed, compared with x-ray sources, neutron fluxes are quite low. Moreover, neutrons typically have low scattering cross-sections with most particles relevant to condensed matter systems. This doubly exacerbates the low flux issue. However, as will be seen, great progress has been made in regards to neutron detection. In fact, historical requirements for sample size have decreased over time.

Regardless of any limitations to their production, neutrons have proven to be an invaluable probe of many diverse systems. For example, in biological applications, x-rays tend to destroy the sample, while neutrons leave the sample intact and thereby enable detailed study. Further, by substituting deuterium for hydrogen in key sections

of a biological sample, neutrons can then distinguish these sections due to the contrast in the cross-sections of the neutron with hydrogen and deuterium[1]. Typically in the study of ceramic single crystals, such as those of interest to this thesis, hard x-rays are capable of penetrating on the order of micrometers into a sample. Neutrons, on the other hand, are instead able to probe the entirety of these same kinds of samples. This makes neutron scattering an excellent complement to x-ray scattering. Similar cases can be made for pairing neutron scattering with other probes, such as muSR and NMR, as well as for stand alone neutron studies.

Neutrons have three qualities that prove advantageous to the study of condensed matter systems.

The first quality is neutrons are able to scatter not only from magnetic moments (magnetic interaction) within a material, but also from the cores of nuclei (strong interaction). This enables neutrons to serve as probes in the study of a wide range of different problems.

The second quality is that the neutron itself lacks charge. This lack of charge allows the neutron, in most cases, to probe a sample in its entirety and not be strongly scattered by an electric interaction. This is not to say that neutrons are immune to absorption from certain materials. For example, Gadolinium presents challenges for neutron scattering studies due to its high absorption cross-section[2]. Despite this, neutrons can still scatter from the bulk of the material. Recent reports have demonstrated that neutrons can be used even in strongly absorbing systems, provided careful experimental design is employed[5].

The third quality is that the kinetic energy of neutrons typical for the study of solid state systems is on the order of meV. This is because the interatomic length scale relevant to such systems is on the order of Å, while many of the interesting excitation energy scales for such systems are on the order of meV. Because the neutron has a particular mass, it works out that to produce neutrons with the correct wavelength, IE order Å, requires neutrons with order meV kinetic energy. This makes neutrons a sensitive probe of both the lattice and magnetic dynamics of many systems, as well as any interaction between them.

Table 1.1: Basic Neutron Properties [1]

mass = 1.675 x 10^{-27} kg
charge = 0
spin = $\frac{1}{2}$
magnetic moment = -1.04 x $10^{-3}\mu_B$
kinetic energy of standard thermal neutron at room temperature = 25.3 meV

1.2 Key Neutron Properties

Table 1.1 displays many of the key properties of the neutron. The mass of the neutron, which, as discussed before, enables a number of advantages to using neutrons as a probe for condensed matter, is 939.573 MeV/c^2 [4]. Many experiments in neutron scattering use so-called thermal neutrons, which are thermalized with a moderator (a bath of heavy water or light water typically) that is maintained at room temperature. By then selecting an appropriate monochrometer - a device we will discuss shortly - these allow for the selection of neutrons whose incident energy are largely on the order of 15-30 meV.

1.3 Neutron Velocity Distributions

Neutrons may be treated as a non-interacting gas of particles. For the purpose of this discussion, we will treat these neutrons as a gas with a Maxwell-Boltzmann distribution of energies[6]. In many real-world implementations, the peak of this energy distribution is typically too high of an energy scale relative to the energy scale required for condensed matter experimental needs. To remedy this, neutrons are exposed to an appropriate moderator to thermalize the neutrons to a lower energy. For low energy experiments, such as the experiment carried out on the Disc Chopper Spectrometer (DCS) in this thesis, liquid hydrogen (O(25 K)) is used to thermalize the neutron gas to long wavelengths. As well, many facilities use thermal neutrons, which are neutrons that are thermalized with a room temperature source of heavy or light water. Thermal neutrons are fairly versatile and capable of studying an array of different systems. This is because thermal neutron wave-lengths are roughly commensurate with the typical interatomic distance in most condensed matter systems.

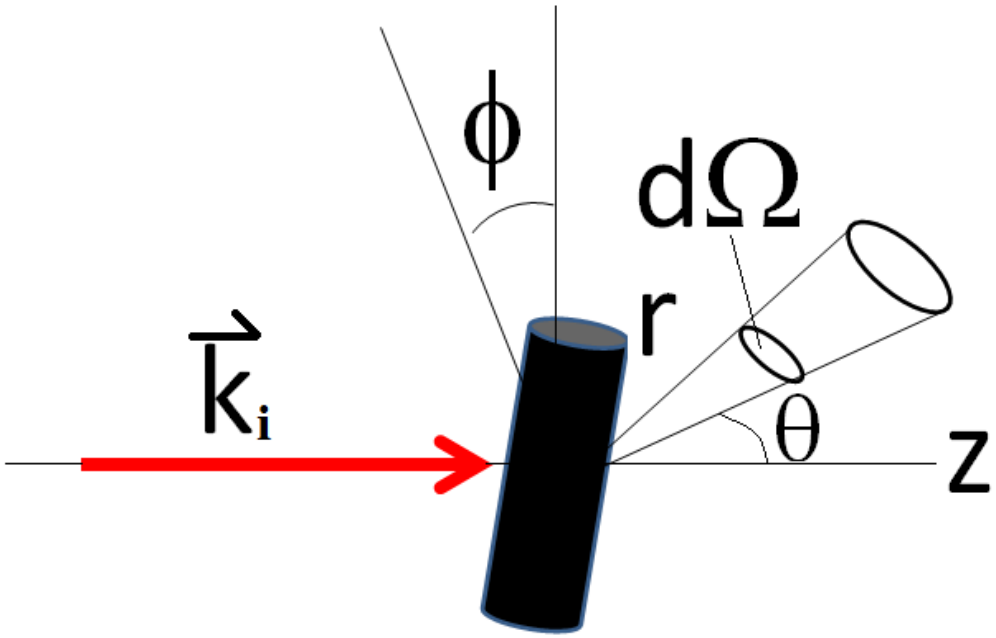

Figure 1.1: Scattering geometry of a neutron scattering experiment. The large cylindrical object is a representation of a sample in a beam of neutrons with incident wave-vector **k**. This is the same geometry depicted in G. L. Squires. *"Introduction to the Theory of Thermal Neutron Scattering"*. Dover Publications, 1978.

1.4 Nuclear Scattering

Fig. 1.1 is the geometry of a general neutron scattering experiment. Consider a monoenergetic beam. We will assume that we have a well collimated beam of incident wave-vector **k** and incident energy E. The neutrons will scatter to a neutron detector along an outgoing neutron wave-vector **k**' after hitting the large sample, represented as a black cylinder. To determine the final energy E', we can use two techniques, both of which will be discussed below. For the moment, assume that E' is known. We will solve the problem below using cylindrical polar coordinates for ease of analysis. This geometry is depicted in Fig. 1.1, which presents a real space view of the problem, and Fig. 1.2, which presents a reciprocal space view of the same problem.

The partial differential cross section in this geometry is defined as the number of neutrons scattered per second into $d\Omega$, with energy between E' and E + dE' and with wave-vector **k'**. To normalize this quantity for the size of the detector, the range of energies between E' and E' + dE', and the incident flux of neutrons, we will divide

the partial differential cross section by the solid angle, energy range and incident flux. The differential cross section is defined as the number of neutrons scattered per second into solid angle $d\Omega$. Explicitly,

$$\frac{d\sigma}{d\Omega} = \int_0^\infty (\frac{d^2\sigma}{d\Omega dE'})dE'. \tag{1.1}$$

The total cross section is then just

$$\sigma_{tot} = \int_(\frac{d\sigma}{d\Omega})d\Omega. \tag{1.2}$$

For simplicity, picture only those neutrons that scatter from an atomic nucleus in the sample. We employ the Born approximation and assume that the incident and outgoing neutrons are plane waves. Consequently, their state is defined by **k** and **k'**. We take the origin of this coordinate system to be the position of the atomic nucleus. We will also assume that the nucleus is a point source. Physically, this reflects that nuclei are miniscule by comparison to the size of an atom and, more importantly, the neutron wavelength. Experimentally, this turns out to be a good approximation. Scattering theory teaches that this scenario enables[7] the definition of a parameter b, called the scattering length. This parameter b is sensitive only to the nuclear structure of the nucleus and its spin state. In terms of b, the scattered wavefunction is

$$\psi_{sc} = -\frac{b}{r}e^{(ikr)}. \tag{1.3}$$

Defining ψ_{inc} as the incident neutron wavefunction and **v** as the velocity of the neutron, it can be shown that the number of neutrons passing through area dS per second is

$$vdS|\psi_{sc}|^2 = vdS\frac{b^2}{r^2} = vb^2d\Omega. \tag{1.4}$$

The incident flux Φ is then just

$$\Phi = v|\psi_{inc}|^2 = v. \tag{1.5}$$

Thereforem

$$\frac{d\sigma}{d\Omega} = \frac{vb^2d\Omega}{\Phi d\Omega} = b^2. \tag{1.6}$$

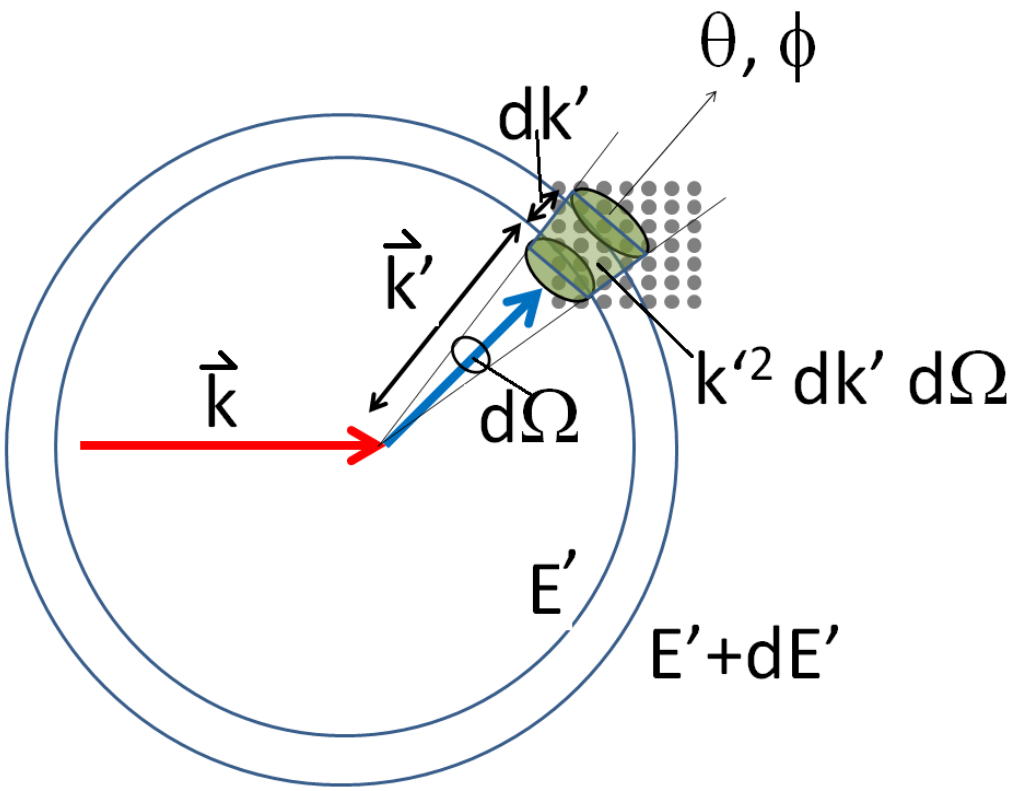

Figure 1.2: A second formulation of the geometry of a neutron scattering experiment. This representation is advantageous for the definition of new variables that are useful for calculating the number of momentum states in $d\Omega$. This quantity is defined as $\rho_{\mathbf{k}}$[2]. Shaded spheres represent points in the reciprocal lattice of a single crystal. The geometry shown is the same as a similar figure depicted in G. L. Squires. *"Introduction to the Theory of Thermal Neutron Scattering"*. Dover Publications, 1978.

Consequently, the total scattering cross-section is given by

$$\sigma_{tot} = 4\pi b^2. \tag{1.7}$$

It is worth noting if b is complex, then this would correspond to a negative number of scattered neutrons. This result corresponds to the case of neutron absorption by the sample.

Using Fig. 1.2, we can develop further the above formalism. Recall that Fermi's Golden rule tells us that[7]

$$(\frac{d\sigma}{d\Omega}) = \frac{1}{\Phi d\Omega}\Sigma W_{\mathbf{k},\lambda->\mathbf{k'},\lambda'}, \tag{1.8}$$

where W is the number of transitions per second of neutrons from their incident initial state to their final scattered state and the sum is over all $k\prime$ in dΩ. We define the potential from the crystal as V. Therefore,

$$\Sigma_{\mathbf{k'}ind\Omega} W_{\mathbf{k},\lambda->\mathbf{k'},\lambda'} = \frac{2\pi}{\hbar}\rho_{\mathbf{k}}| < \mathbf{k'}\lambda'|V|\mathbf{k}\lambda > |^2. \tag{1.9}$$

However, coherrent nuclear constructively interfering scattering occurs only if the difference between the incident and scattered wavevector, which is defined to be $\mathbf{Q}$, is a reciprocal lattice vector[8]. Normalizing the scattered flux to the incident flux

$$(\frac{d\sigma}{d\Omega})_{\lambda->\lambda'} = \frac{k'}{k}(\frac{m}{2\pi\hbar^2})^2| < \mathbf{k'}\lambda'|V|\mathbf{k}\lambda > |^2. \tag{1.10}$$

Energy conservation then requires that

$$(\frac{d\sigma}{d\Omega dE'})_{\lambda->\lambda'} = \frac{k'}{k}(\frac{m}{2\pi\hbar^2})^2| < \mathbf{k'}\lambda'|V|\mathbf{k}\lambda > |^2\delta(E_\lambda + E_{\lambda'} + E - E'), \tag{1.11}$$

where E_λ is the energy of a neutron of wavelength λ and E is the energy transferred to the crystal by the scattering event.

This last equation is the general form of the scattering cross-section relevant for nuclear neutron scattering. It can be subsequently be shown that

$$(\frac{d\sigma}{d\Omega dE'})_{\lambda->\lambda'} = \frac{\sigma_{coherent}}{4\pi}\frac{k'}{k}\frac{1}{2\pi\hbar}\Sigma_{jl}\int_{-\infty}^{\infty} < e^{(-i\mathbf{K}\bullet\mathbf{R}_l(0))}e^{i\mathbf{K}\bullet\mathbf{R}_j(t))} > e^{-i\omega t}dt \tag{1.12}$$

and

$$(\frac{d\sigma}{d\Omega dE'})_{\lambda->\lambda'} = \frac{\sigma_{incoherent}}{4\pi}\frac{k'}{k}\frac{1}{2\pi\hbar}\Sigma_{j}\int_{-\infty}^{\infty} < e^{(-i\mathbf{K}\bullet\mathbf{R}_j(0))}e^{i\mathbf{K}\bullet\mathbf{R}_j(t))} > e^{-i\omega t}dt \tag{1.13}$$

where

$$\sigma_{incoherent} = 4\pi(< b >)^2, \sigma_{incoherent} = r\pi(< b^2 > -(< b >)^2). \tag{1.14}$$

In the following sections, we will consider the case of purely magnetic scattering. A similar analysis for inelastic lattice scattering would yield that the differential cross-section for one phonon processes in a Bravais lattice is

$$\frac{d\sigma}{d\Omega dE'_{\lambda->\lambda'}} = \frac{\sigma_{coh}}{4\pi}\frac{\mathbf{k}'}{\mathbf{k}}\frac{(2\pi)^3}{v_o}\frac{1}{2M}e^{-2W'}\sum_s\sum_{\mathbf{K}}\frac{(\mathbf{Q}\bullet e_s)^2}{\omega_s} < n_s{+}1 > \delta(\omega{-}\omega_s)\delta(\mathbf{Q}{+}q{-}\mathbf{K}), \tag{1.15}$$

where W' is the Debye Waller factor, which is related to deviations of a nucleus from a Bravais lattice position, e_s is propogation direction of a phonon mode, ω_s is the energy of a phonon, $< n_s + 1 >$ is the Bose factor, which will be described in the context of magnetic scattering later.

1.5 Magnetic Scattering

We now motivate the cross section relevant for magnetic scattering. The magnetic dipole moment is:

$$\vec{\mu}_n = -\gamma\mu_n\vec{\sigma} \tag{1.16}$$

where $\gamma = 1.913$, $\vec{\mu} \approx \frac{e\hbar}{2m_p}$[1]. It is important to note that the magnetic moment of an electron is greater than that of the nucleus. So, while one can measure the nuclear magnetic moment using neutrons, statistically speaking, typical magnetic neutron experiments are more likely to inform the observer on the electronic magnetic properties of the system. Rewriting the magnetic interaction operator to refer to the electron:

$$\vec{\mu}_e = -\gamma\mu_B\vec{s} \tag{1.17}$$

where we take the spin state of the electrons to be $\vec{s}$. We label the electron momentum as $\vec{p}$. The spin magnetic field follows from the electron dipole moment and the magnetic field that follows from the electron's momentum is given by the Biot-Savart law[9]. Putting these contributions together, it can be shown that the magnetic scattering potential is [1]:

$$V_m = \frac{\mu_0}{4\pi}\gamma\mu_N 2\mu_B\vec{\sigma}\bullet[\nabla\times(\frac{\vec{s}\times\hat{R}}{R^2}) + \frac{1}{\hbar}(\frac{\vec{p}\times\hat{R}}{R^2})] \tag{1.18}$$

Therefore the partial differential cross section for magnetic scattering is:

$$(\frac{d\sigma}{d\Omega dE'})_{\sigma\lambda->\sigma'\lambda'} = \frac{k'}{k}(\frac{m}{2\pi\hbar^2})^2| < \mathbf{k'}\sigma'\lambda'|V_m|\mathbf{k}\sigma\lambda > |^2\delta(E_\lambda - E_{\lambda'} + E - E') \quad (1.19)$$

Note that here we are switching from real space to reciprocal space. We now define the energy difference in the crystal *E-E'* as a quanta of energy $\hbar\omega$. This allows us to show that:

$$(\frac{d\sigma}{d\Omega dE'})_{\sigma\lambda->\sigma'\lambda'} = (\frac{\gamma\mu_0 e^2}{4\pi m_e})^2\frac{k'}{k}| < \sigma'\lambda'|\vec{\sigma}\bullet\vec{Q_\perp}|\sigma\lambda > |^2\delta(E_\lambda - E_{\lambda'} + \hbar\omega), \quad (1.20)$$

where

$$\vec{Q_\perp} = \Sigma_i e^{i\mathbf{K}\bullet\mathbf{r}_i}[\hat{\mathbf{K}}\times(\mathbf{s}_i\times\hat{\mathbf{K}} + \frac{i}{\hbar K}(\mathbf{p}_i\times\hat{\mathbf{K}})]. \quad (1.21)$$

Full details on all of these derivations can be found in G. L. Squires. *"Introduction to the Theory of Thermal Neutron Scattering"*. Dover Publications, 1978. Equation 1.20 determines the probability of pure magnetic neutron scattering. Here, the term 'pure' emphasizes that we are only considering scattering from spins that do not hybridize with any lattice degrees of freedom. This cross-section also includes both elastic and inelastic magnetic scattering processes.

It is useful to rewrite the differential cross-section where we encapsulate all information directly related to the underlying magnetic potential in a function called the scattering function S($\mathbf{Q}$,$\hbar\omega$). In other words, we will write[1, 2]

$$(\frac{d\sigma}{d\Omega dE'})_{\sigma\lambda->\sigma'\lambda'}\alpha S(\mathbf{Q},\hbar\omega,T). \quad (1.22)$$

We include T because the magnetic potential is, of course, temperature dependent. Again, all we have done is rewritten the interesting system dependent information, the terms dependent on the magnetic potential, into a single function. By measuring the scattered intensity across all energies and $\mathbf{Q}$, we are therefore mapping out this scattering function. The advantage of this formulation is that a number of interesting properties of neutron scattering can be derived more easily. However, it also allows for a simple interpretation of a measured scattered intensity. It can be shown[2] that this scattering function can be broken down into two parts. Namely,

$$S(\mathbf{Q}, \hbar\omega, T) =< n+1 > \chi''(\mathbf{Q}, \hbar\omega, T), \tag{1.23}$$

where

$$< n+1 >= \frac{1}{1 - e^{-\frac{\hbar\omega}{k_B T}}} \tag{1.24}$$

The χ'' term is the so-called dynamic susceptability. This function is determined solely by the magnetic character of a scattering system and it is therefore this function that contains all interesting information about a scattering system. The remaining term is a thermal population factor, also known as a Bose factor. As can be seen, this function is determined solely by the excitation energy and the temperature, and therefore contains no detailed magnetic information about an underlying scattering system. Chapters 4 through 6 will use this formulation frequently. However, it must be remembered that these functions follow in their entirety from equation 1.20. χ'' and the Bose factor are a different way of formulating the same information conveyed by equation 1.20. Similar manipulations can be applied to nuclear and phonon scattering cross sections, as seen in equation 1.15.

1.6 Form Factors

From equations 1.15 and both 1.20 and 1.21, we see that magnetic scattering cross section is dependant on the component of the spin perpendicular to $\mathbf{Q}$, while for nuclear scattering the cross section instead depends quadratically on the phonon eigenvector component parallel to $\mathbf{Q}$. These terms arose from taking a Fourier transform of a relevant scattering potential. Each scattering potential is related to the spatial distribution of scatterers underlying the scattering potential. Physically, what we are encoding is that the cross section is related to a Fourier transform of the spatial distribution of scatterers in the system. Consquently, the greater the density of scattering sites in a lattice, the greater the likelihood that a neutron will be able to scatter. These Fourier transforms of the spatial distribution of scattering sites are called Form Factors. It is these Form Factors that caused the nuclear scattering cross section to go as $(\mathbf{Q} \bullet e_s)^2$ and the magnetic form factor to depend on the component of the spin perpendicular to $\mathbf{Q}$.

Physically, what the Form Factors are encoding is that differential cross sections

are related to the Fourier transform of some particle-particle correlation. In phonon scattering, the neutron strikes a nucleus and this causes energy to be transfered between nuclei via Coulomb forces. As this interaction is of a similar nature to one billiard ball striking another, it is not surprising that the phonon form factor is related to the component of $\mathbf{Q}$ parallel to the phonon eigenvector. For magnetic scattering, the correlations exist over larger distance scales and employ a, relative to the strong force, long range Coulomb interaction. This is why the magnetic Form factor is strongest at low $|\mathbf{Q}|$.

1.7 Distinguishing Magnetic and Nuclear Scattering

Experimentally, we only measure the number of neutrons that scatter into a particular solid angle and which also transfer a particular quanta of energy to the crystal. In other words, it is impossible to distinguish between magnetic and nuclear scattering from a measurement of a sample at a single point in $\mathbf{Q}$ and energy; it can even be difficult to distinguish between magnetic and structural scattering from a series of measurements at several points in $\mathbf{Q}$ and energy.

There are three commonly used methods that in practice aid in determining if a particular neutron scattering signal is magnetic or nuclear scattering.

The first method is to appeal to complementary information from other measurements. For example, if it is known from x-ray scattering that there is a structural transition only at temperature T_x, and one observes in a neutron experiment a phase transition at temperature T_N, as indicated by the onset/destruction of Bragg peaks at a temperature T_N then it is clear that the phase transition is not structural and is likely magnetic.

The second method is flows from the distinct $\mathbf{Q}$ dependences of magnetic and nuclear inelastic scattering. Again, for magnetic scattering, the neutron couples to the component of a magnetic moment that is **perpendicular** $\mathbf{Q}$ while for inelastic nuclear scattering, or phonon scattering, the neutron instead couples to the component of the phonon wave-vector that is **parallel** to $\mathbf{Q}$. Therefore, it is possible to distinguish between inelastic nuclear and magnetic scattering from these distinct $\mathbf{Q}$ dependencies of the scattering.

The third method is to measure the same signal in equivalent Brillouin zones of different $|\mathbf{Q}|$. This is because, again, the inelastic magnetic and nuclear scattering possess different Form Factors. As discussed, the magnetic form factor is concentrated at low $|\mathbf{Q}|$, hence the magnetic scattering cross section is most intense at low $|\mathbf{Q}|$. For phonon scattering, the Form Factor instead goes as $|\mathbf{Q}|^2$. Therefore, by observing the $\mathbf{Q}$ dependence of a scattering feature in different Brillouin zones, it can lead to an intuition of the underlying magnetic or nuclear nature of a scattering feature.

In the event that these different techniques are unable to distinguish between nuclear and magnetic scattering features, which can occur for complex systems with multiple phonon modes and complex magnetic interactions in a region of interest, one can also appeal to polarized neutron scattering measurements, as well as other techniques. However, a discussion of such methods is beyond the scope of this thesis. This is because it turns out that at the time of the publication of this thesis there exist no polarized neutron scattering apparatus configured to probe the features of interest to this work. While work is underway at present to remedy this state of the art, it is expected that this new suite of polarized neutron scattering spectrometers will not be ready for polarized neutron scattering experiments relevant to the features presented in this thesis until at least 2016, if not beyond.

1.8 Triple-Axis Instruments

Developed by Bertram Brockhouse, a Canadian physicist from McMaster University, the triple-axis spectrometer is a key measurement apparatus in neutron scattering today. The three axes are defined by a monochrometer axis, an analyzer axis and a sample rotation axis. The monochrometer and analyzer axes house single crystals with well known structures. Each crystal can be rotated so that when used in conjunction with Bragg's law[1], these crystals enable selection of a particular neutron wavelength for transmission to the sample or to a detector as appropriate. In other words, the monochrometer controls incident energy of neutrons on the sample and the analyzer controls the final energy of neutrons that reach a detector. Furthermore, using a coordinate system such that the monochrometer lies along the x-axis of a Cartesian plane, the detector position specifies $\mathbf{Q}$. Therefore, the monochrometer and analyzer enable complete control over both $\mathbf{Q}$ and the incident final energies of neutrons used to study a sample.

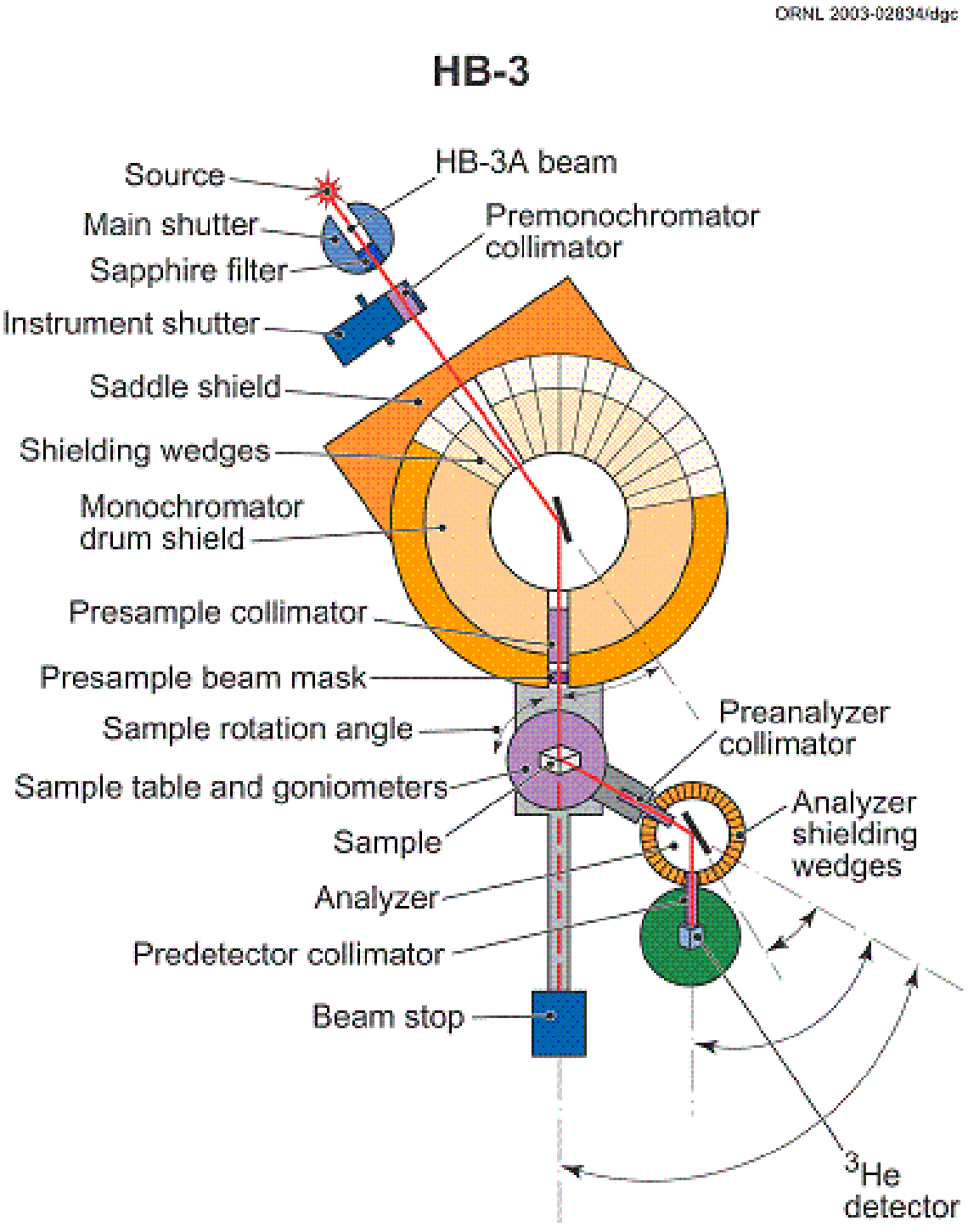

Figure 1.3: Triple-axis spectrometer HB3 at Oak Ridge National Labs [10]. Reproduced with permission from Dr. Adam Aczel.

A caveat to this design is that Bragg's law allows for harmonic wavelengths to contaminate a beam of incident neutrons, and can hence complicate analysis of a neutron measurement. Such harmonic contributions can be minimized by employing neutron filters, which significantly reduce higher order neutron contamination[2]. It is, therefore, always important in these kinds of measurements to consider results carefully, as higher order neutrons may still reach the sample and the detector.

An important assumption in this discussion is that the incident beam of neutrons is well collimated. While the above remarks apply equally well for a poorly collimated beam, imperfect collimation introduces experimental energy and momentum resolution effects. Such effects can broaden scattering signals to appear as broader than they should otherwise appear. Resolution effects are made additionally coarse by random errors inherrant in the position of spectrometer parts, the finite size of physical neutron detector, etc. For a detailed discussion of resolution effects, please see G. Shirane, S. M. Shapiro, and J. M. Tranquada. *"Neutron Scattering with a Triple-Axis Spectrometer"*. Cambridge University Press, 2002. For the present discussion, it is sufficient to be aware of such factors and to motivate that the signals presented in later chapters may be subject to resolution broadening.

In a triple-axis spectrometer, resolution effects can be reduced by the use of collimators. Collimators are comprised of a series of parallel plates of neutron absorbing materials. Consequently, collimators only allow neutrons whose trajectory lie to within some allowed angular range of a desired direction to pass. This practice dramatically reduces the flux of neutrons on the sample. This leads to the central trade-off problem of triple-axis neutron scattering - resolution vs. neutron flux.

An example of a triple-axis spectrometer is shown in Fig. 1.3. Depicted there is the HB3 spectrometer at Oak Ridge National Laboratory[10]. Spectrometers like HB3 can only view one scattering plane of a crystal at a time. This is because the spectrometer comprises only one detector placed in the horizontal scattering plane. Adding out of plane detectors can relieve this constraint. Measurements from a multi-detector setup are well suited, for example, in studies involving a large number of temperatures and magnetic fields. This is because such studies, by their nature, typically require one to measure a number of points in energy-reciprocal space at each field/temperature of interest.

1.9 The Time-of-Flight Spectrometers

Time-of-flight spectrometers (TOFS) have undergone a renaissance in recent years thanks to the advent of large neutron flux sources and modern computational technology. There are two main designs for these kinds of instruments, which will be discussed below.

1.9.1 Direct Geometry Time-of-Flight Spectrometers

This design of a TOFS is the kind of TOFS employed in this thesis. Fig. 1.4 shows an exemplary TOFS; in fact, this spectrometer was the spectrometer used in the measurements reported in chapter 4 of this thesis. The TOFS used in chapters 5 and 6 use similar principles, though the design of those implementations is more complex. Fig. 1.4 outlines the basic operating principles underlying both TOFS design.

1. A beam of “white" (which means polyenergetic) neutrons are directed towards the apparatus.

2. Prior to reaching the sample, the beam encounters a series of rotating neutron absorbing materials called choppers. Each of these choppers have a small channel cut into them. The purpose of these channels is to select the energy of all neutrons that reach the sample, as will be described in the following steps.

3. Neutrons are only able to proceed beyond the first chopper if and only if they arrive at such a time that the small channel of the first chopper is aligned with the incident neutron beam. If the neutrons arrive at any other time, they will be absorbed by the chopper. This step can be thought of as “defining the zero of a clock“, where the time at which the small channel of the first chopper becomes aligned with the incident neutron beam being defined to be time = 0.

4. Neutrons that pass the first chopper then reach a second chopper. The rotation speed of the second chopper is chosen so that the small channel of the second chopper becomes aligned with the neutron beam at a selectable time t. The selectable time is determined as follows. The distance between the first and second choppers are known and the time at which the neutrons passes the first chopper is also known. Again, the time at which the neutrons passes the first chopper is 0. Therefore, to allow only neutrons with energy $E = \frac{1}{2}mv^2$ to pass the second chopper at the selectable time, the selectable time t must be given by t = v * distance between chopper 1 and chopper

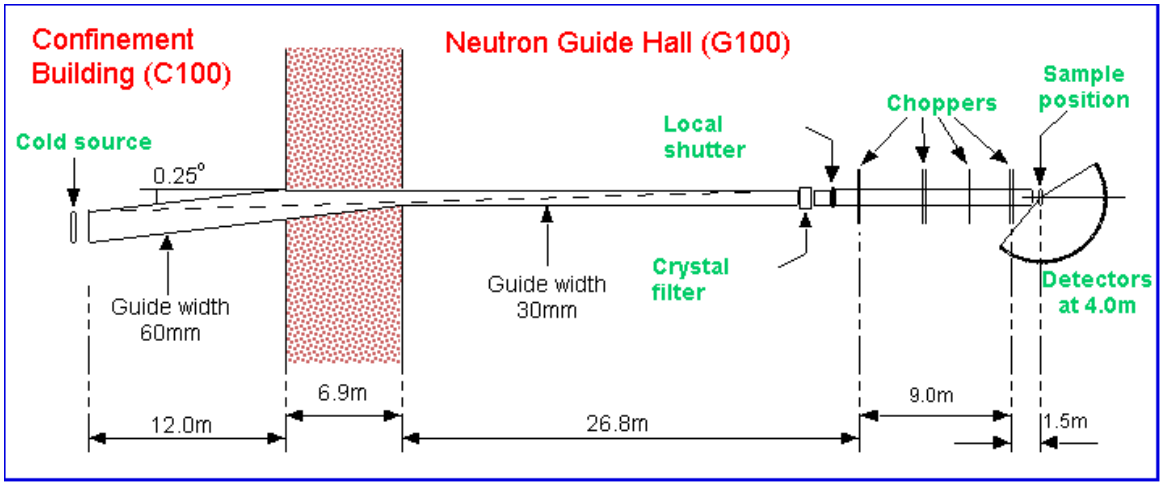

Figure 1.4: The DCS spectrometer at NIST[11]. Reproduced with permission from Dr. J. R. D. Copley.

2. In this way, the direct geometry TOFS can enable a user to define the energy of neutrons that are able to pass the choppers.

It should be noted that neutrons travelling at velocities such as $\frac{1}{2}$v will also be able to pass chopper 2. This effect can be eliminated in a number of ways.

One method is to moderate the distribution of neutron velocities in the beam of neutrons so that there exists only a small population of neutrons with velocity $\frac{1}{2}$v.

A second method is to tailor the distance between the neutron source and the first chopper appropriately. Since the distance between the first chopper and the neutron source is known, the times at which the small channel of the first chopper will aligns with the beam can be determined. One can therefore tailor the neutron source to the first chopper distance, so that no neutrons with velocity $\frac{1}{2}$v will be able to pass the first chopper. If the small channels are sufficiently small, this second method is applicable to a wide range of neutron velocities.

A third method would be to combine both of the above described methods.

5. Because both of the small channels of choppers 1 and 2 have a finite width and rotate to be in line with the incident neutron beam at calculable time intervals, it is clear that a number of neutrons with velocities close to but not equal to the velocity v will be able to pass both choppers. It is therefore optional to include additional choppers, as shown. By including more choppers, the range of velocities capable of passing the plurality of choppers is reduced, which thereby improves the resolution of the instrument.

6. The neutrons that pass all of the choppers are then able to reach a sample and scatter to a neutron detector. As with a triple-axis spectrometer, the sample lies at a known position. Note that a further consequence of the preceding steps is that the time at which the neutron reaches the sample is known.

7. The time at which the neutron detector detects a neutron is recorded.

8. Because the velocity of neutrons reaching the sample is known, the distance between the neutron detector and the sample is known, the time at which the neutron arrives is known and the position of the neutron detector is known, it is therefore possible to calculate all scattering angles and final energies of the neutron. This can be done as follows:

Determining the final energy of the neutron is equivalent to determining the velocity of the neutron. The neutron velocity is just the distance between the sample and the neutron detector divided by the difference in time between when the neutron reached the neutron detector and when the neutron reached the sample. Therefore, it is simple to determine the final velocity of the neutron.

Because the scattering angle of the neutron is known because the position of the neutron detector is known, the scattering angles of the neutron can be calculated. Using Bragg's law, $\mathbf{Q}$ is therefore calculable as it would be in a triple-axis measurement.

As a side note, steps 1 through 5 above are also employed by traffic lights in the City of Hamilton to regulate traffic speeds. When driving, if a driver arrives at a first green light and proceeds to drive at the speed limit, the driver is ensured that each subsequent light they pass will also be green for the same reasons that the velocities of neutrons reaching the sample are known for the above method.

It should also be noted that while instruments like DCS have a large number of neutron absorbers, called choppers, instruments at spallation sources can operate using fewer choppers. This is because spallation sources produce neutrons in pulses. This pulsed beam nature enables a definition of a $t = 0$ using the time of production of the neutron pulse in much the same way as the first chopper defined a $t = 0$ above. As a result, the function of the first chopper is provided by the pulsed nature of the neutron source itself, which obviates the need for a larger number of choppers.

Modern direct geometry instruments typically employ a large array of detectors. It is, of course, possible to use large detector arrays with triple-axis instruments as well. However, the fact that neutrons arrive at a sample at a controlled time enables large detector arrays to be used to their fullest potential. Examples of such instruments are

those used in reported measurements described in chapters 4 and 5 of this thesis.

Generally in neutron scattering measurements, as should be clear from the preceding triple-axis and TOFS discussions, detector positions, combined with knowledge of the neutron's energy transfer, define **Q**. However, while an analyzer crystal in a triple-axis measurement allows only one final energy to be measured at a time, energy measurements in direct geometry TOFS are equivalent to time measurements. Therefore, direct geometry TOFS are operable to detect ALL neutrons that scatter from a sample. Consequently, using a large detector array enables TOFS to measure both a large number of excitation energies simultaneously over a range of reciprocal space.

This ability to detect all scattered neutrons of all energies enables an interesting advantage of direct geometry TOFS - the production of four dimensional data sets. This can be obtained as follows. A three dimensional position in **Q** can be defined by the position of the detector (which gives two degrees of freedom), and an angle between the crystallographic planes of the sample and the incident neutron beam (which gives a third degree of freedom). This latter degree of freedom is controlled by rotating the sample and is often called the sample rotation angle. Because a TOFS can capture neutrons of all scattering energies in a single observation, by using a two-dimensional detector array, and by also controlling a sample rotation angle during an experiment, a direct geometry TOFS measurement can measure a kinematically accessible range of **Q** and energy in one map. i.e., one can map all of the kinematically accessible 4 dimensional energy-reciprocal space in a single set of measurements!

It should be noted that in such a 4 dimensional map, the dominant contributions to loss of **Q** resolution derive from collimation, and resolution broadening which is known to arise from the single crystal rotation protocol itself. This technique is therefore well situated for comprehensive explorations of materials at the expense of **Q** resolution. Today, many researchers will iterate between performing a first TOFS measurement and a triple-axis measurement to efficiently determine all the interesting physics in a system with the triple-axis measurements enabling detailed studies of particular features of interest.

1.9.2 Indirect Geometry TOFS

This type of spectrometer is an alternative to the direct geometry instruments from the previous subsection. This kind of spectrometer was not employed in this thesis.

Unlike direct geometry instruments which observe all SCATTERED neutrons in one measurement, indirect geometry TOFS probes a sample using all INCIDENT neutrons available. As a result, the operable flux of neutrons and range of distance scales in a sample system that can be probed are greater than monoenergetic spectrometers. An introduction to the technique and its operation will be provided here.

In these designs:

1. A **white** beam of neutrons is directed towards a sample.

2. After the neutrons scatter from the sample, the neutrons scatter towards a number of detectors. Each of these detectors has an analyzer crystal whose function is equivalent to that of the analyzer crystal in a triple-axis spectrometer.

3. The time at which a scattered neutron is detected is recorded.

Since all the distances in the spectrometer are known and because each detector only detects neutrons of a known energy, knowing the time at which an incident neutron reaches a known point in the apparatus means that the time-of-flight of the neutron can be calculated.

For example, in a spallation neutron based apparatus, the time of neutron production is known. This establishes the zero of a clock. Let us now call the time at which the neutron reach the sample position $t = T_S$ and the time at which the neutron reaches the neutron detector $t = T_D$.

Using an analyzer crystal ensures that the final energy of the neutron is known, which means that the neutron's final velocity is also known. Therefore the time needed for the neutron to travel from the sample to the detector is just the product of this final velocity and the distance between the sample and the neutron detector. Call this calculated time T_{Calc}. Therefore, because the neutron was produced at $t = 0$, the time needed for the neutron to reach the sample is T_D - $T_{Calc} := T_I$. This then shows that the initial velocity of the neutron must be the distance between the known point in the apparatus and the sample divided by T_I.

1.9.3 Direct Geometry TOFS Data Visualization

Returning to direct geometry TOFS, it was described above that a modern direct geometry TOFS can obtain 4 dimensional data sets in a single set of measurements. However, it is not hard to imagine that such a data set can present significant computational and analytical challenges. The full details of how to analyze such a data set requires a thorough discussion of how to computationally manipulate the immense

volume of data generated by such experiments. This would include discussions of how to encode the time-of-flight of each neutron, how to discount detectors that do not detect neutrons at a given time of flight, the importance of pointers implanted into each data measurement, and more. Such discussions of the detailed computer science are quite complex. However, how to analyze a four dimensional data set is of material interest to the present discussion.

The central theme of direct geometry TOFS data visualization, or DV, is data integration. Data integration is the method of summing data over a particular range, where the range is a range along a particular direction of energy-reciprocal space, and then normalizing the result by the magnitude of the range. Data integration can be used in four ways.

The first way of data integration is a volume data set integration. This involves integrating along one direction of energy-reciprocal space and presenting data from the remaining three directions of energy-reciprocal space. For example, if one were to integrate in energy from -1 to 1 meV, the resultant volume data set would be the kinematically accessible range of **Q** for elastic scattering mapped in the experiment. To present neutron scattering intensities at each point in **Q** for such an integration, one typically employs a colour scale to represent the quantity of neutrons scattered to a particular point in the volume data set. Volume data sets are useful for quick surveys of general trends in the data, but are computationally expensive to display.

The second way of data integration is a slice data set integration. This involves integrating along two directions of energy-reciprocal space and presenting data from the remaining two directions of energy-reciprocal space. For example, if one were to integrate in energy from -1 to 1 meV and from -0.1 to 0.1 reciprocal lattice units (R.L.U.) in the L direction, the resultant slice would be the elastic scattering of the HK plane. Slice data sets are a mainstay presentation method of DV. As with volume data sets, color scales are typically used to represent the quantity of neutrons scattered into a point in the slice data set.

The third way of data integration is a cut data set integration. This involves integrating along three directions of energy-reciprocal space and presenting data from the remaining direction of energy-reciprocal space. Presenting these data sets involves plots in the form of neutron scattered intensity vs. **Q** or energy, similar to a constant **Q** or constant energy scan with a triple-axis.

The fourth way of data integration is a data point integration. This involves

integrating along all four directions of energy-reciprocal space. The result of this data integration method is a number. Such a method can be useful, for example, if a data set presents a region of roughly uniform background scattering. This method can then be used as a means to determine the average background scattering value, which can be a useful measure of experimental backgrounds created by the adenda in a TOFS. Such background scattering tends to present as independent of both energy and **Q**. This fourth way of data integration is used in chapters 5 and 6 of this thesis.

The advantage of data integration, generally, is that it enables one to add together the measured intensities from several detectors together. Since the error in a neutron measurement goes, to first order, as the square root of the number of neutrons detected (i.e., counting statistics of independent scattering events), integration is a useful tool to use on weak signals that are diffuse in **Q** and/or energy.

For example, for a two dimensional magnetic system, the scattering along one direction of **Q** is isotropic, modulo the magnetic form factor. Integrating largely over this direction will add together more signal statistics from more detectors, improving the precision of the measurement. Simultaneously, if all other signals in the system are weak and three dimensional, such features will tend to average out and present as a weak background in the integration data set. Indeed, this methodology will be seen to be applicable to the materials studied in this thesis in chapters 5 and 6.

However, note that the hazard of large integrations is the assumption that all other scattering from sources other than some feature of interest are both a) less diffuse that the scattering from the feature of interest and b) of sufficiently low intensity that integration washes out the structure of the scattering from these other sources. Guidelines for the applicability of these assumptions lack precise quantification. However, if an integration range is too small, there may be insufficient statistics to gain meaningful information about the feature of interest. Consequently, the practice of modern neutron scattering requires a great deal of trial and error to identify appropriate integration ranges. The general trade-off in integration schemes is thus between integrating a sufficiently large quantity of scattering from the feature of interest against the drawback of integrating too much scattering from other sources.

Part II

General System Introduction

Chapter 2

Cuprate Superconductors

Decades after the discovery of superconductivity[12], and decades after the subsequent analytical formalism describing elemental and conventional superconductivity[13], the first high temperature cuprate superconductor was discovered[14]. This astonishing discovery took place nearly thirty years prior to this thesis. Yet, copper-oxide based superconductors, or 'cuprates', remain, in many ways, nearly as mysterious today as the day they were first discovered. At the heart of the study of these materials lies the question of what drives these materials to be the highest temperature superconductors ever discovered to date? Why are they so different than any other material?

However, it is not for superconductivity alone that cuprates have garnered such unprecedented scientific interest. Cuprates exhibit some of the most varied and rich physics of any system. Band theory suggests that cuprates should in fact all be at least reasonable conductors[15]. However, without the introduction of holes or electrons into the copper-oxide planes of these materials, cuprates instead prove to be strongly insulating[14]. In fact, the evolution from a three dimensional commensurate magnetically long-range ordered insulating undoped parent compound to a two dimensional incommensurate magnetically ordered superconductor, as obtained by the modest application of chemical doping[16] or oxygen annealing[17], is in of itself an attractive aspect and further introduces yet another avenue for departure from conventional superconductivity. Indeed, standard s-wave BCS theory[12], which is the theory by which we understand elemental/so-called conventional superconductivity, would suggest that we should not expect strong magnetism in any system with superconductivity. Cuprates stand in clear violation of this expectation. The plethora of differing magnetic orders and magnetic fluctuations that pervade each of the cuprate phase diagrams - plots, which in the present case, display the expected ground state magnetic order, transport properties and nominal spin excitations for a given cuprate as a function of both temperature and doping - alone merits rigourous and dedicated study.

To explain these states in proper detail, this introduction to cuprate superconductivity, magnetism and the foundations for this thesis' contributions to the field of magnetism in the prototypical cuprate $La_{2-x}(Ba, Sr)_xCuO_4$, is broken up into the following sections. The first section discusses typical phase diagrams relevant to this thesis as well as the general crystalline structure of these materials. The subsequent section will discuss the intertwining of magnetic order with superconductivity. An overview of the kinds of magnetic order in a few example cuprates will also be given. The next section will introduce magnetic excitations found in a number of different

cuprate systems and their potential relation to superconductivity. This section and the previous section directly relate to the first study of this thesis: Two Dimensional Incommensurate and Three Dimensional Commensurate Magnetic Order and Fluctuations in $La_{2-x}Ba_xCuO_4$[18]. The final section will consider the cutting edge issues in the field of magnetic excitations in cuprates - namely the dramatic enhancements of the **Q** integrated dynamic susceptibility of the reportedly 'purely magnetic' fluctuations found in a few cuprates, with particular focus paid to the enhancements observed in the sister materials $La_{2-x}Ba_xCuO_4$ (LBCO) and $La_{2-x}Sr_xCuO_4$ (LSCO).

2.1 General Phase Diagram

2.1.1 Crystal Structure

The high temperature crystal structure of 214 cuprates LBCO and LSCO, i.e., materials whose parent compound have a stoichiometric La:Cu:O ratio of 2:1:4, is shown in Fig. 2.1. The layered nature of this structure is pervasive to all crystal structures found in the cuprates, although the number of layers per unit cell can vary.

La takes on a [Xe] electronic configuration, entering into a 3+ charge state. O, conversely, enters into a [Ne] configuration with a 2- charge state. This leaves the task of charge balance to Cu, taking the configuration [Ar]3d9 and a charge of +2. This 3d9 valency makes Cu spin $\frac{1}{2}$. While a naive Hund's rule calculation would suggest a non-zero value of orbital angular momentum, crystal field effects split the d energy levels into the three lower t_2g bands and two upper e_g bands[20]. As a result of this splitting, orbital angular momentum is quenched in the depicted structure.

From Fig. 2.1, it can be further seen that the effect of Ba or Sr substitution at the La lattice site is to replace 3+ La with a 2+ dopant ion. These dopants remain in the same valence configuration as La 3+, and hence it is widely believed that the only contribution of doping is its effect on the valency of a portion of the Cu and O sites. Replacing La 3+ with a 2+ dopant requires that some Cu sites become +3 and hence have valence [Ar]3d8. It will be seen that this modification on the Cu site results in a plurality of modifications and changes to both the ordered and dynamic states of the cuprates. Interestingly, the introduction of additional oxygen atoms to the bilayer lattice of the material $YBa_2Cu_3O_{6+x}$ (YBCO) has been seen to reproduce the same effects as chemical doping in 214 materials[21]. This suggests that the rich

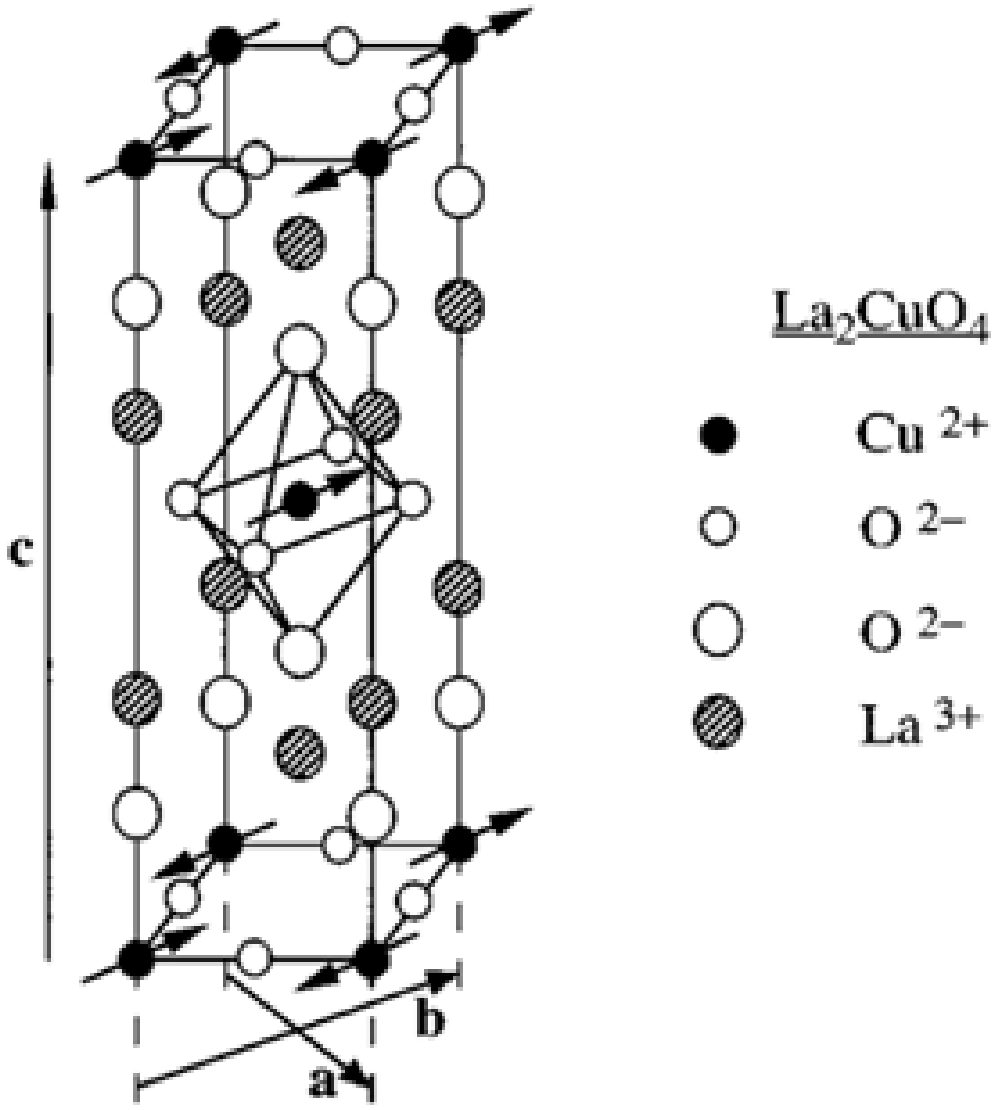

Figure 2.1: Crystal structure of La_2CuO_4[19]. Reproduced with permission from Dr. J. M. Tranquada.

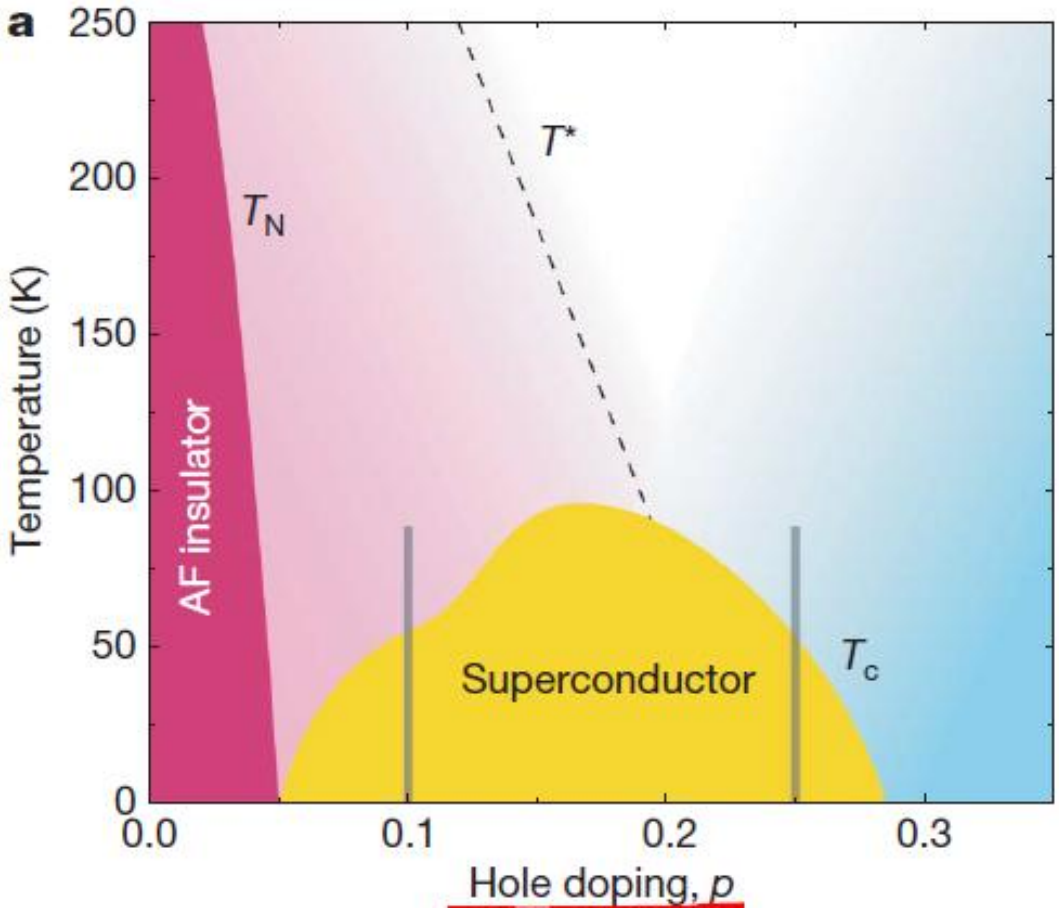

Figure 2.2: YBCO phase diagram[17]. Reproduced with permission from Dr. L. Taillefer.

physics of the cuprates is in some way determined by the concentration of holes in the copper-oxide layers.

It is common to summarize all the relevant transition information for a system in a phase diagram. A representative is shown for YBCO[17] and is reproduced in Fig. 2.2. This figure shows that upon increased hole concentration, the system evolves from a long range ordered antiferromagnet, with an order room temperature antiferromagnetic transition temperature T_N, to a system with no such long range order. Notice that at the same doping at which magnetic order is fully destroyed, a superconducting ground state is established. Further doping of holes leads at first to the enhancement of the superconducting transition temperature T_C. However, for x $\sim$ 0.16 - 0.19, T_C peaks, and then begins to fall. Eventually, for x $\sim$ 0.3, superconductivity is itself destroyed.

Please note that phase diagrams like Fig. 2.2 do not show a co-existence of any

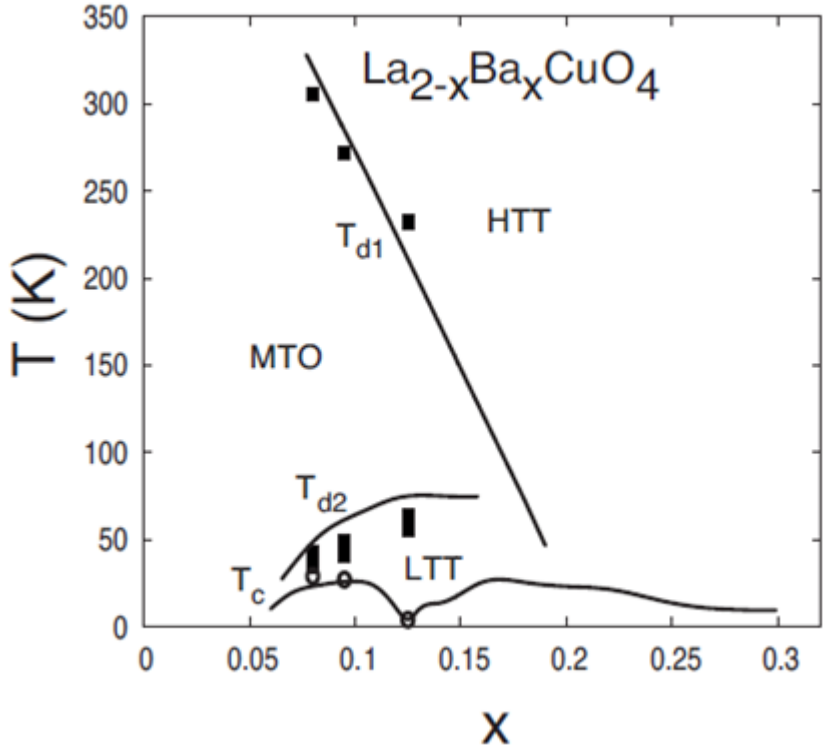

Figure 2.3: The phase diagram relevant to the crystal structure of $La_{2-x}Ba_xCuO_4$[22]. Reproduced with permission from Prof. B. D. Gaulin.

kind of magnetism with superconductivity. Such depictions lack precision. In fact, magnetic order can, and typically does, coexist with high temperature superconductivity. In materails like LBCO and LSCO, this magnetic order is not the long range three dimensional magnetic order of the parent compound, but instead a shorter ranged order. It is this second shorter ranged magnetic order with which this thesis is concerned.

In Fig. 2.4, another kind of Cuprate phase diagram is shown, this time relevant to LSCO. The high degree of similarity between the phase diagrams of LSCO and YBCO merits appreciation. However, there are a few notable departures. For one, in LSCO, three dimensional antiferromagnetic order persists only to x $\sim$ 0.02, with superconductivity forming around x $\sim$ 0.05. Note that this means that superconductivity occurs at a higher doping than the destruction of 3D antiferromagnetic order in LSCO, unlike in YBCO where 3D antiferromagnetic order persists until the onset of superconductivity. One should also note the inclusion of crystallographic phase transitions in this second phase diagram, as well as transport properties. Of greatest interest to this thesis is the addition of a small region labeled as a "spin-glass". Each

of these newly listed phases will be considered in turn.

It worth first noting the crystallographic phase transitions shown in Fig. 2.4. Starting at the highest temperatures, we see that the crystal structure of LSCO is tetragonal. More specifically, the crystal structure, relevant to both LSCO and LBCO, in this high temperature regime is a so-called high temperature tetragonal phase. The space group for this structure is $I4/mmm$[16, 23]. Upon cooling, a phase transition occurs and the crystal structure becomes orthorhombic with space group Bmab[24]. Interestingly, this breakdown in the equivalence of a and b lattice parameters is only a modest alteration of the crystallographic unit cell. It should still be appreciated that the transition involves a rotation of the basis lattice vectors by 45 degrees from the tetragonal basis vectors, and an appropriate multiplication of a and b is required. It should also be noted that this multiplication results from the rotation of the basis and can be pictured as encoding the switch from using nearest neighbor copper atoms as basis sites to next nearest neighbor copper atoms. While this may seem like a significant modification, the disparity between a and b is only slight and is typically on the order of less than 0.5%. This has led to many authors approximating all the crystal structures in LSCO with the high temperature tetragonal cell[25, 26]. Indeed, this practice extends equally well to LBCO, despite the presence of a third crystallographic phase, which is itself so slightly orthorhombic that the orthorhombicity can be difficult to detect[22].

The key commonality of these differing structures is that they are all layered with copper-oxide planes. Returning to YBCO for a moment, this system has a significantly larger and more complex bilayer structure than the monolayer structure of 214 cuprates. This structure is still well described, overall, by either a tetragonal or orthorhombic unit cell, with YBCO holding two full copper-oxide planes per cell, as opposed to only one plane per unit cell found in 214 cuprates. However, while this change in structure has notable impact upon the magnetic correlations of YBCO by way of inter-plane magnetic interactions[27], it appears that the key commonality YBCO shares with other cuprates is that it is comprised of copper-oxide layers. Interestingly, other high temperature superconducting systems like the pnictides are also layered, although drawing a direct analog based on structure alone between these systems is not so simple[15].

It is perhaps, then, not surprising that there exist a number of suggestions that the layered nature of cuprates is integral to the manifestation of high temperature

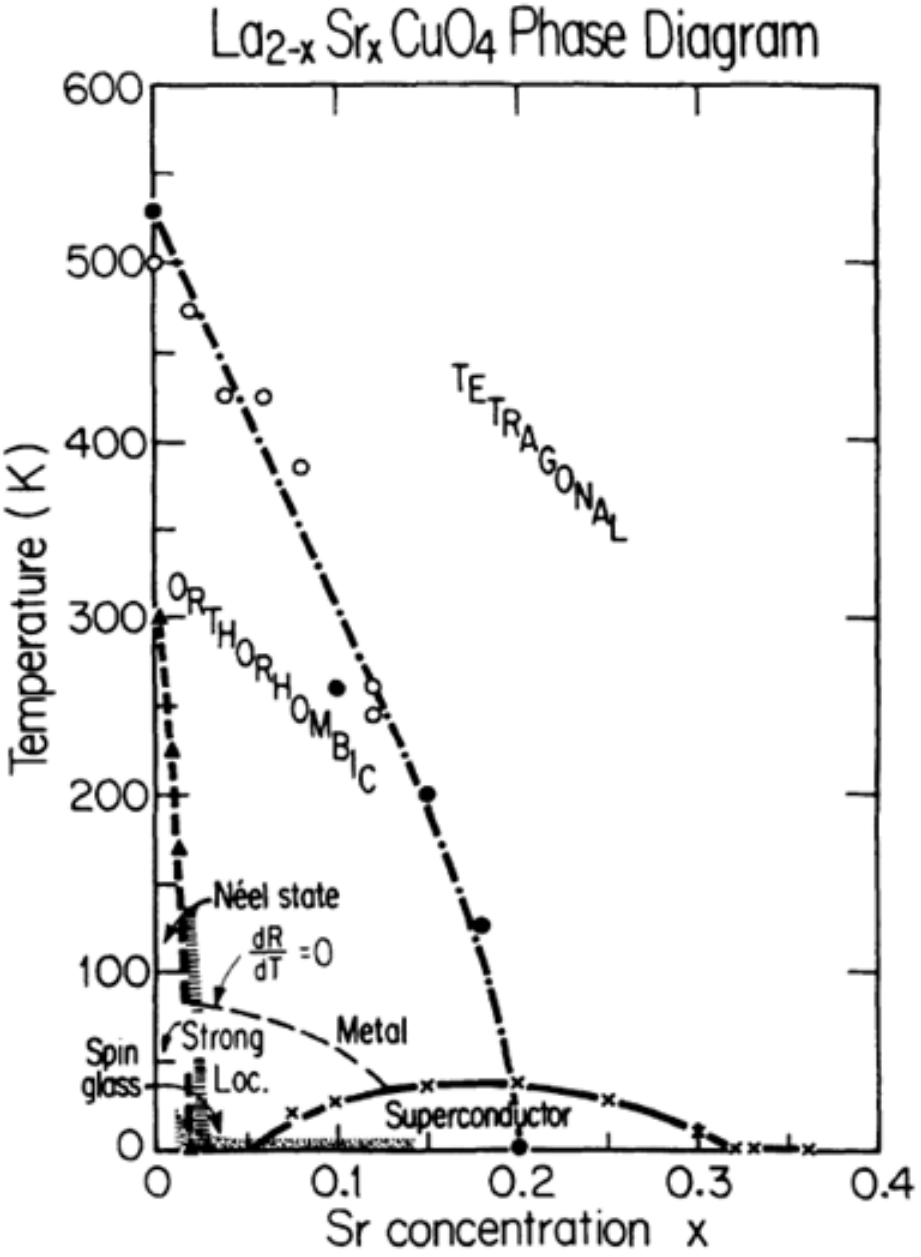

Figure 2.4: LSCO phase diagram[16]. Reproduced with permission from Dr. R. J. Birgenau.

superconductivity. It is therefore useful to consider some direct implications of these layered structures.

Interlayer separations of copper-oxide planes are significant, with separation distance scales between adjacent layers being large by comparison to the relevant distance scales within the copper-oxide layer. The typical ratio of a to c, using the tetragonal unit cell is approximately, 4:13. The consequence of this is that the *intra*-layer Cu-Cu distance is smaller than the *inter*-layer Cu-Cu distance. As a result, though interlayer ions ensure strong three dimensional lattice correlations, localized intralayer spins and charge carriers will experience stronger two dimensional **intra**-plane interactions. It is not surprising, then, that it appears that much of the interesting physics of cuprates are native to these copper-oxide planes. As such, one often considers the 214 cuprates to be like a series of decoupled quasi-two dimensional systems.

2.1.2 Basic Transport Properties

Transport in cuprates is dominated by strong electronic correlations. As mentioned earlier, band theory predicts that the undoped parent compounds of the cuprates should be reasonable metals[12]. In practice, the cuprate parent compounds are all insulators. This is a direct consequence of strong electronic correlations.

However, though conduction occurs for only modest hole concentrations, the nature of this transport is not that of a typical metal. Metals are expected to display quadratic resistivities as a function of temperature[20]. While such a phenomenology is observed for large hole concentrations beyond the superconducting ground state, for smaller dopings, resistivity measurements show linear parametric responses in many materials[21]. This has caused some authors to report that at these intermediate dopings cuprates behave as "strange metals"[16].

The most striking type of transport in cuprates, though, is of course high temperature superconductivity. It turns out that Cooper pairing still occurs in high temperature superconductivity[12]. This result can be understood qualitatively as follows. The elementary charge carriers in cuprates are electrons. As electrons are fermions, no two electrons can be in the same state at the same time, owing to the Pauli Exclusion Principle. However, superconductivity is a macroscopic occupation of a shared ground state. Paired electrons, on the other hand, are bosons, not fermions, and therefore do not suffer from Pauli exclusion and can thus participate in a shared macroscopic ground state[7]. As with conventional superconductors, transport within

this state occurs without resistance. Most importantly, the transition temperature into this state can be quite high - hence the name 'high temperature superconductivity'. There are, at present, no universally accepted theories that explain any of the transport properties described briefly in this subsection.

2.2 Magnetic Order in Cuprates

Magnetism in cuprates appears to be at the heart of understanding high temperature superconductivity. While conventional superconductivity, which is understood using BCS theory, would suggest that superconductivity is not compatible with magnetism[12], all high temperature superconductors possess robust magnetic order and fluctuations. It is clear that developing a thorough understanding of superconductivity requires a detailed understanding of cuprate magnetism.

Given the electronic configurations discussed above, spins in cuprates are due predominantly to Cu spins. However, recent work has shown that oxygen plays a key role as well, with $\sim \frac{1}{3}$ of the total ordered moment coming from the O site[28]. This is not so surprising a result. Given the typical distances between magnetic sites in the copper-oxide layer, one would expect that oxygen mediated superexchange should be a dominant contributor to magnetic interaction given the plaquet structure of the copper oxide layers[29]. Superexchange tends to favor antiferromagnetic interactions for the bond angles realized in cuprates, and indeed the predominant magnetic correlations seen in cuprates are antiferromagnetic[30].

For the parent compound, magnetic order is three dimensional and commensurate (3D C AF) with T_N in 214 Cuprates being on the order of room temperature, though oxygen off-stoichiometry can cause variations in the T_N realized in parent compound samples[16]. However, introduction of holes lowers T_N and leads to the onset of of two dimensional incommensurate antiferromagnetic order (2D IC AF)[16]. It may well be that 2D IC AF exists in the parent compound, although, as will be explored in chapter 4, it is expected that for this parent compound that the incommensuration of the 2D IC AF is 0Å. Consequently, observation of this state may not be possible[31].

In Fig. 2.4, 2D IC AF is referred to as a "spin-glass". While this labeling may be accurate, it is the implications of 2D IC AF beyond its 'glassyness' that are of greater importance. It should be noted that there also exists a narrow region where 3D C and 2D IC AF co-exist[32]. This coexistence will be demonstrated in chapter 4, with

the surprising further result that 2D IC AF forms at the expense of 3D C AF. It is also important to note that the 2D IC AF structure has been solved, and that the moments lie within the copper-oxide planes[26].

As a quick aside, in a neutron experiment, these 2D and 3D AF order appear with marked differences. From Bragg's law[33], any long range periodic correlations lead to constructive interference and therefore neutrons will be more likely to scatter into a restricted subset of possible solid angles. 3D correlations will restrict scattering angles in a full 3D space, as the correlations are periodic in all three spatial directions, resulting in a intense spot of scattering. 2D correlations will not exhibit any periodicity along some third spatial dimension, though within the other two spatial directions constructive interference will occur. As a result, 2D correlations appear as rods of scattering in a neutron experiment. In addition, everything else being equal, the scattered intensity from 2D correlations will likely appear less intense than the scattered intensity typically seen arising from 3D correlations. This is because a 3D Bragg spot condenses all the scattered neutrons into a tiny volume of reciprocal space while a 2D correlation from a similar magnetic origin will diffuse that scattered intensity isotropically along the entire length of the rod of scattering. As a result, 2D features can be harder to see. Moreover, 2D order is typically of a shorter range than 3D order. Furthermore, classical 2D systems with continuous symmetry should not attain true long range order by virtue of the Mermin/Wagner theorem[33]. It is therefore not unexpected that 2D order tends to be shorter ranged as compared to 3D order.

While the 3D C AF interactions are fairly well understood, the origin and role of the 2D IC AF remains a subject of some debate. 3D C AF can be understood naturally in terms of superexchange. For dopings where 3D C AF exists, the system is an insulator and all spins are localized. This then allows superexchange interactions to create a 3D C AF state. However, 2D IC AF pervades the phase diagram. One popular theory is that 2D magnetic order manifests because of so-called stripes[34, 35]. This theory suggests that the magnetic ground state forms in rivers of antiferromagnetic order with regions of magnetically-disordered material in between. Another popular suggestion involves so-called fermi surface nesting. Here, the antiferromagnetic correlations relate to neutron wave-vectors that reach from one region of the Fermi surface to another. Such a picture would also lead to incommensurate antiferromagnetic interactions[21]. However, even assuming that one of these two theories accounted for the 2D IC AF ground state, it is known that the magnetic ordering wave-vectors rotate by 45 degrees

at the same doping as the onset of superconductivity[36]. A microscopic connection between this last observation and the two above theories is at present lacking.

Regardless, 2D IC AF does not appear to be the cause of superconductivity. In fact, 2D IC AF appears to be competitive with superconductivity. Experiments in a magnetic field show that as superconductivity is suppressed by an external magnetic field, the effective T_N of 2D IC AF increases[37, 38]. Despite this, the issue of how the ordering wave-vector rotates at the onset of superconductivity still points to a common tie between 2D IC AF and superconductivity, although the precise origin of this correlation remains unknown.

2.2.1 Magnetic Fluctuations in Cuprates - Understanding the Hour-Glass

The diversity of magnetic fluctuations in cuprates is also rich. As there are numerous suggestions that it is the magnetic excitations in cuprates that themselves cause superconductivity[39], it is therefore important to understand these excitations in detail.

The magnetic excitations in cuprates are known to be two dimensional and, at least at low energies, occupying similar wave-vectors as the 2D IC AF[28, 30]. One might nominally expect that these excitations are a direct consequence of 2D IC AF order. This might be expected to be the case for a simple antiferromagnet[29], wherein the elementary excitations would be magnons that extend from magnetic Bragg positions. However, this does not appear to be the case. Studies of the integrated scattered intensity do not correspond to what would be expected for spin waves[28]. Further, there is also at present no work demonstrating a noticeable change to the dispersion or scattered intensity of the inelastic magnetic excitations as a result of the onset or destruction of magnetic order. Therefore, the magnetic excitations in cuprates cannot be understood as excitations of the 2D IC AF magnetically ordered state.

The magnetic excitations in cuprates take on the characteristic dispersion of an extended hour-glass, as shown in Fig. 2.5[40]. This hour-glass extends out to fairly high energies relative to typical magnetic energy scales relevant to solid state systems. At the top of the hour-glass, the excited states disperse out towards the Brillouin zone boundaries at around 200-300 meV[30, 41]. Interestingly, this highest energies of the hour-glass dispersion manifests as as fairly doping independent[42].

The hour-glass dispersion does turn out to be quite sensitive to doping. This sensitivity is seen best below 50 meV at the narrow waist of the dispersion. The energy of the hour-glass waist is referred to as energy E_{cross}[40]. E_{cross} is sensitive to hole concentration and scales linearly with doping over much of the phase diagram. It should be pointed out that for em x = 0, no hour-glass is observed[30]. This is often interpreted as meaning that $E_{cross} = 0$ at em x = 0.

Attempts to use spin-wave theories to model the magnetic dispersion appear to enjoy some success[30], though not complete success as discussed above. It is also interesting to note that regardless of the doping, spin-wave theory does a reasonable job reproducing the magnetic dispersions above E_{cross}. Further, the ordering wave-vectors above E_{cross} remain diagonal - meaning that the incommensuration lies along $< HH >$ - across the phase diagram[43]. This is suggestive of a common microscopic origin to the higher energy magnetic excitations in these materials.

Though the excitations may appear fairly consistent across the phase diagram, there remain a number of notable connections to doping dependent superconductivity. The most dramatic of these is the formation of a superconducting spin gap, which is observed in most cuprates. However, prior to this thesis, LBCO was a notable exception to this trend[19]. Indeed, reconciling the discrepancy between LBCO and LSCO remained an unsolved problem of the field for over a decade. The superconducting spin gap is seen in neutron scattering experiments as a suppression of the scattering below some threshold energy Δ[37, 42, 44] that exists only within the superconducting ground state.

However, this gap is not the only notable doping dependence. Just as the magnetic ordering wave-vectors rotate by 45 degrees at the onset doping of superconductivity, so too do the low energy magnetic excitations below E_{cross}[36]. It is observed that the dynamic correlation rotate from $\mathbf{Q} = (\frac{1}{2} \pm \delta, \frac{1}{2} \pm \delta, L)$ to $\mathbf{Q} = (\frac{1}{2} \pm \delta, \frac{1}{2}, L)$[45–47]. Furthermore, as E_{cross} increases, so too does the incommensuration of the low energy excitations. It is curious that below E_{cross} there is seen such sensitivity to doping while above E_{cross} there is instead seen largely doping insensitivity. An understanding of this distinction is at present lacking.

Another notable aspect of these hour-glass excitations is the strong enhancement of the scattered intensity at E_{cross}. The origin of this enhancement is well understood. The incommensurate nature of the 2D spin fluctuations imply that in a neutron experiment one can observe two peaks split evenly about the central $\mathbf{Q} = (\frac{1}{2}, \frac{1}{2})$ position. As

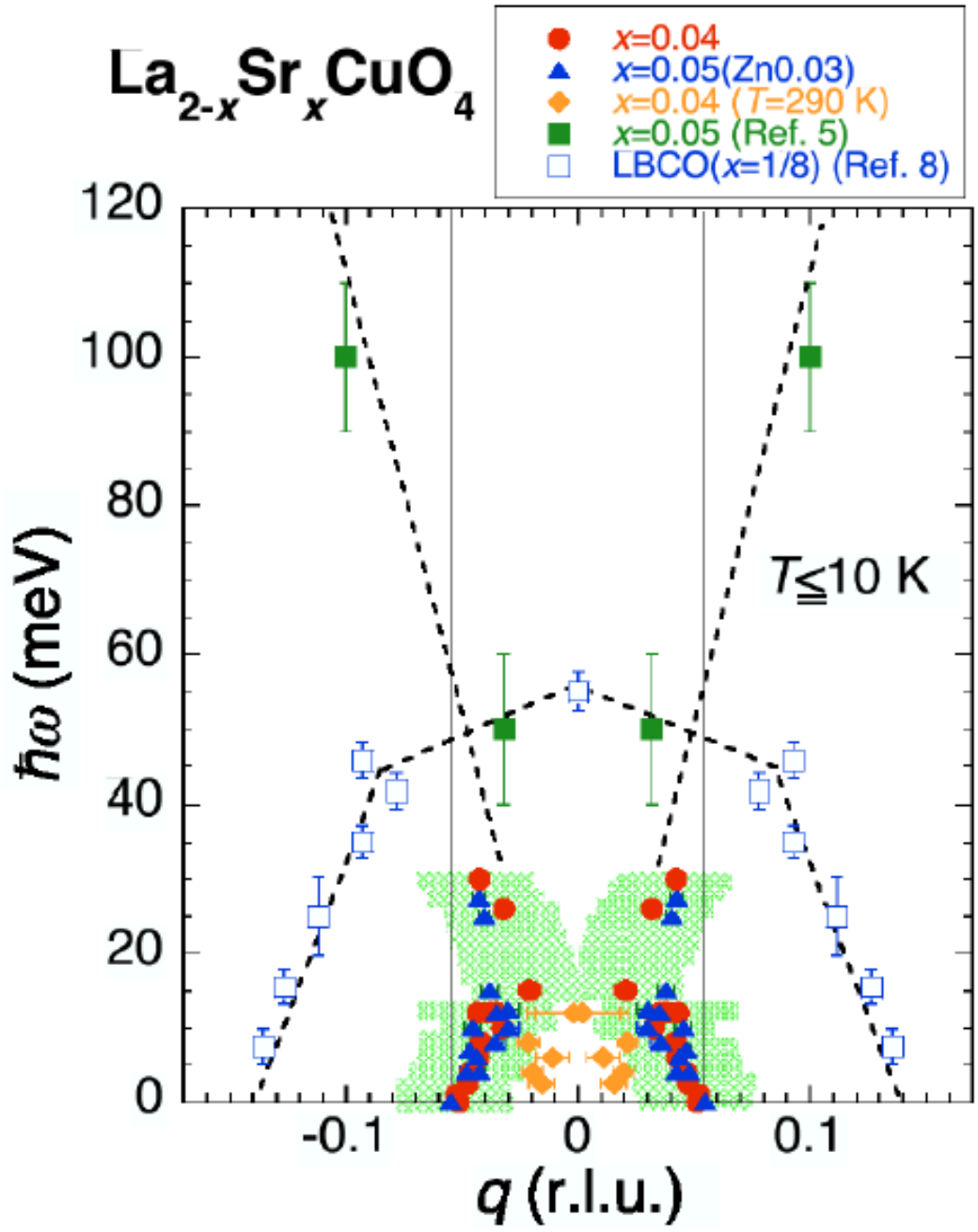

Figure 2.5: Dispersion of magnetic excitations in 214 cuprates[40]. Reproduced with permission from Dr. J. M. Tranquada.

the incommensurate splitting becomes small near E_{cross}, the two incommensurate peaks approach the same position. For sufficiently small separations, experimental resolution effects become important and, as a result, near E_{cross} resolution effects cause an integration of the scattered intensity from both incommensurate peaks. The result of this integration is a dramatic enhancement of the inelastic scattered intensity.

As a final note, the magnetic excitations in the cuprates become weaker with doping[48]. It is observed that scattered intensities become quite experimentally negligible near the overdoped regime of the phase diagram. However, recent work has suggested that this may be reflective of a transfer of spectral weight to other regions of reciprocal space[49].

2.2.2 Magnetic Fluctuations and Enhancements of the Integrated Scattered Intensity Beyond the Hour-Glass

More recent studies of the magnetic excitations in cuprates have centered on investigating the energy dependence of the **Q** integrated scattered intensity. Previously, such measurements were not feasible. However, a modern suite of newly developed facilities and instruments have enabled the cuprate problem to be revisited in a new experimental light.

A very interesting example of such a series of studies were performed on YBCO[50–52]. These studies produce data sets like that shown in Fig. 2.6. As seen, there are clear enhancements of the scattering near 20 meV. At present, these 20 meV feature have no detailed explanation. It has been presumed that the feature is magnetic in orign and related somehow to the superconducting spin gap[53]. Studies of the doping dependence of this feature suggest that the energy scale of this enhancement is strongly doping dependent[53, 54]. Further, it appears that the energy of this enhancement of the scattered intensity scales with T_C[52].

It is possible that this enhancement may be related to the superconductivity observed in these materials. If this is the case, then one would expect that a corresponding phenomenon should be observed in other cuprates as well. As it turns out, there are enhancements of the integrated scattered intensity in both LBCO and LSCO as well. Example measurements are shown in Figs. 2.7 and 2.8. Here, two enhancements are observed, with the higher energy enhancement peak being associated with the E_{cross} enhancement.

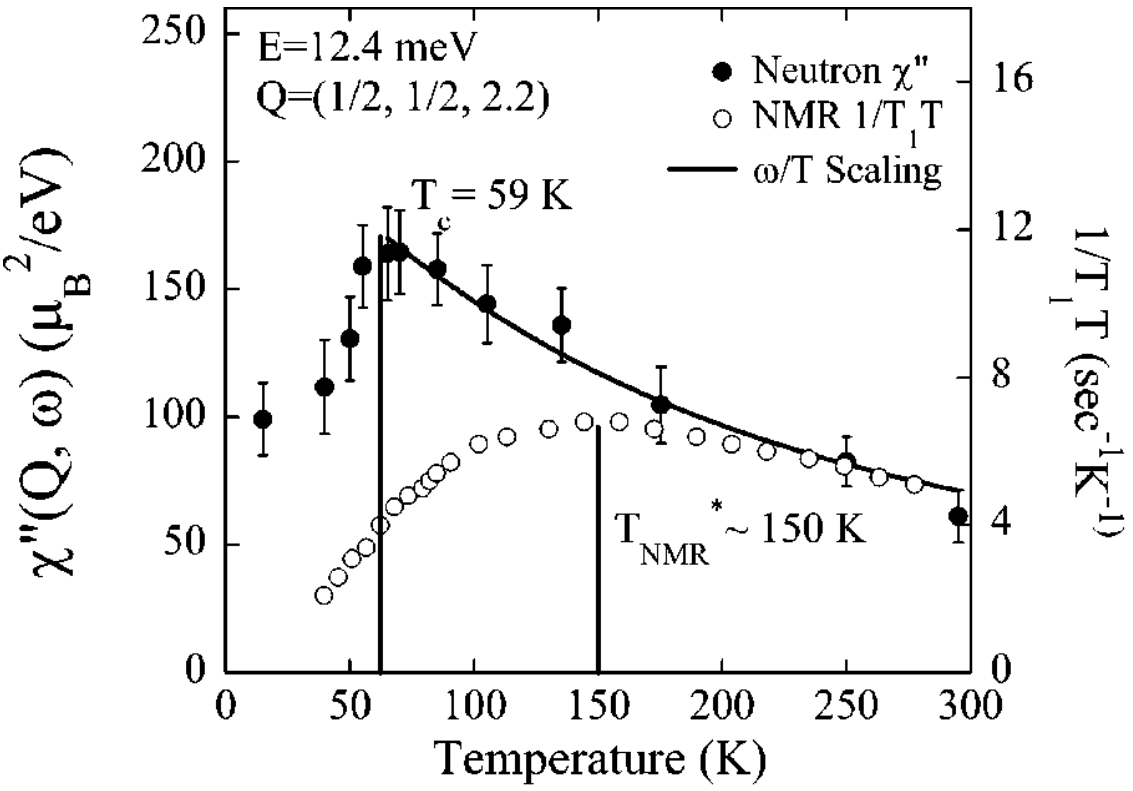

Figure 2.6: **Q** integrated intensity in underdoped superconducting YBCO, NMR data also presented but not discussed[51]. Reproduced with permission from Prof. C. Stock.

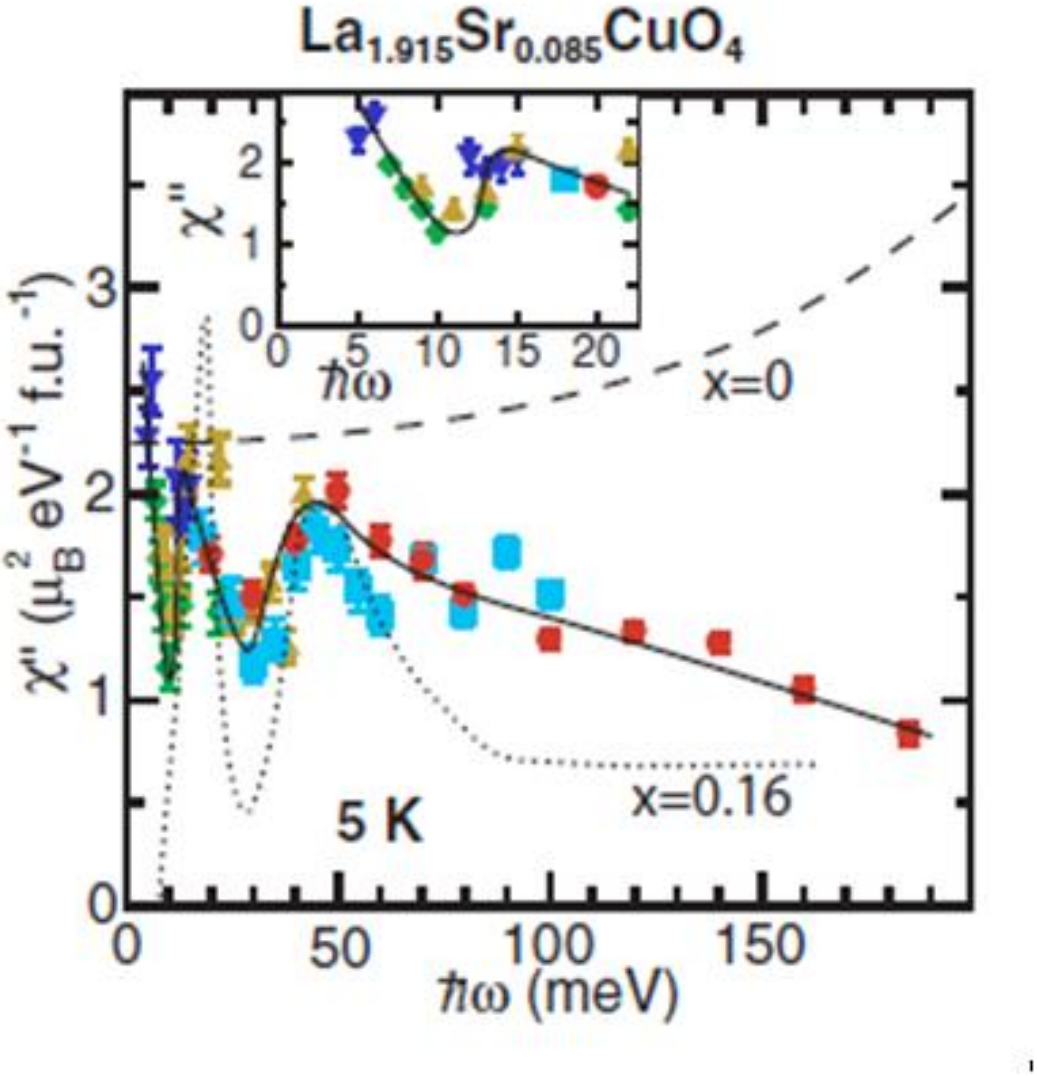

Figure 2.7: **Q** integrated intensity in underdoped superconducting LSCO[53]. Reproduced with permission from Prof. S. M. Hayden.

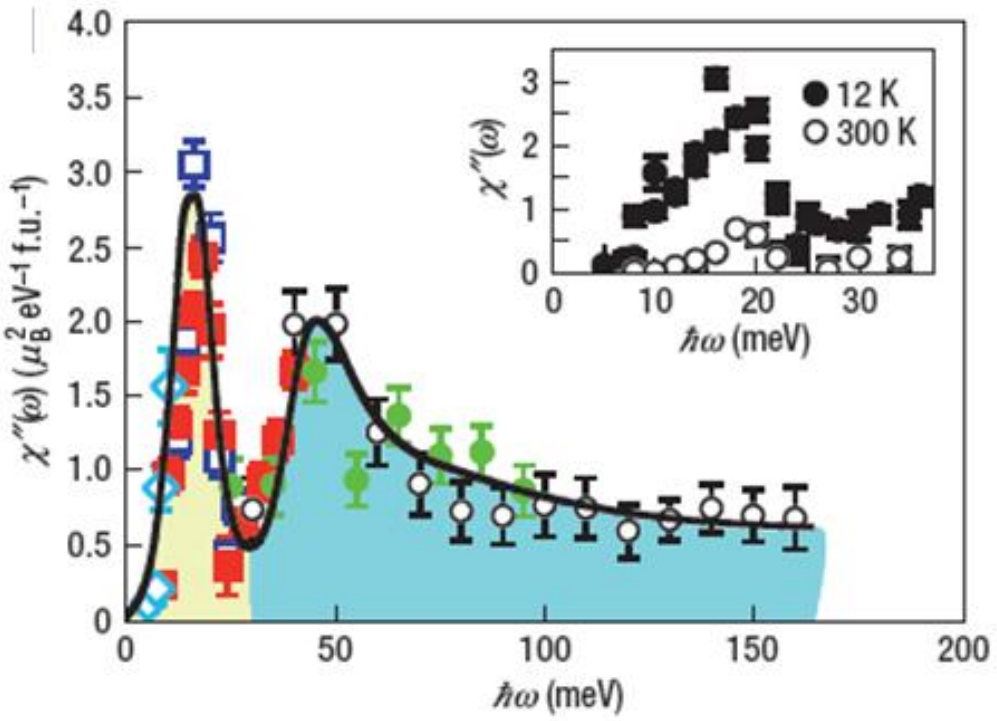

Figure 2.8: **Q** integrated intensity in optimally doped superconducting LSCO[54]. Reproduced with permission from Prof. S. M. Hayden.

Some doping and temperature dependent studies have been performed on these features in superconducting LSCO and LBCO. The temperature dependence of the enhancements in LSCO[53] show that at least for superconducting samples, these enhancements persist to temperatures outside of the superconducting ground state. However, in regards the doping dependence in LSCO and LBCO, there exists disagreement. Some authors have suggested that there exists a doping dependence for the excitation energy scale[44, 53, 54] while others report no such doping dependence with all excitations appearing at 20 meV[43, 55]. Resolving this discrepancy is of fundamental importance as if these newly discovered excitations are correlated to superconductivity, it will be important to determine the sensitivity of these features to doping.

At present, only a magnetic origin has been posited for these features. However, unlike the hour-glass itself for which the underlying Hamiltonian is well-understood[30], a full microscopic picture of the underlying magnetic interactions for these beyond the hour-glass enhancements remains lacking. Further, it should be noted that all previous reports are on superconducting materials, which begs the question of whether a similar phenomenon can be seen in a non-superconducting sample. Therefore, there exists a need for further study into the relation of these novel excitations to superconductivity, as well as a thorough characterization and understanding of these features at large.

Part III

Pure Magnetism in $La_{2-x}Ba_xCuO_4$

Chapter 3

Two Dimensional Incommensurate and Three Dimensional Commensurate Magnetic Order and Fluctuations in $La_{2-x}Ba_xCuO_4$

This chapter concerns work studying the low lying ($\leq 1meV$) magnetic excitations and magnetic structures found LBCO over a range of non-superconducting samples ($0 \leq x \leq 0.035$). Prior to this study, only large high quality single crystals of LSCO were available. This study presents this first in depth look at the LBCO. The reported measurements are therefore a window to determine the degree of similarity between LBCO and LSCO - a similarity that has been often assumed, but never explicitly demonstrated.

This report is also positioned to answer a never before resolved question. While it has been long assumed that 3D C and 2D IC correlations should coexist in 214 cuprates, no prior studies demonstrating this co-existence have been reported.

First, it is found that the magnetic structures and low lying excitations correspond with excellent agreement to previous reports for LSCO. This is not an unexpected result, as the two materials are isostructural and share identical electronic configurations. While such features are no guarantee of similarity, this result confirms that the driving physics of these magnetic excitations at low dopings is the concentration of holes introduced by doping.

It is also found that two dimensional and three dimensional magnetic order coexist for $0 \leq x \leq 0.02$. Further, it is observed that two dimensional incommensurate order comes at the expense of three dimensional order in samples where the two states are found to co-exist. This result is surprising, as one would naively expect from entropy considerations that higher dimensional order should typically occur at lower temperatures, as it is a more ordered state than a lower dimensional state. Regardless, the presumed co-existence of these features is now confirmed.

As this study involved time of flight neutron scattering techniques, we were also able to inform upon the low energy excitations in the system. We first found that the excitations correspond well to those reported in LSCO.

We also found a systematic depletion of the low energy dynamic susceptibility occurs with increased doping x. This appeared suggestive of a precursor to a superconducting spin gap for higher dopings. However, at the time of this publication, no such observation of such spin gap in LBCO has been reported.

Interestingly, we also found an apparent universally observed temperature dependence to the integrated dynamic susceptibility across this region of the phase diagram. It was found that a crossover behavior occurs for the magnetic excitations on a temperature scale consistent with the three dimensional ordering temperatures of the parent compound. This apparently universal temperature scale found for this cross-over in the excitations of this system below 1 meV strongly suggests a common origin to the magnetic excitations throughout the phase diagram.

To summarize these results, we construct a phase diagram based solely upon magnetic neutron scattering order parameter measurements. The result appears quite similar to superconducting phase diagrams reported for cuprates generally.

This work was published as J. J. Wagman, G. Van Gastel, K. A. Ross, Z. Yamani, Y. Zhao, Y. Qiu, J. R. D. Copley, A. B. Kallin, E. Mazurek, J. P. Carlo, H. A. Dabkowska, and B. D. Gaulin. In: *Phys. Rev. B* 88 (2013), p. 014412. G. Van Gastel, participated in all the measurements reported, including the Chalk River triple-axis measurements shown in Fig. 1, for which I was absent. He also collaborated with me in analyzing the elastic scattering data. K. A. Ross participated in the DCS measurements and prepared the phase diagram. Z. Yamani was the instrument scientist responsible for the C5 measurements. Y. Qiu and J.R.D. Copley were the instrument scientists for the DCS measurements. Y. Zhao, A. B. Kallin, E. Mazurek and H. A. Dabkowska grew the samples. J. P. Carlo assisted with data analysis of the C5 data. B. D.

Gaulin supervised all experiments, analysis and preparation of the publication. My contribution was to participate in all experiments but the C5 experiment, collaborate in the analysis of the elastic scattering data, take the lead role in analyzing all of the inelastic data and took the lead role in preparing the publication. This work was awarded the distinction of "Editor's Suggestion" by the American Physical Society.

PHYSICAL REVIEW B **88**, 014412 (2013)

Two-dimensional incommensurate and three-dimensional commensurate magnetic order and fluctuations in $La_{2-x}Ba_xCuO_4$

J. J. Wagman,[1] G. Van Gastel,[1] K. A. Ross,[1,2,3] Z. Yamani,[4] Y. Zhao,[3,5] Y. Qiu,[3,5] J. R. D. Copley,[3] A. B. Kallin,[1,6] E. Mazurek,[1] J. P. Carlo,[1,4] H. A. Dabkowska,[7] and B. D. Gaulin[1,7,8]

[1]*Department of Physics and Astronomy, McMaster University, Hamilton, Ontario, Canada L8S 4M1*
[2]*Department of Physics and Astronomy, Johns Hopkins University, Baltimore, Maryland 21218, USA*
[3]*National Institute of Standards and Technology, Gaithersburg, Maryland 20899-6102, USA*
[4]*Canadian Neutron Beam Centre, NRC, Chalk River Laboratories, Chalk River, Ontario, Canada K0J 1J0*
[5]*Department of Materials Sciences and Engineering, University of Maryland, College Park, Maryland 20742, USA*
[6]*Department of Physics and Astronomy, University of Waterloo, Waterloo, Ontario, Canada N2L 3G1*
[7]*Brockhouse Institute for Materials Research, McMaster University, Hamilton, Ontario, Canada L8S 4M1*
[8]*Canadian Institute for Advanced Research, 180 Dundas Street West, Toronto, Ontario, Canada M5G 1Z8*

(Received 29 March 2013; published 12 July 2013)

We present neutron-scattering measurements on single crystals of lightly doped $La_{2-x}Ba_xCuO_4$, with $0 \leqslant x \leqslant 0.035$. These reveal the evolution of the magnetism in this prototypical doped Mott insulator from a three-dimensional (3D) commensurate (C) antiferromagnetic ground state, which orders at a relatively high T_N, to a two-dimensional (2D) incommensurate (IC) ground state with finite-ranged static correlations, which appear below a relatively low effective T_N. At low temperatures, the 2D IC magnetism coexists with the 3D C magnetism for doping concentrations as low as ∼0.0125. We find no signal of a 3D C magnetic ground state by $x \sim 0.025$, consistent with the upper limit of $x \sim 0.02$ observed in the sister family of doped Mott insulators, $La_{2-x}Sr_xCuO_4$. The 2D IC ground states observed for $0.0125 \leqslant x \leqslant 0.035$ are diagonal, and are rotated by 45 degrees within the orthorhombic basal plane compared with those previously reported for samples with superconducting ground states: $La_{2-x}Ba_xCuO_4$, with $0.05 \leqslant x \leqslant 0.095$. We construct a phase diagram based solely on magnetic order-parameter measurements, which displays much of the complexity of standard high-temperature superconductivity phase diagrams discussed in the literature. Analysis of high-energy resolution inelastic neutron scattering at moderately low temperatures shows a progressive depletion of the very low-energy dynamic magnetic susceptibility as x increases from 0.0125 to 0.035. This low-energy, dynamic susceptibility falls off with increasing temperature on a scale much higher than the effective 2D IC T_N appropriate to these materials. Appreciable dynamic 2D IC magnetic fluctuations inhabit much of the "pseudogap" regime of the phase diagram.

DOI: 10.1103/PhysRevB.88.014412 PACS number(s): 75.25.−j, 75.30.Kz, 75.40.Cx, 75.40.Gb

I. INTRODUCTION

The 214 family of cuprates, $La_{2-x}Ba_xCuO_4$ (LBCO) and $La_{2-x}Sr_xCuO_4$ (LSCO), are among the most studied of the high-temperature superconductors (HTSs).[1–3] Most of this work has focused on $La_{2-x}Sr_xCuO_4$, which has been available in large, pristine single-crystal form for some time.[4] Although $La_{2-x}Ba_xCuO_4$ was the original HTS family to be discovered,[5] its study has been greatly restricted due to the difficulty of its single-crystal growth. These difficulties have now been largely overcome for relatively low doping levels: $x \leqslant 0.15$. While there are many similarities between the magnetic and superconducting properties of the two 214 families of HTSs,[6,7] there are also important differences. For example, a low-temperature tetragonal phase of $La_{2-x}Ba_xCuO_4$ exists for $0.05 \leqslant x < 0.15$,[8–10] and superconductivity is almost completely suppressed at $x = 0.125$, a phenomenon which is referred to as "the 1/8 anomaly."[11]

For HTSs, the parent, undoped compounds are Mott insulators which display three-dimensional (3D), commensurate (C), antiferromagnetic (AF) ground states.[12,13] This 3D C AF ground state is remarkably sensitive to the presence of mobile, doped holes, and is less sensitive to the presence of doped mobile electrons.[14] For hole doping, relevant to Ba in $La_{2-x}Ba_xCuO_4$, Sr in $La_{2-x}Sr_xCuO_4$, and oxygen in $YBa_2Cu_3O_{6+x}$, the 3D C AF ground state is very quickly destroyed.[15] This occurs, for example, for $x >$ ∼0.02 in $La_{2-x}Sr_xCuO_4$.[16,17] Upon further introduction of holes, a superconducting ground state is obtained for $x \sim 0.05$.[18,19] The superconducting T_C increases with increased doping and an optimally high superconducting T_C is achieved near $x \sim 0.17$.[20–22]

Two-dimensional (2D) incommensurate (IC) spin structures and dynamics, exhibited by samples with hole-doping concentrations beyond those that destroy the 3D C magnetic order, have been studied in several families of HTSs. Inelastic neutron-scattering studies are consistent with an "hour glass" dispersion, wherein low-energy spin excitations disperse out of IC wave vectors and merge or nearly merge at the C wave vector to form a resonant spin excitation.[23–30] At higher energies, the excitations disperse out from the C wave vector, before turning over near the Brillouin-zone boundaries.[23,31,32] Such a picture has been shown to be relevant even in the relatively low hole-doping regime of $La_{2-x}Sr_xCuO_4$, where the insulating ground state is characterized by "diagonal" IC spin order.[33]

The resulting phase diagrams for these families of HTS materials have led some observers to conclude that magnetism

and superconductivity are closely linked, as these ground states are either contiguous or almost contiguous to each other. In contrast, others have concluded that these ground states compete, as each inhabits a different part of the phase diagram. From either perspective, it is important that the microscopic magnetic properties be characterized and well understood across the phase diagram. Even in the underdoped, nonsuperconducting regime, for $x < 0.05$ in LBCO and LSCO, the magnetic phase behavior and properties change quickly with doping. This paper seeks to elucidate this evolution of magnetic properties in LBCO, using a variety of neutron-scattering techniques. We specifically report on the magnetic structure and dynamics of $La_{2-x}Ba_xCuO_4$ for doping levels $0 \leqslant x \leqslant 0.035$, and study how the 3D C magnetism evolves into 2D IC magnetism. We construct a phase diagram for $La_{2-x}Ba_xCuO_4$ based solely on magnetic neutron-scattering order-parameter measurements and show that it possesses much of the full complexity of conventional HTS phase diagrams based on magnetic and transport measurements. Finally, using time-of-flight neutron-scattering techniques, we report on low-energy 2D IC spin dynamics in $La_{2-x}Ba_xCuO_4$ for $x \leqslant 0.035$. We observe the low-energy dynamic susceptibility to evolve with temperature on a much higher temperature scale than that given by the effective 2D IC T_N for any doping, and show that 2D IC dynamic spin correlations inhabit much of the phase diagram associated with the "pseudogap" state.[34]

We will focus our discussion on the 214 cuprate HTS families. For the low-doping levels we are considering, $La_{2-x}Ba_xCuO_4$ and $La_{2-x}Sr_xCuO_4$ are isostructural.[35,36] At temperatures that are high relative to room temperature, these crystals display tetragonal crystal structures with space group $I4/mmm$. As the temperature is lowered, they undergo a structural phase transition to an orthorhombic structure with space group *Bmab*. This transition occurs near ∼308 K for $x \sim 0.08$ in LBCO,[9] and increases in temperature with decreasing doping. We will be presenting measurements on LBCO for $x \leqslant 0.035$ and $T \leqslant 300$ K. As such, our samples are orthorhombic at all temperatures measured. The lattice parameters in the orthorhombic basal plane are similar, and this has led some to treat the orthorhombic cell as tetragonal for convenience.[10] We too shall adopt this simplification. Doing so, we label the C AF wave vector as $(\frac{1}{2},\frac{1}{2},L)$ and the diagonal IC ordering wave vectors, relevant for LBCO with $x < 0.05$, as having the form $(\frac{1}{2} \pm \delta,\frac{1}{2} \pm \delta,L)$ and $(\frac{1}{2} \mp \delta,\frac{1}{2} \pm \delta,L)$.

II. EXPERIMENTAL DETAILS

High-quality single crystals of $La_{2-x}Ba_xCuO_4$ with $x = 0$, 0.006, 0.0125, 0.025, and 0.035 were grown by floating zone image furnace techniques using a four-mirror optical furnace. The growth method has been reported on previously.[37,38] The resulting samples were cylindrical in shape and weighed ∼7 grams each. The crystals were all grown in the same excess oxygen atmosphere, resulting in a small oxygen off-stoichiometry. This oxygen off-stoichiometry could be estimated by measuring the 3D C AF phase transition in undoped $La_2CuO_{4+\delta}$, as T_N is known to be sensitive to the precise value of δ.[39] From a determination that $T_N \sim 250$ K for our $La_2CuO_{4+\delta}$ single crystal, we estimate that $\delta \approx 0.004$. We expect this to be the same for all of our $La_{2-x}Ba_xCuO_{4+\delta}$ samples, as they were grown under similar conditions. Hereafter, we will not refer to the oxygen off-stoichiometry in the crystals.

Neutron-scattering measurements were performed using both time-of-flight and triple-axis spectrometers. These measurements were carried out using several different cryostats, allowing access to the approximate temperature range of 1.5 to 300 K. Three sets of triple-axis neutron measurements were performed at two laboratories. All measurements were performed with the horizontal scattering plane coincident with the *HK*0 plane of the crystal. Two of these triple-axis measurements employed a constant final energy of $E_f = 14.7$ meV. The first was a set of measurements at the N5 beam line of the NRU reactor at Chalk River Laboratories, which employed a collimation of open-36′-48′-72′ using the convention of collimation between source-monochromator, monochromator and sample, sample and analyzer, and analyzer and detector. The second was a set of measurements using the HB3 instrument at Oak Ridge National Laboratory, which employed 48′-40′-40′-120′. Both sets of measurements employed a pyrolitic graphite filter in the scattered beam to suppress harmonic contamination, and both had an approximate energy resolution of ∼1 meV. High-resolution, elastic-scattering measurements were also made at Chalk River using $E_f = 5.1$ meV and collimation of open, 12′, 12′, 72′. These measurements performed at Chalk River employed a cooled beryllium filter for suppression of higher harmonic incident neutrons. Time-of-flight neutron-scattering measurements were performed using the NG4 Disk Chopper Spectrometer (DCS)[40] at the National Institute of Standards and Technology (NIST) Center for Neutron Research. All DCS measurements presented here were performed using an incident neutron wavelength of 5 Å and a corresponding energy resolution of ∼0.09 meV. The measurements at DCS were performed with the *HHL* plane of the crystals coincident with the horizontal plane.

III. RESULTS AND DISCUSSION

A. Magnetic order-parameter measurements

Magnetic order-parameter measurements of 3D Bragg peaks using triple-axis spectrometers are relatively straightforward to perform, compared with the corresponding measurement of 2D Bragg signatures. This is because 3D ordered systems display Bragg spots in reciprocal space, while 2D Bragg signatures appear as rods in reciprocal space. If the strength of the elastic magnetic scattering is otherwise the same, then the neutron intensity at a single **Q** position is much larger in the 3D case, as the signal from the 3D ordered state is localized at a resolution-broadened point in reciprocal space, rather than along a rod in the 2D case. Such measurements for a sample of the nominally undoped LBCO $x = 0$ yield a sharp onset to 3D C Bragg scattering at $(\frac{1}{2},\frac{1}{2},0)$ for $T_N = 250$ K. Similar measurements were carried out on $x = 0.006$ and $x = 0.0125$ samples.

Figure 1 shows the results of such order-parameter measurements for $x = 0.0125$, 0.025, and 0.035 LBCO samples. Figure 1 also shows high-resolution elastic triple-axis measurements performed with tight collimations and 5.1 meV neutrons for the 3D C Bragg peak near $\mathbf{Q} = (\frac{1}{2},\frac{1}{2},0)$ in the

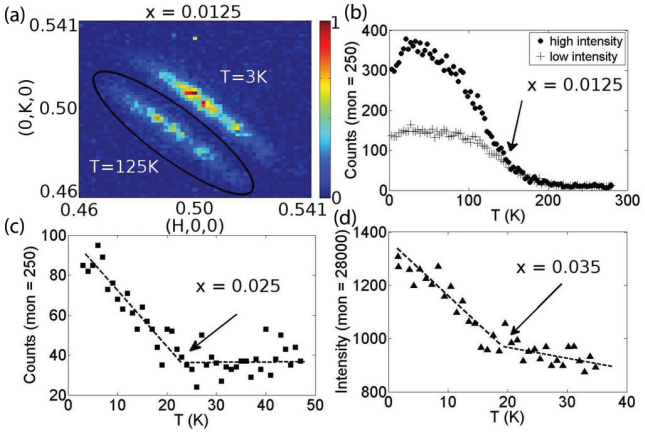

FIG. 1. (Color online) Elastic triple-axis neutron-scattering measurements of $La_{2-x}Ba_xCuO_4$ for $x = 0.0125$, 0.025, and 0.035 taken on N5 and HB3. (a) Reciprocal space maps in the (HK0) plane for $x = 0.0125$ taken at 3 and 125 K. The two temperature data sets have been shifted for ease of viewing. (b) Order-parameter measurement for $x = 0.0125$. The solid circle data are measured at the high-intensity "hot spot" identified in the (HK0) map in (a). The crosshatched data are collected within the ellipse of elastic scattering in (a), but away from the hot spot. (c), (d) Low-resolution, elastic-scattering measurements of the 2D IC order parameters for $x = 0.025$ and 0.035, respectively. Dashed lines serve as guides to the eye.

$x = 0.0125$ sample. Mesh scans in reciprocal space taken at $T = 3$ and 125 K are shown in Fig. 1(a), with the two data sets artificially displaced from each other in the figure for clarity. In addition, the intensity scale of each data set has been normalized such that the peak intensity is unity. A broad, elliptical distribution of elastic scattering is observed at all temperatures below ∼200 K. However, as can be seen by comparing the $T = 3$ K map with the intensity-normalized map at $T = 125$ K in Fig. 1(a), a high-intensity "hot spot" develops within the ellipse of elastic scattering for temperatures less than ∼150 K. We note that the elongated nature of these peaks along the transverse direction is due to a combination of the crystal's twinned orthorhombic structure, its mosaic, which is on the order of 1 degree, and the resolution of the spectrometer.

It is possible to follow the temperature dependence of the hot-spot scattering and that in the weaker periphery of the ellipse. Many such measurements were made. The temperature dependence of the sum of all of the Bragg scattering at high-intensity hot spots and at low-intensity positions within this ellipse are shown in Fig. 1(b). One can see that these two sets of temperature dependencies are the same above ∼150 K, where both the hot spots and the periphery of the Bragg positions show upwards curvature as a function of decreasing temperature. Below ∼150 K, the two temperature dependencies markedly depart from each other, with the intensity at the hot-spot positions (solid circle data points) becoming much stronger than that at the corresponding low-intensity positions (crosshatched data points). We, therefore, identify $T_N = 150$ K for 3D C order in our $x = 0.0125$ single-crystal sample of LBCO.

For the same $x = 0.0125$ data set at ∼25 K, we observe a pronounced drop off in the intensity of the 3D C AF Bragg scattering. This can be seen in the hot-spot order parameter of Fig. 1(b), which corresponds to the high-intensity positions of the reciprocal space map shown in Fig. 1(a). As we will see, this decrease in intensity is associated with the development of coexisting 2D IC elastic scattering, which occurs with an "effective" T_N of ∼25 K for $x = 0.0125$. The origin for the decomposition of the 3D C ordered state into coexisting 2D IC static order and 3D C static order is not completely clear, but has been the subject of some theoretical discussion.[41,42]

Similar high-resolution elastic magnetic Bragg scattering measurements were performed on $La_{2-x}Ba_xCuO_4$ with $x = 0.025$ and 0.035, with no obvious sign of 3D C AF order in either sample. Lower-resolution elastic-scattering measurements were performed using 14.7 meV neutrons and relatively coarse collimation, looking explicitly for 2D IC order at appropriate 2D IC diagonal wave vectors $\mathbf{Q} = (\frac{1}{2} \pm \delta, \frac{1}{2} \pm \delta, L)$, with $\delta \sim x$ and $L = 0$, as required for measurements within the HK0 scattering plane. The scattering at these 2D IC Bragg positions is weak even at low temperatures, as expected for constant-$\mathbf{Q}$ elastic-scattering measurements of a 2D rod of scattering. Nonetheless, effective 2D IC magnetic order parameters were measured and these are shown for $x = 0.025$ and 0.035 samples in Figs. 1(c) and 1(d), respectively. From these measurements, we identify effective 2D T_N of ∼23 and 18 K for $x = 0.025$ and $x = 0.035$, respectively.

B. Time-of-flight elastic neutron-scattering measurements

The DCS time-of-flight spectrometer was used to measure reciprocal space maps of both the elastic, $-0.09 \leqslant \hbar\omega \leqslant 0.09$ meV, and inelastic, $0.09 \leqslant \hbar\omega \leqslant$ ∼0.8 meV, magnetic scattering from our lightly doped LBCO samples, as a function of temperature. Time-of-flight data are shown in Figs. 2–4. Figure 2 shows maps of the elastic scattering within the HHL scattering plane around $(\frac{1}{2}, \frac{1}{2}, L)$ for four different dopings of $La_{2-x}Ba_xCuO_4$: $x = 0$, 0.0125, 0.025, and 0.035. The top panels of Fig. 2 show these maps taken within the ground state of the samples at $T = 1.5$ K. The bottom panels show the same elastic-scattering HHL maps for the same four samples, but now taken at $T = 35$ K. This is still at a low temperature, but above 25 K, which is the effective 2D T_N for $x = 0.0125$ and is the highest for any of these samples. The ranges of L shown were chosen to avoid complications due to absorption by the sample.

Three types of Bragg diffraction features can be seen in these reciprocal space maps. Two of these features are 3D C Bragg peaks of the form ($\frac{1}{2}$, $\frac{1}{2}$, L = even and L = odd). The ($\frac{1}{2}$, $\frac{1}{2}$, L = even) 3D C Bragg peaks at $L = -2$ for $x = 0$ and $x = 0.0125$ are nuclear-allowed Bragg peaks. The ($\frac{1}{2}$, $\frac{1}{2}$, L = odd) 3D C Bragg peak at $L = -3$ for $x = 0$ and $x = 0.0125$ is magnetic in origin. Such 3D C magnetic Bragg peaks are absent at all temperatures for the $x = 0.025$ and 0.035 samples, and for the $x = 0$ and $x = 0.0125$ above their 3D T_N's, at ∼250 and 150 K, respectively.

One clearly observes rods of magnetic elastic scattering of the approximate form $(\frac{1}{2}, \frac{1}{2}, L)$ for all x except $x = 0$. These are centered on diagonal IC wave vectors $(\frac{1}{2} \pm \delta, \frac{1}{2} \pm \delta, L)$.

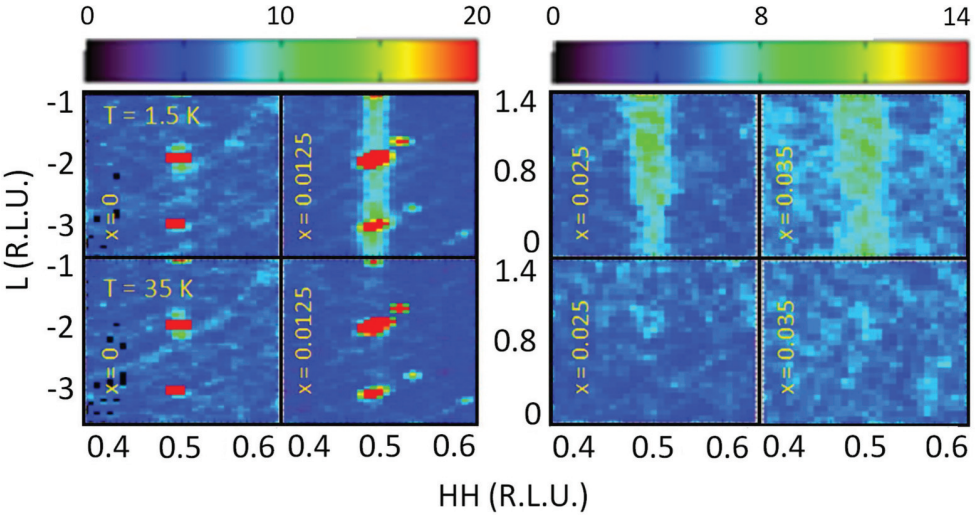

FIG. 2. (Color online) Elastic scattering in $La_{2-x}Ba_xCuO_4$. From left to right are elastic-scattering maps of $La_{2-x}Ba_xCuO_4$ for $x = 0, 0.0125$, 0.025, and 0.035, respectively. The top row shows data taken at 1.5 K and the bottom row shows data taken at 35 K. All data have an empty cryostat background subtracted from them.

Note that $\delta \sim x$ is small at these low dopings. The rods of scattering are clearly distinct from the Bragg "spots" which signify 3D order. Furthermore, these rods show little or no L dependence, a fingerprint of highly correlated 2D planes of Cu spin-$\frac{1}{2}$ magnetic moments, which are largely decoupled from each other. The only L dependence which is observed in our measurements is that associated with self-absorption of the sample in the neutron beam, due to the fact that the cylindrical axis of the crystals is not normal to the scattering plane.

Figure 2 shows that the 3D C magnetic order in the $x = 0$ and 0.0125 samples is largely unaffected by raising the temperature from 1.5 to 35 K. In the $x = 0.0125$ sample, 2D IC static correlations coexist with 3D C AF order at $T = 1.5$ K, but no signal of the 2D IC static magnetic scattering remains by $T = 35$ K, leaving only the 3D C AF order. In both the $x = 0.025$ and 0.035 samples, only 2D IC static magnetic order exists within the ground state, while the 3D C AF order is absent. This is consistent with the low-resolution triple-axis measurements on the $x = 0.025$ and 0.035 samples shown in Figs. 1(c) and 1(d), wherein the 2D IC magnetism disappears at relatively low temperatures, but above their effective 2D T_N of ∼23 and 18 K, respectively. The appearance of the 2D rods of scattering below ∼25 K in the $x = 0.0125$ sample correlates nicely with the suppression of its 3D C magnetic Bragg scattering shown in Fig. 1(a).

The temperature dependence of the magnetic elastic scattering in the $x = 0.0125$ samples merits further attention, as both 3D C AF Bragg peaks and 2D IC rods of magnetic scattering coexist within the ground state. We have already seen that the temperature dependence of the 3D C AF Bragg peak for $x = 0.0125$, shown in Fig. 1(b), has a reduction in the scattered intensity below ∼25 K. The top set of panels

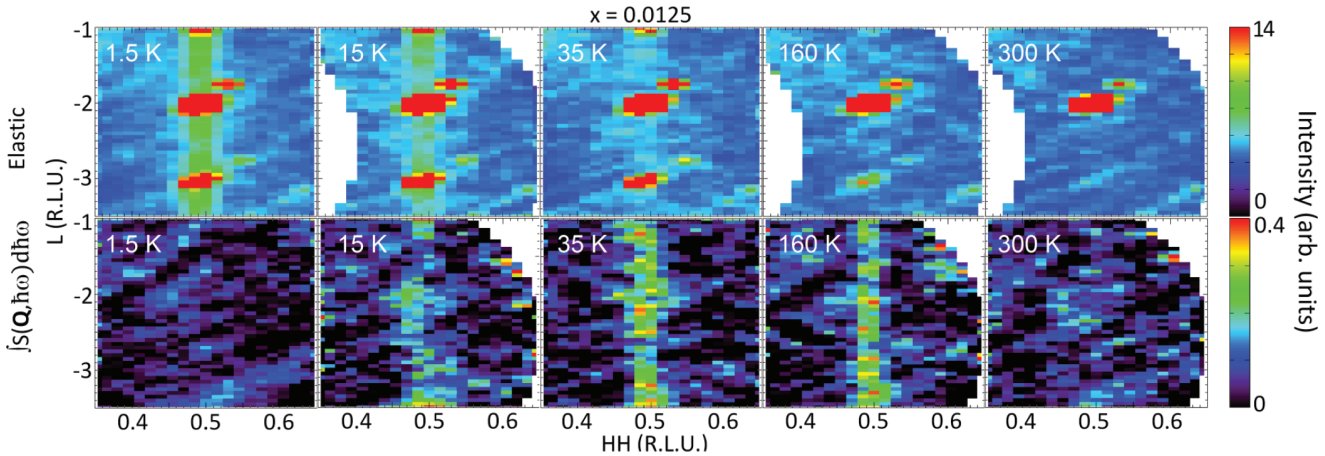

FIG. 3. (Color online) Top row: elastic scattering in $La_{2-x}Ba_xCuO_4$ for $x = 0.0125$ shown as a function of temperature. Bottom row: Low-energy inelastic scattering for the same $x = 0.0125$ crystal, $S(\mathbf{Q},\hbar\omega)$, integrated between 0.15 and 0.8 meV. Both sets of data were collected in the same time-of-flight measurement on DCS and used the same empty cryostat background subtractions. White areas correspond to regions that were not measured.

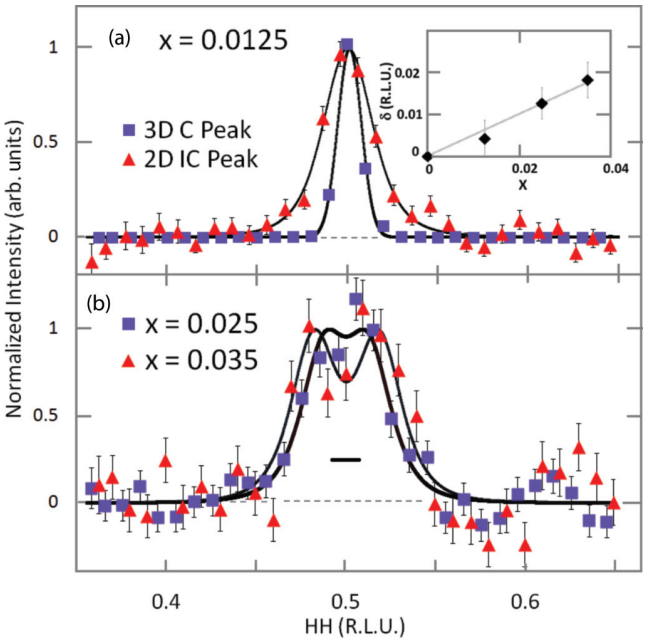

FIG. 4. (Color online) Cuts through the elastic magnetic scattering are shown for $x = 0.0125$, 0.025, and 0.035. Data sets have been normalized to their own maximum intensity for the purposes of qualitative comparison. Solid lines are fits to the data as discussed in the text. (a) 3D C structural and 2D IC magnetic peaks are shown in $x = 0.0125$ at $T = 1.5$ K. The 2D IC for this doping integrated the data over the $[-3.6,-3.2]$, $[-2.7,-2.2]$,$[-1.6,-1.2]$,$[-0.9,-0.65]$ ranges in L, so as to avoid contributions from 3D C peaks. The 3D C structural peak corresponds to $L = -4$ and employs a $-4.1 \leqslant L \leqslant -3.9$ integration. (b) 2D IC peaks in $x = 0.025$ and 0.035 using $0 \leqslant L \leqslant 1.9$ integration for both samples. This range avoids contributions from nuclear Bragg peaks and is minimally affected by self-absorption. Inset: Incommensuration δ as a function of doping as determined from fits of the data. Error bars represent one standard deviation.

in Fig. 3 shows the same $(\frac{1}{2},\frac{1}{2},L)$ elastic reciprocal space map for $x = 0.0125$ shown in Fig. 2, now as a function of temperature. For now, we will focus only on the top panels and will return to the bottom panels when we discuss the inelastic scattering in a later section. We clearly see the disappearance of the rod of elastic scattering as the temperature increases to $T = 35$ K, and that the 3D C AF peak near $(\frac{1}{2},\frac{1}{2},-3)$ has all but disappeared at $T = 160$ K, above the 3D C $T_N \sim$ 150 K, identified in Fig. 1(b) from high-resolution triple-axis order-parameter measurements. We note that the nuclear Bragg peak at $(\frac{1}{2},\frac{1}{2},-2)$ is nearly temperature independent over the range of temperatures shown. This is as expected for a nuclear Bragg peak, given that all temperatures studied are well removed from the orthorhombic-tetragonal structural phase transition in this material.[43]

The tradeoff between 3D C AF and 2D IC static magnetism shown in Figs. 3 and 1(b) is similar to that reported for $La_{2-x}Sr_xCuO_4$ at similar doping levels.[2] It implies that the 3D C AF structure forms as the temperature is lowered, but that part of this structure is unstable to the formation of 2D IC order below the 2D effective T_N of 25 K in the $x = 0.0125$ sample. While it is not easy to compare the integrated intensity of the 2D rod scattering to the 3D C AF Bragg scattering, it is straightforward to estimate the reduction of the 3D C AF Bragg peak from saturation shown below ~25 K in Fig. 1(b). This shows that for $x = 0.0125$, the 2D IC static order accounts for 20% of the elastic magnetic scattering in the ground state. As suggested for $La_{2-x}Sr_xCuO_4$, this fraction presumably grows with x until it accounts for 100% of the static elastic magnetic scattering in the ground state for $x \geqslant 0.02$.[18] As previously noted, several theoretical suggestions have been put forward as to the origin of the decomposition of the 3D C to the coexistence of 3D C static order with 2D IC static order, as shown in Figs. 1(b) and 3.[41,42]

The *HHL* reciprocal space maps around $(\frac{1}{2},\frac{1}{2},L)$, shown in Fig. 2, all cover the same range in (*HH*). Note that the L ranges shown differ due to the fact that the self-absorption for a given position in the (*HHL*) plane differs for the four crystals. It is clear that at $T = 1.5$ K (the top panels in Fig. 2), the rod of magnetic scattering broadens in the (*HH*) direction progressively with increasing doping from $x = 0.0125$ to 0.035. This is due to the fact that 2D IC static order is expected to change its incommensuration with doping, and the expected dependence is roughly $\delta \sim x$ in the diagonal IC wave vector $(\frac{1}{2} \pm \delta, \frac{1}{2} \pm \delta, L)$.[44,45]

We can explicitly examine the line shape associated with the 2D IC rods of magnetic scattering and estimate both the δ vs x dependence in the ground state, and the finite range of the in-plane spin correlations within the 2D IC structure. In Fig. 4, we show cuts in the (*HH*) direction through the reciprocal space maps displayed in the top row of Fig. 2 appropriate to $T = 1.5$ K. For the $x = 0.0125$, 0.025, and 0.035 data sets, the cuts are taken so as to pick out only the 2D IC rod scattering; that is, they sample data between the nuclear-allowed $(\frac{1}{2},\frac{1}{2},L$ = even) 3D Bragg peaks for all samples, as well as avoid the 3D C magnetic Bragg peaks at $(\frac{1}{2},\frac{1}{2},L$ = odd) for the $x = 0.0125$ sample. For comparison, we also have a cut through the $L = -4$ structural Bragg peak in the $x = 0.0125$ sample as a measure of the instrumental resolution.

These cuts are shown in Figs. 4(a) and 4(b). The $x = 0.0125$ 3D C data set is clearly much narrower in (*HH*) than that of any of the other three data sets, which exhibit 2D diagonal IC order. The three 2D IC data sets were fit phenomenologically to a functional form of two squared Lorentzians with identical widths and amplitudes, but centered at different *HH* positions. Previous studies of such quasi-two-dimensional correlations also employed Lorentzian-squared line shapes to describe the IC elastic scattering.[33] Initially, these data were fit with the sum of two Lorentzians-squared line shapes, wherein their widths were allowed to vary with x. However, the resulting variation of the width with x was small, and the fits were redone using a common width for the Lorentzian-squared line shapes in all fits.

As the finite (*HH*) width to the Lorentzian-squared line shape represents a finite (inverse) correlation length, we conclude that the 2D IC static order is short ranged in $La_{2-x}Ba_xCuO_4$, with a correlation length of ~20 Å. Over this doping range and to within our resolution, this correlation length is independent of doping. The diagonal IC wave vector δ can then be extracted from this analysis, and this is shown as a function of x at $T = 1.5$ K in the inset to Fig. 4(a). We observe a linear relationship $\delta \sim x$ for $x = 0.125$, 0.025, and

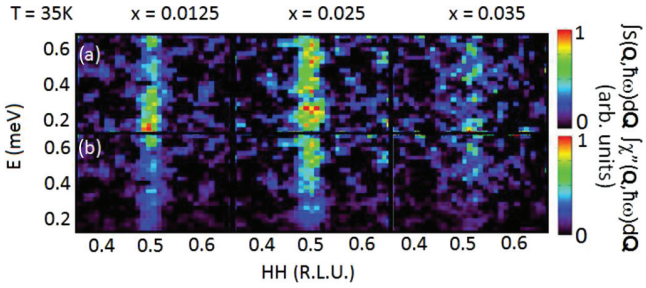

FIG. 5. (Color online) Inelastic scattering for $x = 0.0125$, 0.025 and 0.035 at $T = 35$ K. All data sets employed a $T = 1.5$ K data set as background. (a) and (b) show energy-*HH* wave-vector maps for (a) $S(\mathbf{Q}, \hbar\omega)$ and (b) $\chi''(\mathbf{Q}, \hbar\omega)$. These data sets employed $-3.5 \leqslant L \leqslant -1$ integration for $x = 0.0125$ and $0 \leqslant L \leqslant 1.9$ integrations for $x = 0.025$ and 0.035. $\chi''(\mathbf{Q}, \hbar\omega)$ is related to $S(\mathbf{Q}, \hbar\omega)$ through Eqs. (1) and (2).

0.035, which extrapolates back through zero at $x = 0$. This conclusion is somewhat different from that reached in previous studies of $La_{2-x}Sr_xCuO_4$, wherein a linear $\delta \sim x$ relationship was also found for sufficiently large x, but δ was ∼independent of x for very low concentrations, <0.02, which also displayed 3D C AF order.[44,46]

C. Time-of-flight inelastic-scattering measurements and dynamic susceptibility

The DCS time-of-flight instrument allows the simultaneous measurement of elastic neutron scattering and inelastic neutron scattering. Reciprocal space maps of the inelastic scattering can also be constructed, similar to the elastic-scattering data presented in Figs. 2 and 3. The relatively low incident energy E_i employed in these measurements restricts the accessible inelastic scattering to less than ∼1 meV energy transfer, although the magnetic excitations in this system are known to exist to significantly higher energy.[31] We have plotted inelastic scattering for the $x = 0.0125$ sample as a function of temperature in the bottom panels of Fig. 3. A comparison between this magnetic inelastic scattering from the 0.0125, 0,025, and 0.035 samples, all at $T = 35$ K, is shown in the top panel of Fig. 5.

The bottom panels of Fig. 3 show reciprocal space maps of the inelastic scattering from the $x = 0.0125$ sample, integrated in energy from 0.1 to 1 meV, and as a function of temperature between $T = 1.5$ and 300 K. This integrated inelastic magnetic scattering can be compared directly to the same reciprocal space maps of the elastic scattering around $(\frac{1}{2}, \frac{1}{2}, L)$ wave vectors, as shown in the top panels of Fig. 3. On this relatively low-energy scale, we observe an interesting trend wherein little inelastic scattering is observed at $T = 1.5$ K, although both the 2D IC elastic rod of magnetic scattering and the 3D C AF Bragg peaks are strong. As the elastic rod of 2D IC scattering for the $x = 0.0125$ sample fades in intensity above $T = 15$ K, the inelastic scattering becomes clearly evident. Above the 2D effective $T_N \sim 23$ K, only the 2D IC inelastic scattering and the 3D C elastic magnetic scattering remain. The intensity of the 2D IC inelastic scattering is prevalent out to 160 K, but has clearly faded at the highest temperature measured, $T = 300$ K. The lower panels of Fig. 3 show that 2D IC dynamic spin fluctuations in the $x = 0.0125$ sample are present well above the effective 2D $T_N \sim 23$ K, and only completely disappear above the temperature characteristic of the 3D C $T_N \sim 150$ K, in this sample.

The evolution of the low-energy inelastic magnetic scattering and the corresponding imaginary part of the dynamic susceptibility as a function of doping is shown in Fig. 5. The top panel of Fig. 5(a) shows the inelastic scattering at $T = 35$ K for each of the $x = 0.0125$, 0.025, and 0.035 samples. There data has been integrated in L using $-3.5 < L < -1$ for $x = 0.0125$ and $0 < L < 1.9$ in $x = 0.025$ and 0.035. The reason for this choice of L integration is that these regimes avoid complications due to self-absorption that arise as the sample is rotated in the beam. This data is plotted in an energy vs (*HH*) wave-vector map, over the approximate range in energy from 0.15 to 0.8 meV. A temperature of 35 K was chosen for this comparison as it is sufficiently low to approximate the ground state, while high enough such that appreciable magnetic inelastic intensity is evident in all samples. We note that there is little magnetic inelastic scattering evident at $T = 1.5$ K. We take advantage of this and use the $T = 1.5$ K data sets as a measure of the inelastic background for our samples. This will be important in isolating the dynamic magnetic susceptibility from our inelastic scattering data.

The magnetic inelastic scattering, expressed as $S(\mathbf{Q}, \hbar\omega, T)$, is the product of two terms: the Bose population factor, which maintains detailed balance, and the imaginary part of the dynamic susceptibility χ''. χ'' is an odd function of energy and characterizes the capacity of the system to absorb energy, thereby creating spin excitations at a particular wave vector and energy. The inelastic magnetic scattering, $S(\mathbf{Q}, \hbar\omega, T)$, is then related to the imaginary part of the dynamic susceptibility through

$$S(\mathbf{Q},\hbar\omega,T) = [n(\hbar\omega,T) + 1] \times \chi''(\mathbf{Q},\hbar\omega,T), \qquad (1)$$

where $[n(\hbar\omega,T) + 1]$ is the Bose population factor,

$$[n(\hbar\omega,T) + 1] = \frac{1}{1 - e^{\frac{-\hbar\omega}{k_B T}}}. \qquad (2)$$

At $T = 35$ K and for energies ⩽1 meV, the Bose population factor, $[n(\hbar\omega,T) + 1]$, is sufficiently strong that the overall neutron-scattering signal, $S(\mathbf{Q}, \hbar\omega)$, can be easily distinguished from the background for all concentrations. One can isolate $S(\mathbf{Q},\hbar\omega)$ with an appropriate subtraction and divide through by the Bose factor to give the imaginary part of the dynamic susceptibility, χ''. This is what is shown in the panels of Fig. 5(b) for $x = 0.0125$, 0.025, and 0.035, listed from left to right. The panels of Fig. 5(a) show the corresponding $S(\mathbf{Q}, \hbar\omega)$. Focusing on $\chi''(\mathbf{Q},\hbar\omega)$ in the panels of Fig. 5(b), we see a suppression of $\chi''(\mathbf{Q},\hbar\omega)$ at low energies. This suppression increases with doping between 0.0125 and 0.035. In Fig. 6, we show cuts of $\chi''(\mathbf{Q},\hbar\omega)$ made by integrating the data in Fig. 5(b) in (*HH*) around $0.48 \leqslant (H\,H) \leqslant 0.52$ and over the relevant L range so as to capture all of the dynamic magnetic susceptibility in this low-energy regime. The resulting quantity is then plotted in Fig. 6 as a function of energy for $x = 0.0125$, 0.025, and 0.035. We see a suppression of the low-energy dynamic susceptibility as the doping increases. This can be quantified by fitting the energy dependence of this integrated low-energy dynamic susceptibility to the phenomenological

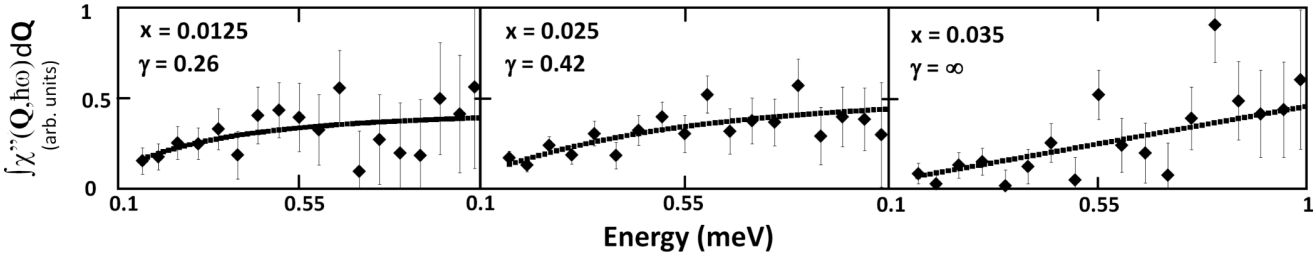

FIG. 6. The energy dependence of $\chi''(\mathbf{Q},\hbar\omega)$ integrated over the HH width of the rod of scattering shown in Fig. 5(b), as described in the text. The dashed line shows a fit to a phenomenological model, given by Eq. (3), describing this energy dependence.

form[47]

$$\chi''(E) = A\tan^{-1}(E/\gamma). \tag{3}$$

This allows the extraction of a characteristic energy scale γ at which the magnetic dynamic susceptibility, as a function of decreasing energy, turns over and decreases towards zero, as it must in order to be an odd function of energy. The fit is displayed as the dashed lines in Fig. 6, and the appropriate γ value resulting from the fit is displayed in the left corner of each panel.

As expected from Fig. 5(b), γ is lowest for the $x = 0.0125$ sample and increases with increased hole doping, x. It is interesting to note that this progression is established in samples that are not superconducting. One might expect this phenomena to be linked to the superconducting gap that is observed in LSCO. There, it is known that for samples of LSCO with superconducting ground states, that is, $x \geqslant 0.05$, a spin gap forms for $T < T_C$ within the dynamic susceptibility at low energies. For example, for samples with $x = 0.16$, it is reported that the gap is 7 meV.[48] That said, it has also been reported that no such corresponding spin gap exists in LBCO out to at least $x = 1/8$.[37] This has been motivated by the absence of a temperature dependence to the low-energy dynamic susceptibility in underdoped superconducting samples. However, there has been the suggestion that a superconducting gap may exist for higher dopings.[10] To be sure, the present spin-gap-related phenomena may be different from the related phenomena which occurs in LSCO. But, it is clear that an interesting depletion in dynamic susceptibility as a function of increasing doping seems to be a characteristic of LBCO as well.

We now examine the temperature dependence of $\chi''(\mathbf{Q},\hbar\omega)$ for $x = 0.0125$ and 0.035 samples in Figs. 7–9. Figure 7 shows $\chi''(\mathbf{Q},\hbar\omega)$ for $x = 0.0125$ in energy vs (HH) maps over the range of energy from 0.15 to 0.8 meV, again integrated in L around the ranges appropriate to isolate 2D rods of scattering, as used in Fig. 5. These data sets are at temperatures ranging from 10 to 300 K, as denoted in the bottom left of each panel, and all data sets used $T = 1.5$ K data sets as background. Figure 8 shows the same $\chi''(\mathbf{Q},\hbar\omega)$ maps for the $x = 0.035$ sample over the temperature range $T = 10$ to 35 K, again using the appropriate $T = 1.5$ K data set as a background.

In both the $x = 0.0125$ and 0.035 cases, $\chi''(\mathbf{Q},\hbar\omega)$ clearly decreases monotonically with increasing temperature over this relatively low-energy range. The intriguing behavior seen in the bottom panels of Fig. 3 for the $x = 0.0125$ sample, wherein the 2D IC inelastic intensity appears to have a temperature dependence complementary to that of the 2D IC elastic scattering, can be understood as a consequence of the temperature dependence of the Bose factor, $[n(\omega) + 1]$.

To better understand $\chi''(\mathbf{Q},\hbar\omega,T)$ quantitatively, we integrated the $\chi''(\mathbf{Q},\hbar\omega)$ data shown in Figs. 7 and 8 in energy between 0.2 and 0.8 meV. This was then fit to a Gaussian line shape centered on $HH = (\frac{1}{2},\frac{1}{2})$ with a linear background. The integrated intensity of the Gaussian gives $\chi''(\mathbf{Q} \sim (\frac{1}{2},\frac{1}{2},L))$, $0.2 \leqslant \hbar\omega \leqslant 0.8$ meV, which is plotted as a function of temperature on a semilogarithmic scale in Fig. 9 for both $x = 0.0125$ and 0.035 samples. The signals from the $x = 0.0125$ and 0.035 samples have been approximately normalized at low temperatures. The values of $T_{N(\text{2D IC})}$ for $x = 0.0125$ (25 K) and 0.035 (15 K) as well as $T_{N(\text{3D C})}$ for $x = 0.0125$ (150 K) and $x = 0$ (250 K) are indicated for reference as dashed lines in Fig. 9. We find that the dynamic IC magnetism in both samples is present on a temperature scale that is independent of the static ordering temperatures in either system. $\chi''(\mathbf{Q},\hbar\omega)$ is strongest at low temperatures in both materials, and its temperature dependence does not suggest a well-defined transition temperature. The phenomenon observed is instead consistent with a crossover that occurs at some temperature above the 3D C T_N for the $x = 0.0125$ system.

D. Magnetic phase diagram

We summarize our elastic and inelastic magnetic neutron-scattering measurements on relatively lightly doped

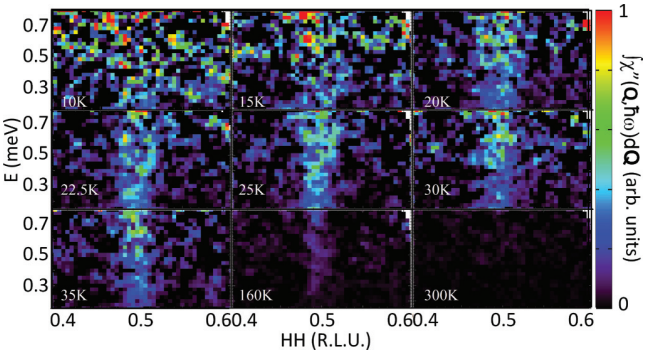

FIG. 7. (Color online) Energy-wave-vector maps of $\chi''(\mathbf{Q},\hbar\omega)$ for $x = 0.0125$ as a function of temperature, from 10 to 300 K. There is a clear monotonic decrease in the spectral weight of the dynamic magnetism with temperature.

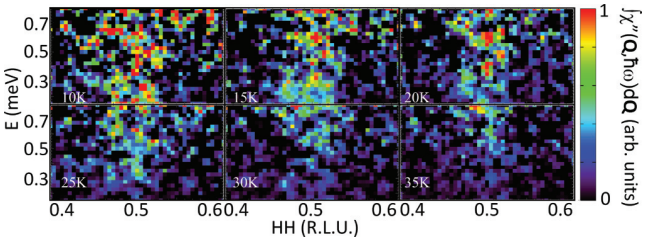

FIG. 8. (Color online) Energy-wave-vector maps of $\chi''(\mathbf{Q},\hbar\omega)$ for $x = 0.035$ are shown as a function of temperature, from 10 to 35 K.

$La_{2-x}Ba_xCuO_4$ in the phase diagram shown in Fig. 10. It displays three sets of points, which represent phase-transition temperatures appropriate to 3D C AF order (red circles), 2D diagonal IC static order (yellow triangles), and 2D parallel IC order (blue circles). The latter set of phase transitions occur for concentrations with superconducting ground states for $x \geqslant 0.05$, and comes from our earlier neutron results on magnetic order-parameter measurements.[6,49]

We also show extended regions on the phase diagram where 2D dynamic IC magnetism is observed. As seen in Fig. 9, this dynamic 2D IC magnetism gradually fades with increasing temperature and does not display an obvious phase transition. This dynamic 2D IC magnetism occupies the same general region of the HTS phase diagram associated with the "pseudogap phase." The pseudogap phase has been ascribed to several different origins, including phase-incoherent superconducting pairs[50] and ordering associated with orbital currents.[51] Whatever other properties it possesses, it is clear that 2D IC spin fluctuations are strong throughout this entire region and

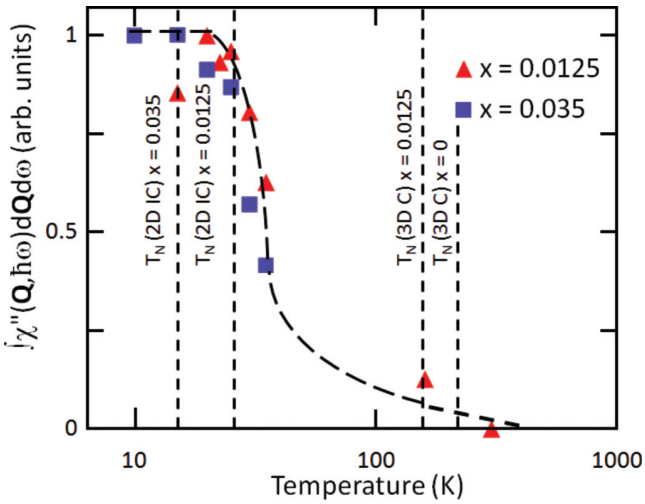

FIG. 9. (Color online) Temperature dependence of the wave-vector and low-energy ($0.2 \leqslant \hbar\omega \leqslant 0.8$ meV) integrated $\chi''(\mathbf{Q},\hbar\omega)$ for $x = 0.0125$ and 0.035 as a function of temperature on a semilogarithmic scale. Dashed lines show the 2D IC (for $x = 0.035, 0.0125$) and 3D C (for $x = 0.0125$ and 0) magnetic ordering temperatures. The $x = 0.0125$ and 0.035 data sets have been normalized at low temperatures. Both data sets have employed their 1.5 K data set as a background. The temperature scale for the evolution of this low-energy dynamic magnetism greatly exceeds the relevant 2D IC magnetic ordering temperatures.

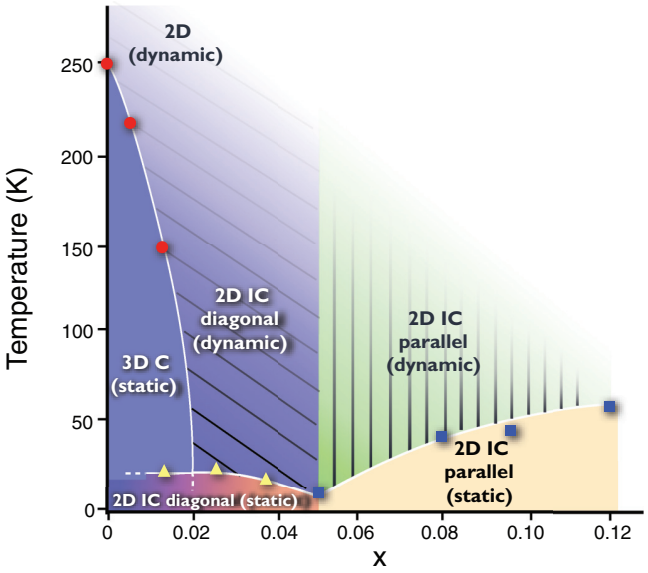

FIG. 10. (Color online) Magnetic phase diagram for $La_{2-x}Ba_xCuO_4$ as determined by magnetic order-parameter measurements on $La_{2-x}Ba_xCuO_4$ crystals with $x \leqslant 0.125$.[6,10] 3D static C magnetic order gives way to 2D static (on the time scale of high-energy resolution neutron measurements) diagonal IC order for $x \geqslant 0.02$, with a coexistence between the two at low temperatures for smaller values of x. At an $x \sim 0.05$ quantum critical point, the 2D IC ordering wave vector rotates from diagonal to parallel, relative to the pseudo-tetragonal axes, and this is coincident with the onset of a superconducting ground state.[6] Dynamic 2D IC fluctuations persist to temperatures much higher than those characterizing the onset of static 2D order. These fade continuously with increasing temperature and inhabit much of the phase diagram associated with the "pseudogap" phase.

that the crossover to a fully paramagnetic state occurs on a high-temperature scale.

Coming back to the 3D C and 2D IC phase transitions identified from elastic neutron-scattering order-parameter measurements, shown as the circles, triangles, and squares, respectively, in Fig. 10, there are several interesting observations to make. First and foremost, Fig. 10 is compiled exclusively from magnetic order-parameter measurements. Nevertheless, it displays much of the full complexity of the HTS phase diagram. In our opinion, such an observation in and of itself leads to the conclusion that the superconducting ground state is intimately related to the magnetic ground state. Second, the fact that the 2D effective T_N is so much smaller than the 3D C T_N is due to the decrease in dimensionality. This is clear from Fig. 2, which shows the 2D rods of magnetic scattering coexisting with 3D C magnetic Bragg peaks for the $x = 0.0125$ sample, only at low temperature. In the HTS literature, the region of the phase diagram between 3D C AF order and a superconducting ground state, which is typically $0.02 \leqslant x \leqslant 0.05$, is often referred to as a spin-glass regime.[2] This is correct in that the ground-state spin correlations within the orthorhombic basal plane of these samples are finite and elastic. However, most importantly, the spin correlation lengths between orthorhombic planes have gone to $\approx$ zero, resulting in distinct rods of magnetic scattering; that is, the layers are

decoupled. This reduction in magnetic dimensionality from 3D to 2D, on its own, would be expected to strongly suppress any ordering transition in such a layered system, and, indeed, this is what is observed. It is an interesting observation that the C spin structure within the orthorhombic plane leads to a 3D structure, while the IC spin structure within the orthorhombic plane displays a 2D ground state.

Finally, although it was first observed some time ago in $La_{2-x}Sr_xCuO_4$,[44,46] and more recently in $La_{2-x}Ba_xCuO_4$,[6] it bears repeating that the quantum critical point between nonsuperconducting and superconducting ground states in $La_{2-x}Ba_xCuO_4$, near $x \sim 0.05$, is coincident with the rotation in the 2D IC spin structure from diagonal to parallel. This also provides strong evidence for an intimate connection between the 2D magnetism and the superconducting properties in these HTS systems.

IV. CONCLUSIONS

We have carried out extensive neutron-scattering measurements on the static and low-energy, dynamic commensurate (C) and incommensurate (IC) magnetism in lightly doped $La_{2-x}Ba_xCuO_4$ (LBCO). We have shown the two-dimensional (2D) IC static order to be characterized by the appearance of rods of elastic, diagonal IC scattering with long but finite correlation lengths within the basal plane, and essentially zero correlation length along L. Moreover, below the 2D IC effective ordering temperature, $T_{N(2D\ IC)}$, these rods are elastic on the energy scale of 0.1 meV, which is $\sim$1 K or less. We can understand the suppression of the 2D IC effective ordering temperature relative to the 3D C ordering temperatures displayed by nearby concentrations as a consequence of the reduction in magnetic dimensionality, rather than being due to proximity to a competing superconducting ground state.

A phase diagram based solely on magnetic order-parameter measurements, and constructed using 3D C long-range order as well as effective 2D IC static magnetic order transitions for all LBCO samples with $x \leqslant 0.125$, is shown to display much of the same complexity as that corresponding to standard phase diagrams relevant to high-temperature superconductivity. This stresses the strong correlation between magnetism and the exotic charge correlation physics, including superconductivity itself, in this family of high-temperature superconductors. Our measurements at low temperatures show a systematic suppression of the low-energy dynamic susceptibility as a function of increasing doping within the lightly doped regime $x \leqslant 0.035$, presaging the appearance of superconducting ground states for $x \geqslant 0.05$.

All samples studied in this paper, other than $x = 0$, display 2D diagonal IC static magnetism at low temperatures within their ground states. Interestingly, we find that the corresponding dynamic IC magnetism exists at low temperatures as well as on a much higher temperature scale, comparable to nearby 3D C ordering temperatures. The temperature dependence of this dynamic IC magnetism does not change quickly with doping at these low dopings. This 2D dynamic IC magnetism inhabits much of the phase diagram associated with pseudogap physics, and there appears to be no characteristic transition temperature associated with these fluctuations; rather, their temperature evolution is characteristic of crossover phenomena.

ACKNOWLEDGMENTS

We would like to acknowledge useful conversations had with A. J. Berlinsky, C. Kallin, G. M. Luke, J. P. Clancy, K. Fritsch, A. Dabkowski, and T. Timusk. We would also like to acknowledge M. D. Lumsden for technical assistance with the measurements on HB3. Research using ORNL's High Flux Isotope Reactor was sponsored by the Scientific User Facilities Division, Office of Basic Energy Sciences, US Department of Energy. Work at McMaster was funded by NSERC of Canada. This work utilized facilities supported in part by the National Science Foundation under Agreement No. DMR-0944772.

[1] M. A. Kastner, R. J. Birgeneau, G. Shirane, and Y. Endoh, Rev. Mod. Phys. **70**, 897 (1998).

[2] R. J. Birgeneau, C. Stock, J. M. Tranquada, and K. Yamada, J. Phys. Soc. Jpn. **75**, 111003 (2006).

[3] Masaki Fujita, Haruhiro Hiraka, Masaaki Matsuda, Masato Matsuura, John M. Tranquada, Shuichi Wakimoto, Guangyong Xu, and Kazuyoshi Yamada, J. Phys. Soc. Jpn. **81**, 011007 (2012).

[4] B. Keimer, R. J. Birgeneau, A. Cassanho, Y. Endoh, R. W. Erwin, M. A. Kastner, and G. Shirane, Phys. Rev. Lett. **67**, 1930 (1991).

[5] J. G. Bednorz and K. A. Muller, Z. Phys. B **64** 189 (1986).

[6] S. R. Dunsiger, Y. Zhao, B. D. Gaulin, Y. Qiu, P. Bourges, Y. Sidis, J. R. D. Copley, A. Kallin, E. M. Mazurek, and H. A. Dabkowska, Phys. Rev. B **78**, 092507 (2008).

[7] M. Matsuda, K. Yamada, Y. Endoh, T. R. Thurston, G. Shirane, R. J. Birgeneau, M. A. Kastner, I. Tanaka, and H. Kojima, Phys. Rev. B **49**, 6958 (1994).

[8] P. Böni, J. D. Axe, G. Shirane, R. J. Birgeneau, D. R. Gabbe, H. P. Jenssen, M. A. Kastner, C. J. Peters, P. J. Picone, and T. R. Thurston, Phys. Rev. B **38**, 185 (1988).

[9] Y. Zhao, B. D. Gaulin, J. P. Castellan, J. P. C. Ruff, S. R. Dunsiger, G. D. Gu, and H. A. Dabkowska, Phys. Rev. B **76**, 184121 (2007).

[10] M. Hücker, M. V. Zimmermann, G. D. Gu, Z. J. Xu, J. S. Wen, Guangyong Xu, H. J. Kang, A. Zheludev, and J. M. Tranquada, Phys. Rev. B **83**, 104506 (2011).

[11] A. R. Moodenbaugh, Youwen Xu, M. Suenaga, T. J. Folkerts, and R. N. Shelton, Phys. Rev. B **38**, 4596 (1988).

[12] B. Keimer, N. Belk, R. J. Birgeneau, A. Cassanho, C. Y. Chen, M. Greven, M. A. Kastner, A. Aharony, Y. Endoh, R. W. Erwin, and G. Shirane, Phys. Rev. B **46**, 14034 (1992).

[13] M. Kofu, S.-H. Lee, M. Fujita, H.-J. Kang, H. Eisaki, and K. Yamada, Phys. Rev. Lett. **102**, 047001 (2009).

[14] N. P. Armitage, P. Fournier, and R. L. Greene, Rev. Mod. Phys. **82**, 2421 (2010).

[15]R. J. Birgeneau, N. Belk, Y. Endoh, R. W. Erwin, M. A. Kastner, B. Keimer, and G. Shirane, Physica B Condens. Matter **180**, 15 (1992).
[16]M. Matsuda, M. Fujita, K. Yamada, R. J. Birgeneau, M. A. Kastner, H. Hiraka, Y. Endoh, S. Wakimoto, and G. Shirane, Phys. Rev. B **62**, 9148 (2000).
[17]M. Matsuda, Y. S. Lee, M. Greven, M. A. Kastner, R. J. Birgeneau, K. Yamada, Y. Endoh, P. Böni, S.-H. Lee, S. Wakimoto, and G. Shirane, Phys. Rev. B **61**, 4326 (2000).
[18]M. Matsuda, M. Fujita, K. Yamada, R. J. Birgeneau, Y. Endoh, and G. Shirane, Phys. Rev. B **65**, 134515 (2002).
[19]S. M. Hayden, G. Aeppli, H. Mook, D. Rytz, M. F. Hundley, and Z. Fisk, Phys. Rev. Lett. **66**, 821 (1991).
[20]S. M. Hayden, G. Aeppli, H. A. Mook, T. G. Perring, T. E. Mason, S.-W. Cheong, and Z. Fisk, Phys. Rev. Lett. **76**, 1344 (1996).
[21]B. Khaykovich, S. Wakimoto, R. J. Birgeneau, M. A. Kastner, Y. S. Lee, P. Smeibidl, P. Vorderwisch, and K. Yamada, Phys. Rev. B **71**, 220508 (2005).
[22]T. R. Thurston, P. M. Gehring, G. Shirane, R. J. Birgeneau, M. A. Kastner, Y. Endoh, M. Matsuda, K. Yamada, H. Kojima, and I. Tanaka, Phys. Rev. B **46**, 9128 (1992).
[23]J. M. Tranquada, H. Woo, T. G. Perring, H. Goka, G. D. Gu, G. Xu, M. Fujita, and K. Yamada, Nature (London) **429**, 534 (2004).
[24]C. Stock, R. A. Cowley, W. J. L. Buyers, R. Coldea, C. L. Broholm, C. D. Frost, R. J. Birgeneau, R. Liang, D. Bonn, and W. N. HardyPhys. Rev. B **75**, 172510 (2007).
[25]B. Vignolle, S. M. Hayden, D. F. McMorrow, H. M. Ronnow, B. Lake, C. D. Frost, and T. G. Perring, Nature (London) **3**, 163 (2007).
[26]O. J. Lipscombe, S. M. Hayden, B. Vignolle, D. F. McMorrow, and T. G. Perring, Phys. Rev. Lett. **99**, 067002 (2007).
[27]O. J. Lipscombe, B. Vignolle, T. G. Perring, C. D. Frost, and S. M. Hayden, Phys. Rev. Lett. **102**, 167002 (2009).
[28]P. Dai, H. A. Mook, R. D. Hunt, and F. Dogan, Phys. Rev. B **63**, 054525 (2001).
[29]N. Bulut and D. J. Scalapino, Phys. Rev. B **53**, 5149 (1996).
[30]S. A. Kivelson, I. P. Bindloss, E. Fradkin, V. Oganesyan, J. M. Tranquada, A. Kapitulnik, and C. Howald, Rev. Mod. Phys. **75**, 1201 (2003).
[31]R. Coldea, S. M. Hayden, G. Aeppli, T. G. Perring, C. D. Frost, T. E. Mason, S.-W. Cheong, and Z. Fisk, Phys. Rev. Lett. **86**, 5377 (2001).
[32]C. Stock, W. J. L. Buyers, R. A. Cowley, P. S. Clegg, R. Coldea, C. D. Frost, R. Liang, D. Peets, D. Bonn, W. N. Hardy, and R. J. Birgeneau, Phys. Rev. B **71**, 024522 (2005).
[33]M. Matsuda, M. Fujita, S. Wakimoto, J. A. Fernandez-Baca, J. M. Tranquada, and K. Yamada, Phys. Rev. Lett. **101**, 197001 (2008).
[34]T. Timusk and B. Statt, Rep. Prog. Phys. **62**, 61 (1999).
[35]S. Katano, J. A. Fernandez-Baca, S. Funahashi, N. Mori, Y. Ueda, and K. Koga, Physica C **214**, 64 (1993).
[36]M. Braden, W. Schnelle, W. Scwarz, N. Pyka, G. Heger, Z. Fisk, K. Gamayunov, I. Tanka, and H. Kojima, Z. Phys. B. **94**, 29 (1994).
[37]M. Fujita, H. Goka, K. Yamada, J. M. Tranquada, and L. P. Regnault, Phys. Rev. B **70**, 104517 (2004).
[38]H. A. Dabkowska and A. B. Dabkowski, *Crystal Growth of Oxides by Optical Floating Zone Technique. Experimental Approach to Defects Determination*, Springer Handbook of Crystal Growth, Defects and Characterization (Springer-Verlag, Berlin, 2010), pp. 367–392.
[39]B. Keimer, A. Aharony, A. Auerbach, R. J. Birgeneau, A. Cassanho, Y. Endoh, R. W. Erwin, M. A. Kastner, and G. Shirane, Phys. Rev. B **45**, 7430 (1992).
[40]J. R. D. Copley and J. C. Cook, Chem. Phys. **292**, 477 (2003).
[41]K. Machida, Physica C: Superconduct. **158**, 192 (1989).
[42]Kazushige Machida and Masanori Ichioka, J. Phys. Soc. Jpn. **68**, 2168 (1999).
[43]M. Reehuis, C. Ulrich, K. Prokeš, A. Gozar, G. Blumberg, S. Komiya, Y. Ando, P. Pattison, and B. Keimer, Phys. Rev. B **73**, 144513 (2006).
[44]K. Yamada, C. H. Lee, K. Kurahashi, J. Wada, S. Wakimoto, S. Ueki, H. Kimura, Y. Endoh, S. Hosoya, G. Shirane, R. J. Birgeneau, M. Greven, M. A. Kastner, and Y. J. Kim, Phys. Rev. B **57**, 6165 (1998).
[45]M. Enoki, M. Fujita, T. Nishizaki, S. Iikubo, D. K. Singh, S. Chang, J. M. Tranquada, and K. Yamada, Phys. Rev. Lett. **110**, 017004 (2013).
[46]S. Wakimoto, R. J. Birgeneau, M. A. Kastner, Y. S. Lee, R. Erwin, P. M. Gehring, S. H. Lee, M. Fujita, K. Yamada, Y. Endoh, K. Hirota, and G. Shirane, Phys. Rev. B **61**, 3699 (2000).
[47]G. Aeppli and T. F. Rosenbaum, *Dynamical Properties on Unconventional Magnetic Systems* (Kluwer, Dordrecht, 1998).
[48]N. B. Christensen, D. F. McMorrow, H. M. Rønnow, B. Lake, S. M. Hayden, G. Aeppli, T. G. Perring, M. Mangkorntong, M. Nohara, and H. Tagaki, Phys. Rev. Lett. **93**, 147002 (2004).
[49]S. R. Dunsiger, Y. Zhao, Z. Yamani, W. J. L. Buyers, H. A. Dabkowska, and B. D. Gaulin, Phys. Rev. B **77**, 224410 (2008).
[50]V. J. Emery and S. A. Kivelson, Nature (London) **374**, 434 (1993).
[51]C. M. Varma, Phys. Rev. B **55**, 14554 (1997).

Part IV

Spin-Phonon Hybridization in Cuprate Superconductors

Chapter 4

Hybridization of Two Dimensional Spin Excitations and Phonons in $La_{1.965}Ba_{0.035}CuO_4$

This chapter and the next chapter are concerned with the topic of spin phonon hybridization. This chapter posits spin-phonon hybridization as an origin for previously observed resonant phenomena in superconducting LSCO and LBCO using a non-superconducting sample of LBCO, while the next chapter informs upon the doping dependence of these features for $0 \leq x \leq 0.11$.

This chapter provides the most detailed analysis of an enhancement feature found at 20 meV in a non-superconducting sample of LBCO. The experiment serves to resolve a number of issues of the aforementioned beyond the hour-glass excitations. First, this measurement confirms that the phenomenon is not solely found in superconducting samples. Furthermore, the enhancement feature is found to occur at the crossing of the highly dispersive magnetic excitations with, by comparison, a relatively dispersionless optic phonon mode. As these two excitations are common to all 214 cuprates, it is argued that this phenomenon should be the same as those reported previously in superconducting LBCO and LSCO. As we report that the enhancement in this x = 0.035 sample occurs at 20 meV, this confirms that the energy scale of the enhancement feature is doping independent. This serves as a first exploration of the role of these enhancement features in superconductivity and resolves many of the standing problems raised in the introduction of this thesis.

The analysis presented is of a four dimensional data set - the first of its kind for a cuprate measurement. This enabled a comprehensive analysis of the excitations in this material. We present views of the scattering from a variety of different scattering planes, provide for effective constant energy and constant $\mathbf{Q}$ scans and compliment our results with DFT calculations to determine the phonon contributions to the scattering.

In the end, we find the following key features. We first find that the enhancements features cannot be explained by a simple superposition of inelastic magnetic and phonon scattering. This can be seen both from the dramatically large enhancements of the raw data, the $\mathbf{Q}^2$ normalized analysis indicating that the enhancements are only phonon like at large $|\mathbf{Q}|$ and present significantly more scattered intensity than that of inelastic magnetic hour-glass scattering and from comparisons of our results to our DFT calculations. We interpret our results in terms of a spin-phonon hybridization picture, which, given the doping dependence of these features reported in the next chapter, seems the most plausible underlying cause for this phenomenon. We also present detailed measurements of the $\mathbf{Q}$ dependence and parametrics of these enhancement features. We find that the enhancement features seem temperature independent out to a temperature comparable to the highest 3D C AF ordering temperatures in the 214 system. We also find that the $\mathbf{Q}$ dependence of these features is such that they occupy the same wave-vectors as the magnetic scattering and present as 2D inelastic rods of scattering. Further, we find from our DFT calculations that the likely phonon mode involved in hybridization is similarly quasi-2D and occupies the same wave-vectors as the magnetic scattering. The phonon mode involves oscillations of the Cu-O-Cu separation of the Cu-O plane, providing a natural route to hybridization.

This work has been published as J. J. Wagman, D. Parshall, M. B. Stone, A. T. Savici, Y. Zhao, H. A. Dabkowska, and B. D. Gaulin. In: *Phys. Rev. B* 91 (2015-06), p. 224404. D. Parshall performed the DFT calculations. A. T. Savici assisted with data reduction of the experimental data. M. B. Stone was the instrument scientist for ARCS. Y. Zhao and H. A. Dabkowska grew the sample. B. D. Gaulin supervised the experiment, data analysis and publication preparation. My contribution was to take the lead role in the experiment, all analysis and preparation of the publication.

Quasi-two-dimensional spin and phonon excitations in $La_{1.965}Ba_{0.035}CuO_4$

J. J. Wagman,[1] D. Parshall,[2] M. B. Stone,[3] A. T. Savici,[4] Y. Zhao,[2,5] H. A. Dabkowska,[6] and B. D. Gaulin[1,6,7]

[1]*Department of Physics and Astronomy, McMaster University, Hamilton, Ontario, Canada L8S 4M1*

[2]*NIST Center for Neutron Research, National Institute of Standards and Technology, Gaithersburg, Maryland 20899, USA*

[3]*Quantum Condensed Matter Division, Oak Ridge National Laboratory, Oak Ridge, Tennessee 37831, USA*

[4]*Neutron Data Analysis and Visualization Division, Oak Ridge National Laboratory, Oak Ridge, Tennessee 37831, USA*

[5]*Department of Materials Sciences and Engineering, University of Maryland, College Park, Maryland 20742, USA*

[6]*Brockhouse Institute for Materials Research, McMaster University, Hamilton, Ontario, Canada L8S 4M1*

[7]*Canadian Institute for Advanced Research, 180 Dundas St. W., Toronto, Ontario, Canada M5G 1Z8*

(Received 3 December 2014; revised manuscript received 6 April 2015; published 3 June 2015)

We present time-of-flight inelastic neutron scattering measurements of $La_{1.965}Ba_{0.035}CuO_4$ (LBCO), a lightly doped member of the high temperature superconducting La-based cuprate family. By using time-of-flight neutron instrumentation coupled with single crystal sample rotation we obtain a four-dimensional data set (three **Q** and one energy) that is both comprehensive and spans a large region of reciprocal space. Our measurements identify rich structure in the energy dependence of the highly dispersive spin excitations, which are centered at equivalent $(\frac{1}{2},\frac{1}{2},L)$ wave vectors. These structures correlate strongly with several crossings of the spin excitations with the lightly dispersive phonons found in this system. These effects are significant and account for on the order of 25% of the total inelastic scattering for energies between ≈5 and 40 meV at low $|\mathbf{Q}|$. Interestingly, this scattering also presents little or no L dependence. As the phonons and dispersive spin excitations centered at equivalent $(\frac{1}{2},\frac{1}{2},L)$ wave vectors are common to all members of La-based 214 copper oxides, we conclude such strong quasi-two-dimensional scattering enhancements are likely to occur in all such 214 families of materials, including those concentrations corresponding to superconducting ground states. Such a phenomenon appears to be a fundamental characteristic of these materials and is potentially related to superconducting pairing.

DOI: 10.1103/PhysRevB.91.224404 PACS number(s): 74.25.−q, 75.40.Gb, 78.70.Nx, 74.72.−h

I. INTRODUCTION

The mechanism underlying high temperature superconductivity (HTS) has been intensely debated since the discovery of the first HTS, $La_{2-x}Ba_xCuO_4$ (LBCO) [1]. Much of this research has focused on the correlation between magnetic structures and fluctuations in these systems with their superconducting ground states [2–5]. In the cuprates, this correlation is manifest as the evolution of an insulating, three-dimensional, commensurate antiferromagnet to a superconducting, two-dimensional (2D), incommensurate antiferromagnet with doping [6–12]. This phenomenon is rich, supporting viewpoints spanning those which focus on the competition between the two ground states, to those focused on their proximity and contiguous nature [13–15].

At doping levels for which commensurate antiferromagnetism is lost, the predominant magnetic excitations in La-based cuprates have a characteristic extended hourglass dispersion, which is centered at equivalent $(\frac{1}{2},\frac{1}{2})$ positions within the pseudotetragonal basal plane [16]. The dispersion approaches the commensurate position at an energy scale that is known to be dependent on the concentration of holes introduced into the copper oxide planes [17], before dispersing out towards the Brillouin zone boundary at ≈200–300 meV [18–21]. Notably, these excitations display little $\langle L\rangle$ dependence, indicative of two-dimensional (2D) dynamic spin correlations within a three-dimensional (3D) crystal structure [7,22].

In the last few years a number of studies have turned to investigate the structure in the energy dependence along these dispersive modes. Such studies have appeared for $La_{2-x}Sr_xCuO_4$ (LSCO) [23–26], LBCO [27], as well as both Ni and Zn doped LSCO [28,29], $YBa_2Cu_3O_{6+\delta}$ [30], and $HgBa_2CuO_4$ [31]. In particular, some neutron scattering studies [24–26] on superconducting LSCO have reported striking correlations between superconductivity and a peak in the dynamic susceptibility near 20 meV [25,26]. However, all of these studies focus exclusively on scattering at the smallest $\mathbf{Q}=(\frac{1}{2},\frac{1}{2},L)$ 2D magnetic zone centers (2DMZCs), and do not inform on the comprehensive scattering at larger **Q**, which is determined by both spin and lattice degrees of freedom, as well as any interaction between them.

Here we report inelastic neutron scattering measurements on LBCO with $x=0.035$. This sample is neither superconducting nor a 3D commensurate antiferromagnet. It displays frozen 2D incommensurate magnetic order at low temperatures, similar to LSCO of the same doping [6,7]. As we will report, we find that this sample exhibits large enhancements of its highly dispersive magnetic inelastic scattered intensity at energies that correspond to crossings of the spin excitations with lightly dispersive phonons. In particular, the strongest such enhancements occur at the lowest of such spin-phonon crossings, which are near 15 and 19 meV in LBCO.

II. EXPERIMENTAL DETAILS

Single crystals were grown by the floating zone method and aligned with the HHL plane horizontal [32,33]. The sample was mounted in a closed cycle refrigerator, whose temperature was controlled between 300 K and a base temperature of 7 K. Over this temperature range, the crystal structure for LBCO is orthorhombic with space group $Bmab$ [34,35]. However, since the mismatch between the a and b lattice parameters is slight, we will approximate the crystal structure by the high temperature tetragonal structure of LBCO, whose space

group is $I4/mmm$ with $a = b = 3.78$ Å and $c = 13.2$ Å [36,37]. A consequence of the approximation of the low temperature crystal structure as tetragonal is that the crystal displays zone centers at supercell wave vectors within the pseudotetragonal reciprocal space given by $(\frac{H}{2},\frac{H}{2},2N)$, with H odd. Neutron scattering measurements were performed on the ARCS spectrometer at Oak Ridge National Laboratory using an incident energy of 60 meV. ARCS is a time-of-flight chopper spectrometer with large position-sensitive detector coverage [38]. Coupled with single crystal sample rotation, the resulting four-dimensional (4D) neutron data set (three **Q** dimensions and energy) is comprehensive and reveals the full complexity of the inelastic spectrum below ≈40 meV for $E_i = 60$ meV. Computation reduction and visualization were achieved using Mantid and Horace, respectively [39,40].

III. RESULTS AND DISCUSSION

A. Energy-dependent structure to the dispersive magnetic excitations

Figure 1 shows a representative energy vs wave-vector intensity contour at 7 K. This data, and all the data presented in this paper, have had an empty cryostat data set subtracted from them in order to better isolate the crystal signal from the background due to the cryostat. We discuss this subtraction further in the Supplemental Material [41]. This projection of the master 4D data set employs two integrations. The first is a narrow integration along $\langle H\bar{H}\rangle$. We couple this with a fairly large integration along $\langle L\rangle$. This ensures we capture the full 2D magnetic scattering, which is evident as isotropic rods along $\langle L\rangle$ [see the $(\frac{1}{2},\frac{1}{2})$ rods in the panels of Fig. 3]. As a result, Fig. 1 displays a series of equivalent 2DMZCs ranging from $(\frac{1}{2},-\frac{1}{2})$ to $(-\frac{5}{2},-\frac{7}{2})$. Note that this measurement does not resolve the incommensuration of the magnetic scattering but instead shows highly dispersive rods of inelastic scattering centered on equivalent $(\frac{1}{2},\frac{1}{2})$ positions.

We observe a clear structure in Fig. 1 as a function of energy near the 2DMZCs. Focusing on $(\frac{1}{2},-\frac{1}{2})$, where the

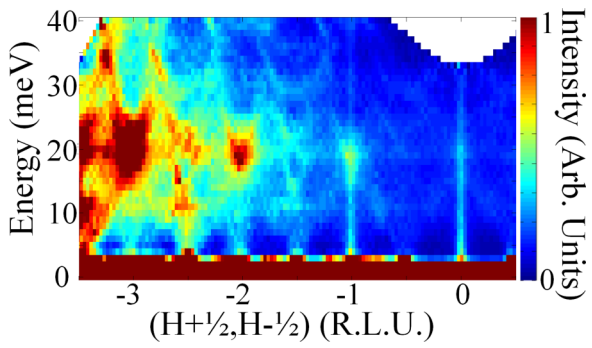

FIG. 1. (Color online) Energy vs wave vector neutron intensity map for $La_{1.965}Ba_{0.035}CuO_4$ showing the scattered neutron intensity along $(H+\frac{1}{2},H-\frac{1}{2})$ at 7 K. The data employ a subtraction of an empty cryostat data set, integration from 0.4 to 0.6 R.L.U. in $\langle H\bar{H}\rangle$ and −4 to 4 R.L.U. in $\langle L\rangle$, where R.L.U. means in units of the reciprocal lattice. The vertical rodlike features, emanating from $(\frac{1}{2},-\frac{1}{2})$ and equivalent 2D magnetic zone centers, are the dispersive magnetic excitations.

magnetic scattering is strongest and the phonon scattering is weakest, the scattered intensity is much greater below ≈19 meV than above. We also see considerable enhancement of the ≈19 meV scattering, which is pronounced at higher-|**Q**| equivalent 2DMZCs, such as $(-\frac{3}{2},-\frac{5}{2})$. We find that this structure develops at the many positions in **Q** and energy that correspond to the crossings of the spin excitations with phonons—particularly the crossing where the low-lying ≈19 meV optic phonon crosses the 2DMZCs [35].

At higher |**Q**| we find that this crossing enhancement grows dramatically in intensity and breadth in both energy and width along **Q**. While purely magnetic scattering drops off with increasing |**Q**| as the square of the magnetic form factor, phonon intensities scale roughly as the magnitude of **Q** squared [42]. Indeed, we see in Fig 1 that away from the spin-phonon crossings, the dispersive rods of magnetic excitations diminish with increasing |**Q**|, while the phonon-dominated nonmagnetic background increases markedly with |**Q**|. Therefore, the large enhancement of the $(-\frac{3}{2},-\frac{5}{2})$ and $(-\frac{5}{2},-\frac{7}{2})$ scattering near ≈19 meV cannot be purely magnetic in origin. The enhancement is also surprisingly strong, given the modest phonon intensities at wave vectors somewhat removed from these 2DMZCs, suggestive that the optic phonons near 2DMZCs qualitatively differ from those away from these wave vectors.

B. Scattering within the HK and HHL planes

We take advantage of the 4D nature of our data to project into another scattering plane. In Fig. 2 we integrate over the same L range as in Fig. 1, but instead we now integrate by ±1 meV in energy to view the scattering in the HK plane. Beginning with the HK maps at 10 and 12 meV (top row of Fig. 2), we can see intense spots of scattering at equivalent 2DMZCs. Again, note the drop in intensity at equivalent positions with higher |**Q**|. Then, by 16 meV, the scattered intensity increases at these 2DMZCs. We emphasize that the scattered intensity at equivalent magnetic wave vectors with higher |**Q**| is now distinguishable from the background unlike at lower energies, which do not correspond to the crossing of spin excitations with phonons. At 18 and 20 meV the scattering at all magnetic positions has increased dramatically in both intensity and breadth in the HK plane—particularly at higher |**Q**|. By 22 meV, clear ringlike excitations develop centered on the 2DMZCs. We identify these rings as arising from optic phonons, which disperse upwards in energy from a minimum near 19 meV at the equivalent $(\frac{1}{2},\frac{1}{2})$ positions. The scattering from these phonons is strongest at high |**Q**| and is difficult to detect at low |**Q**|. Moreover, by 22 meV, the scattered intensity at equivalent 2DMZCs has decreased and is again strongest at low |**Q**|.

We can also explicitly look at the L dependence of the scattering at equivalent 2DMZCs. Figure 3 shows another integration of our 4D data set in energy and $\langle H\bar{H}\rangle$ such that we view reciprocal space maps within the $(H+\frac{1}{2},H-\frac{1}{2},L)$ plane. At energies below the spin-phonon crossing, such as 10 and 12 meV, magnetic rods of scattering, indicative of 2D correlations, are identified only at the low $|\mathbf{Q}| = (\frac{1}{2},-\frac{1}{2},L)$ and $(-\frac{1}{2},-\frac{3}{2},L)$ wave vectors. Between 16 and 20 meV, these rods of scattering become stronger and broader within the HK plane and additional rodlike features appear at equivalent large |**Q**| positions, such as $(-\frac{3}{2},-\frac{5}{2},L)$, similar to the trend

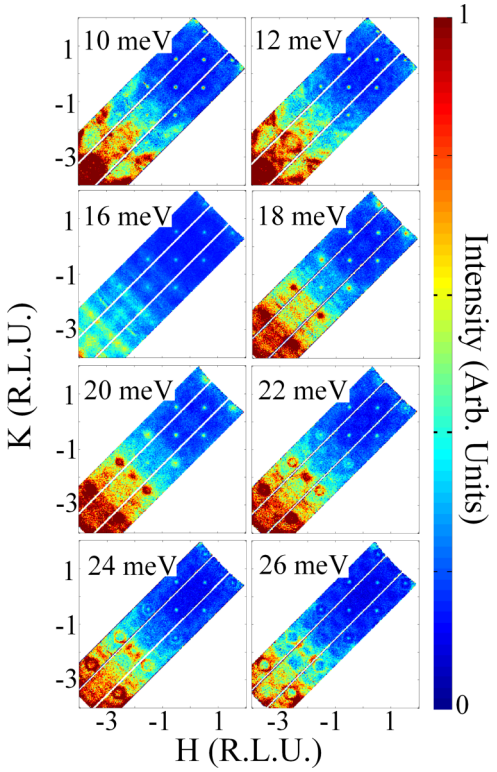

FIG. 2. (Color online) HK reciprocal space maps of the inelastic neutron scattering from $La_{1.965}Ba_{0.035}CuO_4$, showing the scattered neutron intensity in the HK plane at 7 K. The data employ a subtraction of an empty cryostat data set, integration from -4 to 4 in $\langle L\rangle$ and an integration of ± 1 meV in energy about each listed energy. From this projection, the strong spot-shaped features at 10 and 12 meV, centered at equivalent $(\frac{1}{2},\frac{1}{2})$ positions, identify the purely magnetic scattering.

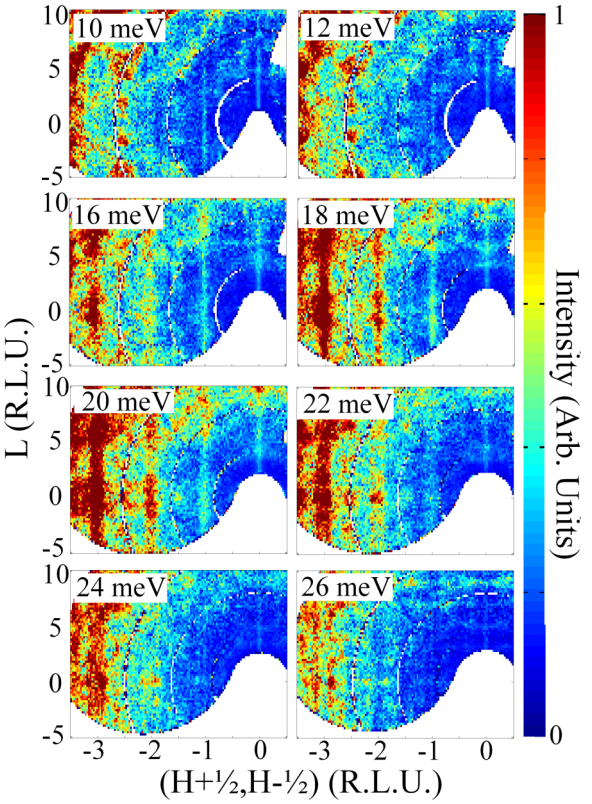

FIG. 3. (Color online) $(H+0.5, H-0.5, L)$ reciprocal space maps of the inelastic neutron scattering from $La_{1.965}Ba_{0.035}CuO_4$ showing the scattered neutron intensity at 7 K. The data employ a subtraction of an empty cryostat data set, integration from -0.1 to 0.1 in $\langle H\bar{H}\rangle$ and an integration of ± 1 meV in energy. From this projection, the vertical, resolution-limited rods of scattering at 10 and 12 meV about $(\frac{1}{2},-\frac{1}{2})$ and $(-\frac{1}{2},-\frac{3}{2})$ identify the purely magnetic scattering. As the phonons begin to contribute at the higher spin-phonon crossing energies, the scattering increases substantially in both breadth and intensity.

seen in Fig. 2. These results show that the inelastic scattering at 2DMZCs between 16 and 20 meV presents as extended rods of scattering along L, at both relatively small $|\mathbf{Q}|$ positions such as $(\frac{1}{2},-\frac{1}{2},L)$, where the scattering would be expected to be magnetic in origin, and at relatively high $|\mathbf{Q}|$ positions such as $(-\frac{5}{2},-\frac{7}{2},L)$, where the scattering would be expected to be mainly due to phonons. This suggests a quasi-2D composite spin-phonon excitation, wherein the relevant phonon eigenvectors would couple strongly to the magnetism in LBCO.

C. Quantitative analysis of the spin-phonon crossings and their temperature dependence

Figure 4 shows the temperature dependence of the energy vs wave-vector maps over a low $|\mathbf{Q}|$ subset of the map shown in Fig. 1. Data are shown at three temperatures: 7, 100, and 300 K, located in Figs. 4(a)–4(c), respectively. These three data sets have been normalized so as to be on the same intensity scale. Interestingly, the structure of the dynamics does not change significantly upon raising temperature, suggesting that the dynamics are independent of the 2D IC ordering temperatures in the system. That said, it is also clear that the scattered intensity increases markedly with temperature. However, this is, to some extent, an expected result emanating from the temperature dependence of the Bose factor. As will become clear, a quantitative analysis is required to understand the temperature dependence of the observed spin fluctuations.

A quantitative analysis of the inelastic scattering at and near the 2DMZCs requires a reliable background estimate. We consider two approaches to this issue. One is to estimate the inelastic background from the inelastic scattering at low temperatures and low $|\mathbf{Q}|$, capturing both the background scattering below the dome of phonon scattering formed by the acoustic phonons, as well as away from the 2DMZC. This background estimate should be largely $|\mathbf{Q}|$ and energy independent and can be subtracted off of the scattered intensity measured as a function of energy at the 2DMZC. Another approach is to use the intensity measured within the basal plane away from the 2DMZC as an energy-dependent background. This energy-dependent background method allows us to remove the background as well as any phonon contribution to the scattering with little dispersion and little $|\mathbf{Q}|$ dependence to their intensity. We relegate the results of this energy-dependent background analysis to our Supplemental Materials [41]. In both methods we employ an additional set of integrations,

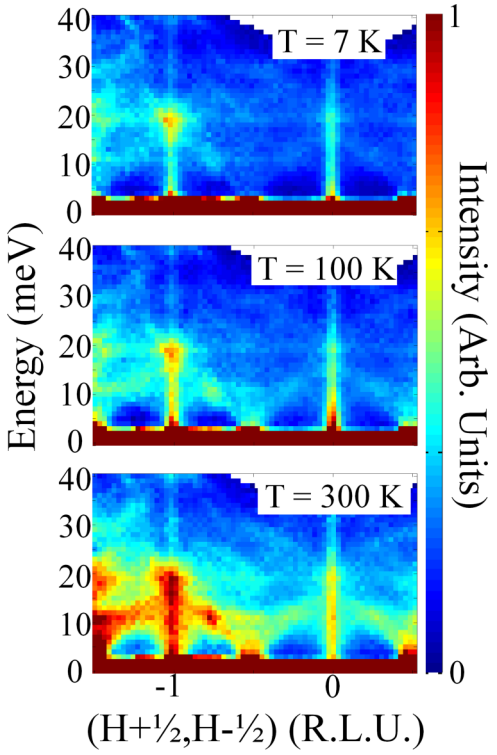

FIG. 4. (Color online) Energy vs wave-vector maps at (a) 7, (b) 100, and (c) 300 K. L has been integrated from -4 to 4 and $H\bar{H}$ has been integrated from 0.4 to 0.6, as in Fig. 1.

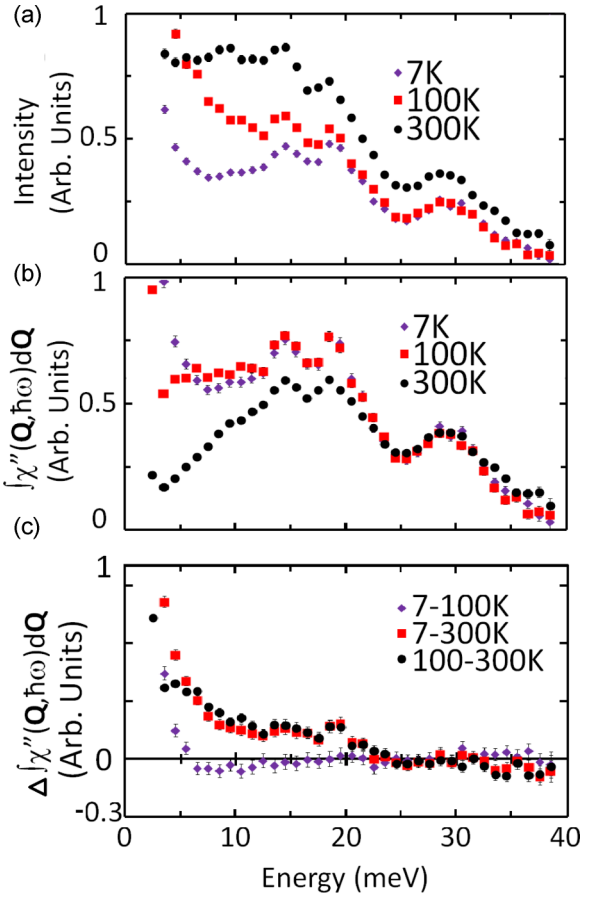

FIG. 5. (Color online) (a) Scattered intensity averaged between areas surrounding $(\frac{1}{2},\frac{1}{2},L)$ and $(-\frac{1}{2},-\frac{1}{2},L)$ are shown as a function of energy at $T = 7$, 100, and 300 K. The data shown are obtained by integrating from -4 to 4 in L, -0.1 to 0.1 in $H\bar{H}$, and 0.4 to 0.6 in HH. Data from integrating the regions ±0.2 to ±0.35 in HH and ±0.6 to ±0.8 with $-4 \leqslant L \leqslant 4$ and $-0.1 \leqslant \bar{H}H \leqslant 0.1$ have been averaged together, and then used as a background in the data shown. (b) $\chi''(\hbar\omega,\mathbf{Q},T)$ obtained from (a) is also shown for $T = 7$, 100, and 300 K. (c) Differences between 7 and 100 K, 7 and 300 K, and 100 and 300 K data sets shown in (b). Error bars represent one standard deviation.

which instead of displaying slices of the data, as those shown in Figs. 1–3, yield effective constant energy and constant-**Q** cuts through the data.

We now analyze the inelastic scattering at the 2DMZC using the background analysis that we described at the beginning of this subsection. As can be seen in Fig. 4, surrounding the $(\pm\frac{1}{2},\pm\frac{1}{2})$ peaks are regions of low scattering intensity, which are bounded by the nearby acoustic phonons. This scattering is largely comprised of incoherent scattering and the sample independent experimental background not captured by the empty cryostat subtraction. We can measure the total background scattering in these four regions by first integrating from $-4 \leqslant L \leqslant 4$ and $-0.1 \leqslant \bar{H}H \leqslant 0.1$. To then obtain the background scattering in these four background regions we further integrate in HH from ±0.2 to ±0.35 and ±0.6 to ±0.8. This yields the total background scattering in these four regions, which we note are quantitatively similar to each other. Given this similarity, we average the results from these four integrations together, and make the approximation that this background is a constant for all energies and **Q**. Our inelastic scattering signal at the 2DMZC is then given by effective constant-**Q** scans obtained by integrating from -4 to 4 in L, -0.1 to 0.1 in $\bar{H}H$, and from ±0.4 to ±0.6 in HH, which we average over the four $(\pm\frac{1}{2},\pm\frac{1}{2})$ positions and display in Fig. 5(a).

The aforementioned background is then subtracted from this signal to produce the inelastic scattering function S(**Q**,$\hbar\omega$) shown in Fig. 5(a) for 7, 100, and 300 K. These three temperatures correspond, respectively, to a temperature within the 2D IC AF frozen magnetic state, a temperature above any 2D IC AF magnetic transitions relevant to any doping x and representative of the "pseudogap" phase, and a temperature relevant to 3D C AF magnetic ordering of the parent compound with $x = 0$, respectively. $S(\mathbf{Q},\hbar\omega,T)$ is itself given by the product of the Bose thermal population factor $n(\hbar\omega + 1)$, which is an analytic function of the ratio of $\hbar\omega$ to temperature and enforces detailed balance, and the imaginary part of the dynamic susceptibility $\chi''(\mathbf{Q},\hbar\omega,T)$. This latter function is the energy-absorbing part of the dynamic susceptibility. It is an odd function of $\hbar\omega$ and contains all the physics of the system of interest. Explicitly,

$$S(\mathbf{Q},\omega,T) = [n(\hbar\omega) + 1]\chi''(\mathbf{Q},\omega,T), \tag{1}$$

where

$$[n(\hbar\omega) + 1] = \frac{1}{1 - e^{-\frac{\hbar\omega}{k_B T}}}. \tag{2}$$

With a robust estimate for the background, and knowing the temperature, it is then straightforward to isolate $\chi''(\mathbf{Q},\hbar\omega,T)$.

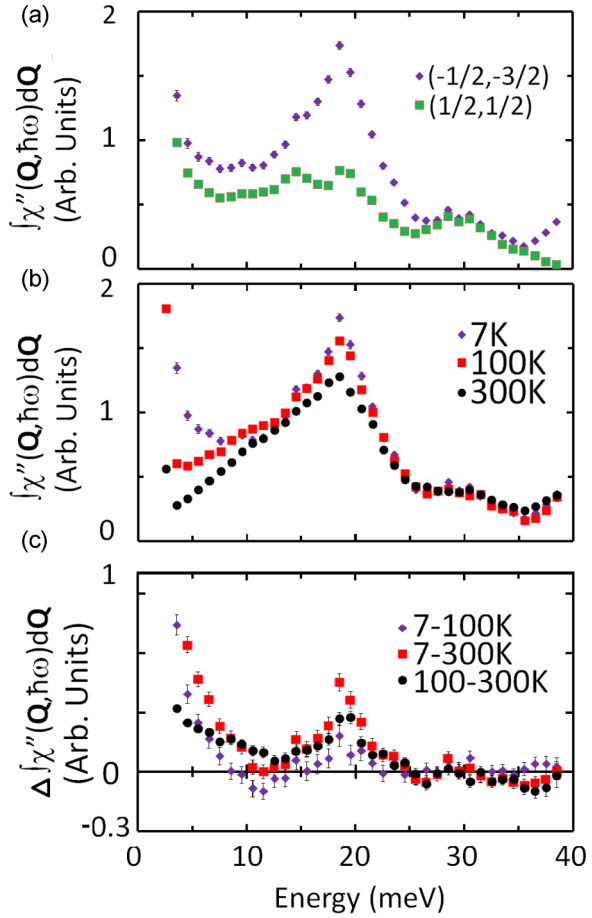

FIG. 6. (Color online) (a) $\chi''(\hbar\omega,\mathbf{Q},T)$ at both $\mathbf{Q}=(\frac{1}{2},\frac{1}{2},L)$, which is also presented in Fig. 5(a), and at $(-\frac{1}{2},-\frac{3}{2},L)$ shown as a function of energy. The data shown are obtained by integrating from -4 to 4 in L, -0.1 to 0.1 in $H\bar{H}$, and 0.4 to 0.6 in HH. Data from integrating the regions ±0.2 to ±0.35 in HH and ±0.6 to ±0.8 with $-4 \leqslant L \leqslant 4$ and $-0.1 \leqslant \bar{H}H \leqslant 0.1$ have been averaged together, and then used as a background in the data shown. The data have been normalized to the same scale as that used in Fig. 5(b). (b) $\chi''(\hbar\omega,\mathbf{Q},T)$ obtained from (a) is also shown for $T=7$, 100, and 300 K. (c) Differences between 7 and 100 K, 7 and 300 K, and 100 and 300 K data sets shown in (b). This intensity scale is the same as that used in Fig. 5(c). Error bars represent one standard deviation.

In Fig. 5(b) we show the integral in $\mathbf{Q}$ around $\mathbf{Q}=(\frac{1}{2},\frac{1}{2},L)$, with the same limits of integration as described above for $S(\mathbf{Q},\hbar\omega,T)$. Figure 5(b) then displays this integral of $\chi''(\mathbf{Q},\hbar\omega,T)$ as a function of energy while Fig. 5(c) shows the difference between this integral of $\chi''(\mathbf{Q},\hbar\omega,T)$ for $T=7$ and 100 K, for $T=7$ and 300 K, and for $T=100$ and 300 K. These results show that the strong enhancement in the $\mathbf{Q}$ integral of $S(\mathbf{Q},\hbar\omega)$ at $\approx$15 and 19 meV is also seen in the $\mathbf{Q}$ integral of $\chi''(\mathbf{Q},\hbar\omega)$ around $\mathbf{Q}=(\frac{1}{2},\frac{1}{2},L)$ at $T=7$ K.

A similar analysis was also carried out for the $\mathbf{Q}=(-\frac{1}{2},-\frac{3}{2},L)$ 2DMZC, using the same background as for $\mathbf{Q}=(\frac{1}{2},\frac{1}{2},L)$. This is shown in Fig. 6, where Fig. 6(a) compares the relevant $\mathbf{Q}$-integrated $\chi''(\mathbf{Q},\hbar\omega)$ from $\mathbf{Q}=(\frac{1}{2},\frac{1}{2},L)$ and $\mathbf{Q}=(-\frac{1}{2},-\frac{3}{2},L)$. We find that the same enhancement of the inelastic scattering occurs near 15 and 19 meV at $T=7$ K at both equivalent 2DMZCs, although the 15 meV enhancement is difficult to resolve when compared to the 19 meV enhancement at $(-\frac{1}{2},-\frac{3}{2},L)$. Similar to Figs. 5(b) and 5(c), Fig. 6(b) shows the temperature dependence of the $\mathbf{Q}$-integrated $\chi''(\mathbf{Q},\hbar\omega,T)$ at $\mathbf{Q}=(-\frac{1}{2},-\frac{3}{2},L)$ as a function of energy, while Fig. 6(c) shows the difference between this integral of $\chi''(\mathbf{Q},\hbar\omega,T)$ for $T=7$ and 100 K, for $T=7$ and 300 K, and for $T=100$ and 300 K.

The temperature dependence of the integral of $\chi''(\mathbf{Q},\hbar\omega,T)$ at the $\mathbf{Q}=(\frac{1}{2},\frac{1}{2},L)$ 2DMZC shown in Fig. 5 is striking, as it shows that all of the difference between this integral at 7 and 100 K is below $\approx$7 meV, while that between either 7 or 100 and 300 K is below $\approx$20 meV. The loss of spectral weight at the 2DMZC on going from the frozen 2D IC magnetic state to the "pseudogap" state at 100 K is at low energies, while most of the spectral weight between 7 and 20 meV remains unchanged. Instead, this 7–20 meV spectral weight diminishes on a temperature scale set by T_N relevant to the undoped parent compound of LBCO with $x=0$. A similar phenomenology is associated with the integral of $\chi''(\mathbf{Q},\hbar\omega,T)$ at the $\mathbf{Q}=(-\frac{1}{2},-\frac{3}{2},L)$ 2DMZC shown in Fig. 6, although the temperature dependent spectral weight is concentrated more in the 15–20 meV regime.

We conclude this section by examining integrals of $\chi''(\mathbf{Q},\hbar\omega)$ at wave vectors of the form $(\frac{n}{2},\frac{n}{2},0)$ with n odd. These are the 2DMZCs such as $\mathbf{Q}=(\frac{1}{2},\frac{1}{2},0)$, etc. The significance of these 2DMZCs with $L=0$ is that the structure factor for all wave vectors of the form $(\frac{n}{2},\frac{n}{2},0)$ are identical within the $I4/mmm$ space group. Thus, the inelastic scattering at these positions should scale only as $|\mathbf{Q}|^2$ if it is due solely to one phonon creation processes.

Figure 7(a) shows the integral of $\chi''(\mathbf{Q},\hbar\omega)$ at such wave vectors of the form $(\frac{n}{2},\frac{n}{2},L)$, over a small range of L about 0, namely $-0.5 \leqslant L \leqslant 0.5$. This integral of $\chi''(\mathbf{Q},\hbar\omega)$ has been corrected for magnetic inelastic scattering at the $(\frac{n}{2},\frac{n}{2},0)$ positions (whose intensity does not scale as $|\mathbf{Q}|^2$), by fitting the scattering at low energies (less than 10 meV) and assuming that this magnetic strength falls off as $\hbar\omega^{-1}$ as is expected for spin waves [43]. This correction may underestimate the magnetic contribution at low energies, but the net effect is to allow $\chi''(\mathbf{Q},\hbar\omega)$ for the 2DMZC with the smallest $|\mathbf{Q}|$, $(-\frac{1}{2},-\frac{1}{2},0)$, to go to $\approx$0 at low energies, as is expected in the absence of magnetic scattering.

Figure 7(b) shows the same integral of $\chi''(\mathbf{Q},\hbar\omega)$ as shown in Fig. 7(a), but now with intensities scaled by $|\mathbf{Q}|^2$. At large $|\mathbf{Q}|$, such as $(-\frac{5}{2},-\frac{5}{2},0)$ and $(-\frac{7}{2},-\frac{7}{2},0)$, where phonon scattering dominates all inelastic scattering, the $\chi''(\mathbf{Q},\hbar\omega)$ integrals overlap very well, as is expected for phonons. However, at $(-\frac{1}{2},-\frac{1}{2},0)$, and, to a considerably lesser extent, $(-\frac{3}{2},-\frac{3}{2},0)$, the data deviate from this $|\mathbf{Q}|^2$ scaling. The scattering at the 2DMZCs corresponding to the smallest $|\mathbf{Q}|$ displays inelastic spectral weight that is much stronger than that expected for phonons alone. From this we conclude that there must be a strong enhancement of the inelastic spectral weight between 15 and 20 meV that is not captured either by one phonon scattering processes or $\hbar\omega^{-1}$ spin waves. This analysis does not eliminate the possibility of a purely magnetic effect. That said, a hybrid spin-phonon origin is more plausible, as the enhanced intensity occurs only at coincidences between the highly dispersive spin excitations at the 2DMZCs and the

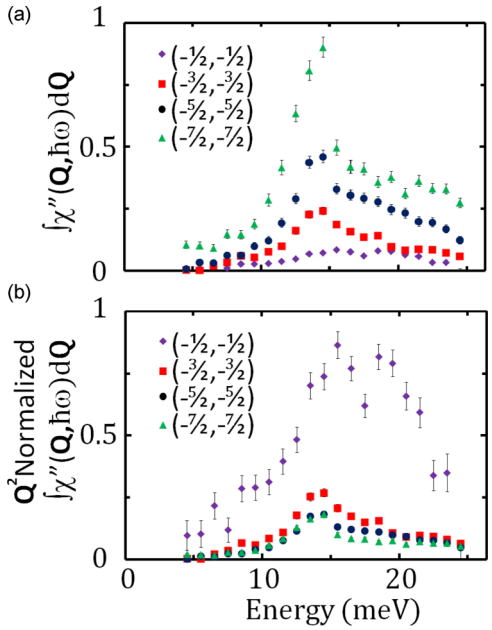

FIG. 7. (Color online) (a) Constant energy cuts of the data using the same HH and $H\bar{H}$ integrations as Figs. 5 and 6, but that also use a very small L integration range. This minimizes contributions from phonon scattering, especially at the lowest $|\mathbf{Q}|$ positions shown. A spin-wave-like background has been subtracted from these data sets and data have also been corrected for the Bose factor, as described in the text. (b) The same constant energy cuts as shown in (a), but with each data set normalized by $|\mathbf{Q}|^2$. Error bars represent one standard deviation.

more weakly dispersive phonons. A related effect appears to occur in superconducting LSCO samples [25]. Independent of its origin, the enhancement is clearly a large and significant effect.

D. Comparison to density functional theory and discussion

The analysis pertaining to Figs. 4–7 reveals a consistent picture of robust enhancement of the inelastic spectrum at the low energy spin-phonon crossings. It is therefore important to, at least qualitatively, understand the nature of the relevant phonons involved. To do this, we turn to density functional theory (DFT) appropriate to La_2CuO_4, whose phonon spectrum should resemble that of LBCO with $x = 0.035$. Calculations were performed using the density functional perturbation approach as implemented in the mixed-basis pseudopotential framework [44,45]. The calculation was performed in the tetragonal structure for La_2CuO_4, with the lattice constants fixed to $a = 3.755\,92$, $c = 13.2275$. Internal parameters (z positions of La and O_4) were optimized to obtain a force-free geometry. The local density approximation was used in the same parametrization employed in Perdew-Wang's work [46]. The calculated phonon dispersion was obtained by interpolation of dynamical matrices, which were calculated on a $2 \times 2 \times 2$ tetragonal mesh. We note that an instability at the M points in the Brillouin zone occurs because the tetragonal structure of pure La_2CuO_4 is not stable at low temperature [34].

Typical results for these calculations are shown in Fig. 8, where we compare these calculations to their appropriate

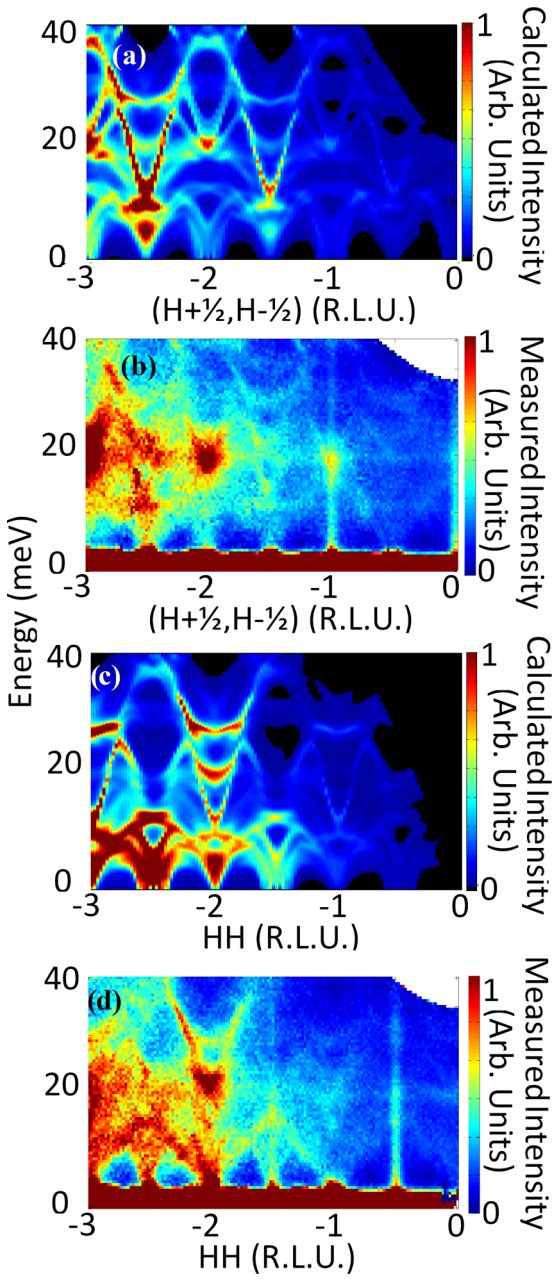

FIG. 8. (Color online) Energy vs wave-vector maps comparing phonon calculations to the neutron scattering data. All data sets integrate in L from -4 to 4 and ± 0.1 about $H\bar{H}$. The calculated and measured dispersion along $(H + \frac{1}{2}, H - \frac{1}{2})$, as obtained by integrating about $H\bar{H} = 0.5$, are shown in (a) and (b), while the calculated and measured dispersion along HH are shown in (c) and (d), respectively. Calculations, which are shown in (a) and (c), display calculated phonon intensities, while the data presented (b) and (d) show the corresponding measured data. The calculated spectra shown in (a) and (c) are normalized to the same arbitrary *calculated* intensity scale, while the measured spectra shown in (b) and (d) are normalized to the same *measured* intensity scale, which is a distinct intensity scale from that used in (a) and (c).

neutron scattering counterparts. In Figs. 8(a) and 8(c) we show the calculated phonon dispersion and intensities along two parallel wave vectors: $(H + \frac{1}{2}, H - \frac{1}{2})$ in Fig. 8(a) and HH in Fig. 8(c). These results can be compared with the

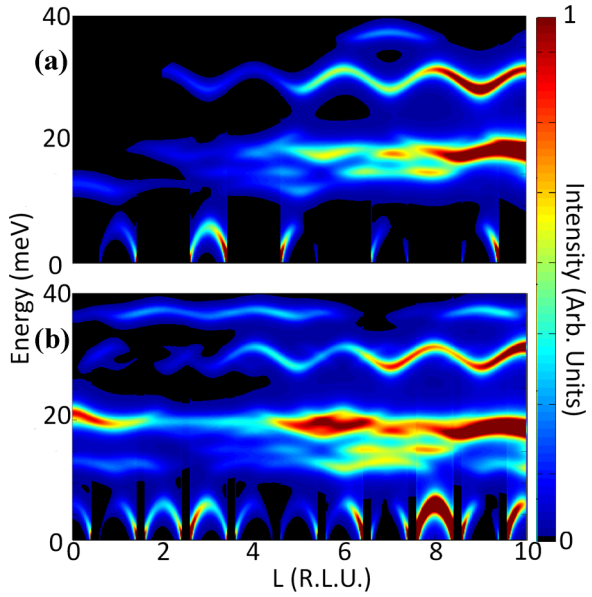

FIG. 9. (Color online) Energy vs L maps of phonon dispersions and intensities from DFT calculations for (a) $\mathbf{Q} = (-\frac{1}{2},-\frac{1}{2},L)$ and (b) $\mathbf{Q} = (-\frac{1}{2},-\frac{3}{2},L)$.

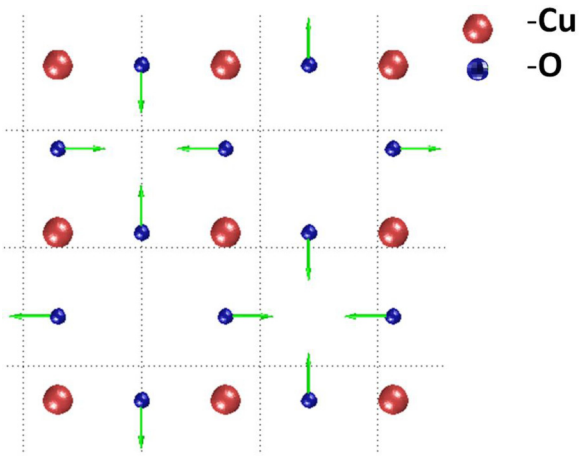

FIG. 10. (Color online) A depiction of the displacements of the ions in La_2CuO_4 for the lightly dispersive ≈19 meV phonon eigenvector at $(\frac{1}{2},\frac{1}{2},0)$. The view is parallel to $\langle 001\rangle$, within the basal plane, showing the motion within the Cu-O plane.

corresponding neutron scattering data shown in Figs. 8(b) and 8(d). All the panels in Fig. 8 have the same integration in $\langle L\rangle$, namely $-4 \leqslant L \leqslant 4$, and both the measured and calculated intensities are shown on a full intensity scale. To illustrate the phonon dispersion, we have convolved our calculations with a resolution function that is narrower than the experimental resolution. From this, a rather hard comparison between the measured and calculated phonon spectra can be made.

We note that the DFT calculation does not capture any magnetic scattering. This can be readily seen as dispersive spin excitations that emanate from the 2DMZCs in the experiment [Figs. 8(b) and 8(d)], but that are absent in the calculation [Figs. 8(a) and 8(c)]. However, the DFT calculation does clearly capture optic phonons that are strong near 19 meV, and disperse upwards and away from the 2DMZCs, as is seen in the experiment. The strongest such optic phonon in the field of view for the $(H+\frac{1}{2},H-\frac{1}{2})$ direction shown in Figs. 8(a) and 8(b) appears just above 20 meV at $H=-3$, which is the $(-\frac{5}{2},-\frac{7}{2})$ position, in both the calculation and the experiment. These comparisons between theory and experiment give us confidence that the DFT calculation is capturing many of the key features in the phonon spectrum for LBCO $x = 0.035$. We can then use these calculations to understand which optic phonons are participating in the strong enhancement to the intensity that we observe at the 2DMZCs shown in Figs. 5–8. We note that at low energies the comparison between calculation and measurement appears less robust. This is caused by a series of phonon branches whose minima occur at less than 0 meV, a consequence of the proximity to a tetragonal to orthorhombic structural transition in this material.

We now consider the energy vs L dependence of the calculated phonons at two wave vectors considered in this paper. These are the $\mathbf{Q} = (-\frac{1}{2},-\frac{1}{2},L)$ and $(-\frac{1}{2},-\frac{3}{2},L)$ 2DMZCs, shown in Figs. 9(a) and 9(b), respectively. At all values of L, we observe relatively strong and dispersionless optic phonons near 30, 19, and 15 meV, although the calculated phonon mode with the largest spectral weight and least dispersion is the 19 meV mode. Focusing on the $(-\frac{1}{2},-\frac{1}{2},L)$ 2DZMC, which presents the largest $|\mathbf{Q}^2|$ normalized enhancements (see Fig. 7), our DFT calculations show that the eigenvector for this ≈19 meV optic phonon involves atomic displacements that correspond primarily to oxygen displacements within the Cu-O basal plane. Moreover, these displacements do not occur for the oxygen within the La-O layers. Such a phonon eigenvector would be expected to possess a very 2D nature, as the stretching of relatively weak bonds in the third dimension are minimal. A similar case can be made for the nature of the optic phonon near 15 meV and the 2DMZC at $(-\frac{1}{2},-\frac{1}{2},L)$, although the isolation of the precise eigenvector of the 15 meV optic phonon is less robust than is the case for the 19 meV optic phonon.

DFT calculations show that the eigenvector for this 19 meV mode is similar to a breathing mode of the in-plane oxygen atoms, centered around the center of the squares comprised of four Cu-O near neighbors, as shown in Fig. 10. While it is unusual for a mode comprised primarily of the lighter oxygen atoms to have such a low frequency, we find that the intensities calculated compare very well with observation, giving us confidence that the calculated eigenvector is correct (the intensity of the mode in various zones is strongly dependent upon the eigenvector). In addition, we note that the oxygen displacements are towards and away from the empty centers of the Cu-O squares, which may be responsible for their low frequency. Our calculated structure factor for this mode is identically zero at $\mathbf{Q} = (\frac{H}{2},\frac{H}{2},0)$ (for H an odd integer). The structure factor for this mode is maximal just off-axis, at $\mathbf{Q} = (\frac{H}{2},\frac{H}{2}+1,0)$. This zone-boundary mode is qualitatively different from the zone-center mode at 20 meV seen at $\mathbf{Q} = (HH0)$. The zone-center mode is an IR-active mode corresponding to motion of the Cu-O plane along the Cu-O bond direction [47].

These results strongly suggest that the large enhancements in the spectral weight observed at the 2DMZCs and near 15 and 19 meV in LBCO with $x = 0.035$ result from the confluence of quasi-2D spin fluctuations with quasi-2D optic phonons

at the same 2D wave vectors. As shown in Fig. 7, it is primarily the lowest $|\mathbf{Q}|$ 2DMZC whose intensity deviates most from the $|\mathbf{Q}|^2$ dependence of the scattered intensity seen at higher $|\mathbf{Q}|$. Therefore, a possible explanation for the origin of this strong enhancement is hybridization between the quasi-2D spin fluctuations and quasi-2D phonons. Such an interpretation would be natural as the atomic displacements involved in the quasi-2D optic phonons are such that Cu-O-Cu bonds are stretched and distorted. Such distortions affect the nature of the strongest Cu-Cu superexchange pathways in the LBCO system. Independent of the precise origin of this resonant enhancement of the inelastic spectrum in LBCO, it is clear that the energy scale of these effects, which is $\approx$200 K, is large and large enough to play a role in the mechanism underlying high temperature superconductivity which occurs on the same temperature scale. However, any firm connection to superconductivity is lacking at present.

IV. CONCLUSIONS

To conclude, comprehensive time-of-flight neutron scattering measurements have observed rich structure in the energy dependence of the inelastic scattering at 2DMZCs, in particular at those at the lowest-$|\mathbf{Q}|$, such as $(\frac{1}{2},\frac{1}{2},L)$. This structure presents in the form of strong enhancements of the spectral weight at several crossings of highly dispersive spin excitations with relatively dispersionless phonons in LBCO with $x = 0.035$. The measured enhancements are large and account for as much as $\approx$25% of the spectral weight between 5 and 40 meV at the lowest-$|\mathbf{Q}|$ 2DMZC.

Modeling the phonons in La_2CuO_4 with density functional theory allowed us to identify the likely eigenvectors associated with the optic phonons involved in the enhancements. These phonon modes appear to be quasi-2D themselves, with appropriate atomic displacements that could affect the strongest Cu-O-Cu superexchange pathways.

This robust structure within the excitation spectrum at the 2DMZCs in LBCO appears on a high energy scale and therefore is of potential relevance to high temperature superconductivity itself. While the current study was carried out on a nonsuperconducting sample, both the quasi-2D spin fluctuations and the nature of the phonon spectrum for this material family should be slowly varying as a function of doping. We also note that superconducting ground states in LBCO form for $x > 0.05$, which is only a modest change in x from the present sample. Therefore, the reported energy dependence in the 2DMZC spectral weight, resulting from a confluence of quasi-2D spin fluctuations and quasi-2D optic phonons, is likely a common feature for a broad range of concentrations relevant to superconductivity in the LBCO system.

ACKNOWLEDGMENTS

We would like to acknowledge useful conversations had with T. Timusk, J. P. Carbotte, I. A. Zaliznyak, J. M. Tranquada, G. E. Granroth, S. A. Kivelson, S. D. Wilson, N. B. Christensen, J. Gaudet, B. Jackel, and J. L. Niedziela. Research at ORNL's Spallation Neutron Source was sponsored by the Scientific User Facilities Division, Office of Basic Energy Sciences, US Department of Energy. This work was supported by NSERC of Canada.

[1] J. G. Bednorz and K. A. Muller, Z. Phys. B **64**, 189 (1986).
[2] T. Timusk and B. Statt, Rep. Prog. Phys **62**, 61 (1999).
[3] M. Fujita, H. Hiraka, M. Matsuda, M. Matsuura, J. M. Tranquada, S. Wakimoto, G. Xu, and K. Yamada, J. Phys. Soc. Jpn. **81**, 011007 (2012).
[4] R. J. Birgeneau, C. Stock, J. M. Tranquada, and K. Yamada, J. Phys. Soc. Jpn. **75**, 111003 (2006).
[5] M. A. Kastner, R. J. Birgeneau, G. Shirane, and Y. Endoh, Rev. Mod. Phys. **70**, 897 (1998).
[6] B. Keimer, N. Belk, R. J. Birgeneau, A. Cassanho, C. Y. Chen, M. Greven, M. A. Kastner, A. Aharony, Y. Endoh, R. W. Erwin, and G. Shirane, Phys. Rev. B **46**, 14034 (1992).
[7] J. J. Wagman, G. Van Gastel, K. A. Ross, Z. Yamani, Y. Zhao, Y. Qiu, J. R. D. Copley, A. B. Kallin, E. Mazurek, J. P. Carlo, H. A. Dabkowska, and B. D. Gaulin, Phys. Rev. B **88**, 014412 (2013).
[8] N. Doiron-Leyraud, C. Proust, D. Leboeuf, J. Levallois, J.-B. Bonnemaison, R. Liang, D. A. Bon, W. N. Hardy, and L. Taillefer, Nature (London) **447**, 565 (2007).
[9] C. Stock, W. J. L. Buyers, Z. Yamani, Z. Tun, R. J. Birgeneau, R. Liang, D. Bonn, and W. N. Hardy, Phys. Rev. B **77**, 104513 (2008).
[10] M. Enoki, M. Fujita, T. Nishizaki, S. Iikubo, D. K. Singh, S. Chang, J. M. Tranquada, and K. Yamada, Phys. Rev. Lett. **110**, 017004 (2013).
[11] N. P. Armitage, P. Fournier, and R. L. Greene, Rev. Mod. Phys. **82**, 2421 (2010).
[12] L. Taillefer, Annu. Rev. Condens. Matter Phys. **1**, 51 (2010).
[13] S. Sachdev, M. A. Metlitski, and M. Punk, J. Phys.: Condens. Matter **24**, 294205 (2012).
[14] S. A. Kivelson, I. P. Bindloss, E. Fradkin, V. Oganesyan, J. M. Tranquada, A. Kapitulnik, and C. Howald, Rev. Mod. Phys. **75**, 1201 (2003).
[15] B. Lake, H. M. Runnow, N. B. Christensen, G. Aeppli, K. Lefmann, D. F. McMorrow, P. Vorderwisch, P. Smeibidl, N. Mangkorntong, T. Sasagawa, M. Nohara, H. Takagi, and T. E. Mason, Nature (London) **415**, 299 (2002).
[16] S. M. Hayden, G. Aeppli, T. G. Perring, H. A. Mook, and F. Doğan, Phys. Rev. B **54**, R6905(R) (1996).
[17] M. Matsuda, M. Fujita, S. Wakimoto, J. A. Fernandez-Baca, J. M. Tranquada, and K. Yamada, Phys. Rev. Lett. **101**, 197001 (2008).
[18] R. Coldea, S. M. Hayden, G. Aeppli, T. G. Perring, C. D. Frost, T. E. Mason, S.-W. Cheong, and Z. Fisk, Phys. Rev. Lett. **86**, 5377 (2001).
[19] N. S. Headings, S. M. Hayden, R. Coldea, and T. G. Perring, Phys. Rev. Lett. **105**, 247001 (2010).
[20] J. M. Tranquada, H. Woo, T. G. Perring, H. Goka, G. D. Gu, G. Xu, M. Fujita, and K. Yamada, Nature (London) **429**, 534 (2004).

[21] S. M. Hayden, G. Aeppli, H. A. Mook, T. G. Perring, T. E. Mason, S.-W. Cheong, and Z. Fisk, Phys. Rev. Lett. **76**, 1344 (1996).
[22] K. Machida and M. Ichioka, J. Phys. Soc. Jpn. **68**, 2168 (1999).
[23] M. Matsuda, G. E. Granroth, M. Fujita, K. Yamada, and J. M. Tranquada, Phys. Rev. B **87**, 054508 (2013).
[24] N. B. Christensen, D. F. McMorrow, H. M. Rønnow, B. Lake, S. M. Hayden, G. Aeppli, T. G. Perring, M. Mangkorntong, M. Nohara, and H. Tagaki, Phys. Rev. Lett. **93**, 147002 (2004).
[25] O. J. Lipscombe, B. Vignolle, T. G. Perring, C. D. Frost, and S. M. Hayden, Phys. Rev. Lett. **102**, 167002 (2009).
[26] B. Vignolle, S. M. Hayden, D. F. McMorrow, H. M. Ronnow, B. Lake, C. D. Frost, and T. G. Perring, Nat. Phys. **3**, 163 (2007).
[27] Z. Xu, C. Stock, S. Chi, A. I. Koleshnikov, G. Xu, G. D. Gu, and J. M. Tranquada, Phys. Rev. Lett. **113**, 177002 (2014).
[28] S. D. Wilson, Z. Yamani, C. Dhital, B. Freelon, P. G. Freeman, J. A. Fernandez-Baca, K. Yamada, S. Wakimoto, W. J. L. Buyers, and R. J. Birgeneau, Phys. Rev. B **85**, 014507 (2012).
[29] M. Matsuura, M. Fujita, H. Hiraka, M. Kofu, H. Kimura, S. Wakimoto, T. G. Perring, C. D. Frost, and K. Yamada, Phys. Rev. B **86**, 134529 (2012).
[30] C. Stock, W. J. L. Buyers, R. Liang, D. Peets, Z. Tun, D. Bonn, W. N. Hardy, and R. J. Birgeneau, Phys. Rev. B **69**, 014502 (2004).
[31] Y. Li, G. Yu, M. K. Chan, V. Valedent, N. Li, Y. Barisic, X. Zhao, K. Hradil, R. A. Mole, Y. Sidis, P. Steffens, P. Bourches, and M. Greven, Nat. Phys. **8**, 404 (2012).
[32] M. Fujita, K. Yamada, H. Hiraka, P. M. Gehring, S. H. Lee, S. Wakimoto, and G. Shirane, Phys. Rev. B **65**, 064505 (2002).
[33] S. R. Dunsiger, Y. Zhao, B. D. Gaulin, Y. Qiu, P. Bourges, Y. Sidis, J. R. D. Copley, A. Kallin, E. M. Mazurek, and H. A. Dabkowska, Phys. Rev. B **78**, 092507 (2008).
[34] Y. Zhao, B. D. Gaulin, J. P. Castellan, J. P. C. Ruff, S. R. Dunsiger, G. D. Gu, and H. A. Dabkowska, Phys. Rev. B **76**, 184121 (2007).
[35] J. D. Axe, A. H. Moudden, D. Hohlwein, D. E. Cox, K. M. Mohanty, A. R. Moodenbaugh, and Y. Xu, Phys. Rev. Lett. **62**, 2751 (1989).
[36] S. Katano, J. A. Fernandez-Baca, S. Funahashi, N. Mori, Y. Ueda, and K. Koga, Physica C **214**, 64 (1993).
[37] C.-H. Lee, K. Yamada, Y. Endoh, G. Shirane, R. J. Birgeneau, M. A. Kastner, M. Greven, and Y-J. Kim, J. Phys. Soc. Jpn. **69**, 1170 (2000).
[38] D. L. Abernathy, M. B. Stone, M. J. Loguillo, M. S. Lucas, O. Delaire, X. Tang, J. Y. Y. Lin, and B. Fultz, Rev. Sci. Instrum. **83**, 015114 (2012).
[39] O. Arnold, J. C. Bilheux, J. M. Borreguero, A. Buts, S. I. Campbell, L. Chapon, M. Doucet, N. Draper, R. Ferraz Leal, M. A. Gigg, V. E. Lynch, A. Markvardsen, D. J. Mikkelson, R. L. Mikkelson, R. Miller, K. Palmen, P. Parker, G. Passos, T. G. Perring, P. F. Peterson, S. Ren, M. A. Reuter, A. T. Savici, J. W. Taylor, R. J. Taylor, R. Tolchenov, W. Zhou, and J. Zikovsky, Nucl. Instrum. Methods Phys. Res. Sect. A **764**, 156 (2014).
[40] http://horace.isis.rl.ac.uk/Main_Page.
[41] See Supplemental Material at http://link.aps.org/supplemental/10.1103/PhysRevB.91.224404 for a discussion of the strength and form of empty can background scattering, and the results of an energy-dependent background subtraction analysis.
[42] G. L. Squires, *Introduction to the Theory of Thermal Neutron Scattering* (Dover, New York, 1978).
[43] G. Shirane, S. M. Shapiro, and J. M. Tranquada, *Neutron Scattering with a Triple-Axis Spectrometer* (Cambridge University Press, Cambridge, 2002).
[44] B. Meyer, C. Elsässer, and M. Fähnle, FORTRAN90 Program for Mixed-Basis Pseudopotential Calculations for Crystals, Max-Planck-Institut für Metallforschung, Stuttgart (unpublished).
[45] R. Heid and K.-P. Bohnen, Phys. Rev. B **60**, R3709 (1999).
[46] J. P. Perdew and Y. Wang, Phys. Rev. B **45**, 13244 (1992).
[47] S. Sugai, Phys. Rev. B **39**, 4306 (1989).

Supplemental Material: Quasi-Two Dimensional Spin and Phonon Excitations in $La_{1.965}Ba_{0.035}CuO_4$

J.J. Wagman,[1] D. Parshall,[2] M. B. Stone,[3] A.T. Savici,[4] Y. Zhao,[2,5] H.A. Dabkowska,[6] and B.D. Gaulin[1,6,7]

[1]*Department of Physics and Astronomy, McMaster University, Hamilton, Ontario, L8S 4M1, Canada*
[2]*NIST Center for Neutron Research, National Institute of Standards and Technology, Gaithersburg, Maryland 20899, USA*
[3]*Quantum Condensed Matter Division, Oak Ridge National Laboratory, Oak Ridge, Tennessee 37831, USA*
[4]*Neutron Data Analysis and Visualization Division, Oak Ridge National Laboratory, Oak Ridge, Tennessee 37831, USA*
[5]*Department of Materials Sciences and Engineering, University of Maryland, College Park, Maryland 20742, USA*
[6]*Brockhouse Institute for Materials Research, McMaster University, Hamilton, Ontario, L8S 4M1, Canada*
[7]*Canadian Institute for Advanced Research, 180 Dundas St. W., Toronto, Ontario, M5G 1Z8, Canada*

I. BACKGROUND SUBTRACTION

We first discuss the measurement of the empty sample can background for the inelastic neutron scattering data presented in the main manuscript, its origin and magnitude. We explicitly show that this background constitutes a small fraction, $\approx$ 2-3 % or less, of the total coherent neutron scattering at small $|\mathbf{Q}|$, and thus can readily be corrected for by subtracting an empty sample can data set, from the "signal" data sets with the sample in place.

The determination of the background is generally important for any scattering experiment[1]. It can display structure as a function of $|\mathbf{Q}|$ and energy, or both, which can mimic scattering from the sample. It can also contribute to multiple scattering, if it is sufficiently strong. Indeed, this latter effect has been the subject of recent neutron scattering measurements[2]. Moreover, as discussed in the main paper, the isolation of $\chi''(\mathbf{Q},\hbar\omega)$ from the measured $S(\mathbf{Q},\hbar\omega)$ requires that the background be well determined such that the Bose thermal population is applied only to the signal and not to the background. Consequently, understanding and accounting for the background is important to the quantitative analysis that we performed here and is common to many inelastic neutron scattering studies.

In most neutron scattering experiments, and certainly in the present experiment, the primary source of background is scattering from the adenda. The adenda are comprised from the mount for the single crystal, any radiation shields that are in place and other parts of the cryostat that may be in the neutron beam. These adenda are made from machined aluminum, which is used because Al has a low coherent and incoherent neutron cross sections, has little neutron absorbtion and is easily machined. The neutron scattering from the adenda is therefore expected to be weak.

Despite the weak contributions of the adenda, care is taken to minimize the amount of material from the adenda in the neutron beam and to shield as much of this remaining material as possible by using strong neutron absorbers. In the present experiment, we employed a cadmium mask over much of the sample mount. "Empty can" measurements are then collected. These measurements are scans performed without the sample in place but with the adenda still present. Such scans then serve as a measurement of the background. and it is these empty can data sets that are subtracted from those data sets collected with the aligned sample in place. All the data presented in the main manuscript is this background-corrected data. Here, we demonstrate the relative strength of the measured background to the measured signal.

Figures S1, S2, and S3 show Energy vs. $(H+\frac{1}{2}, H-\frac{1}{2})$, K vs. H, and L vs. $(H+\frac{1}{2}, H-\frac{1}{2})$ maps of the inelastic neutron scattering from our $La_{1.965}Ba_{0.035}CuO_4$ experiment, with the scattered neutron intensity shown on full scale. We note that Figs. S1 c), S2 c) and S3 c) are the same empty can background-corrected data sets that were presented and discussed in the main manuscript. Figs. S1 a), S2 a) and S3 a) show the original raw data, without subtraction of the empty can data, displayed on the same intensity scale as S1 c), S2 c), and S3 c). Figs. S1 b), S2 b), and S3 b) show the results from the "empty can" measurements alone. We present these data on a full intensity scale that is only 6 % of of the full intensity scale we show for the "signal" scans. This clearly shows that the measured background is a small correction to the scattered intensity from the sample, especially at small $|\mathbf{Q}|$. We therefore conclude that our background subtraction of these data sets is robust, and multiple scattering involving the adenda is not a significant issue for this experiment, especially at low $|\mathbf{Q}|$.

II. ENERGY DEPENDENT BACKGROUND ANALYSIS

Once the "empty can" background has been removed from a data set, one may still wish to isolate a signal of a specific origin, such as magnetic scattering, which has a specific wave-vector dependence, from another sig-

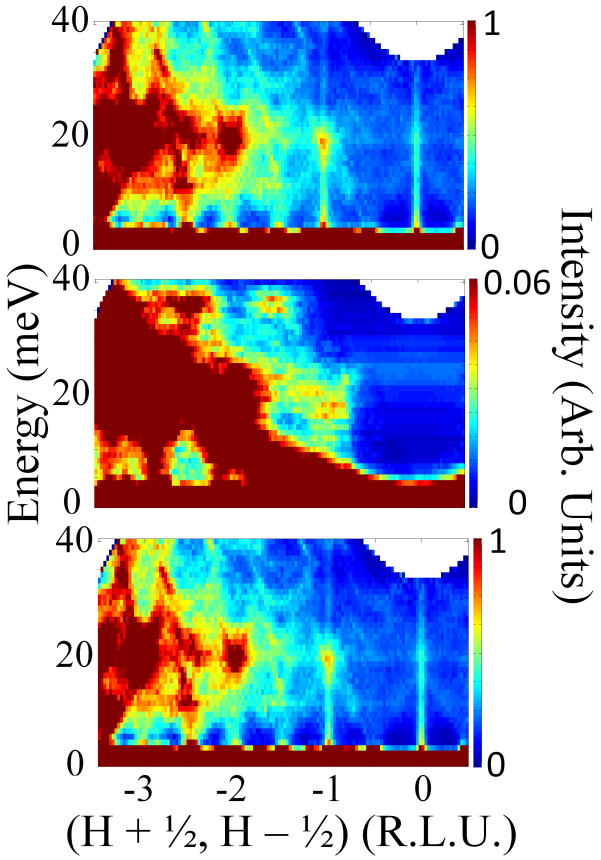

FIG. S1. Energy vs. wave-vector maps produced nearly identically to Fig. 1 of the main manuscript. The only distinction here is that instead of integrating from 0.4 to 0.6 in $\bar{H}H$, as was done in Fig. 1 of the main manuscript, here we integrate from -0.1 to 0.1. a) A normalized signal data set with no empty can subtraction is shown. b) A normalized empty sample can data set on an intensity scale 6% of that of either a) or c) is shown. c) A normalized signal minus background data set is shown on the same intensity scale as in a). This is the same data as presented in Fig. 1 of the main manuscript. All data sets shown were collected at 7 K.

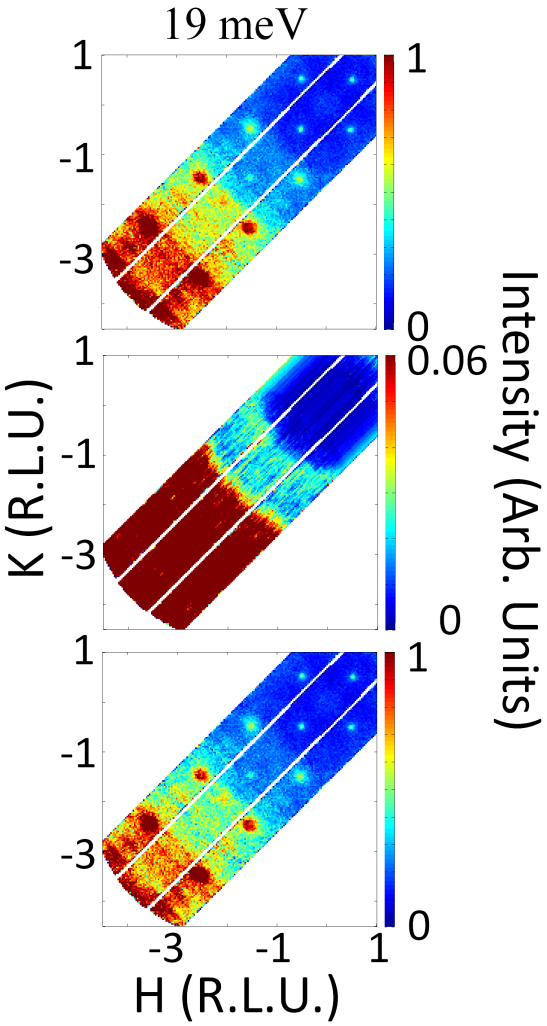

FIG. S2. HK maps produced identically to Fig. 2 of the main manuscript. These maps all present data at 19 meV. a) A normalized signal data set with no empty can subtraction is shown. b) A normalized empty sample can data set on an intensity scale 6% of that of either a) or c) is shown. c) A normalized signal minus background data set is shown on the same intensity scale as in a). This is the same data as presented in Fig. 2 of the main manuscript. All data sets shown were collected at 7 K.

nal, such as phonon scattering, which has a different wave-vector dependence. Below we present an alternate approach to estimating the scattered intensity that occurs at the 2DMZCs to that presented in the main manuscript. With this approach, we use the intensity measured within the basal plane away from the 2DMZCs as an energy-dependent background. This energy dependent background method accounts for phonon contributions with little dispersion and $|\mathbf{Q}|$ dependence to their intensity. As in the main manuscript, in using this method we employ an additional set of integrations, which, instead of displaying slices of the data, as those shown in Figs. 1 to 3 of the main manuscript, yield effective constant energy cuts through the data.

We now consider such constant energy cuts along HH through, and in the vicinity of, $(\frac{1}{2}, \frac{1}{2})$, which is achieved by integrating in energy, $H\bar{H}$ and L. We chose this position in reciprocal space as it is the 2DMZC with the smallest $|\mathbf{Q}|$, implying that it has minimal contributions to the scattered intensity from phonons and maximal contributions from purely magnetic scattering. We display a series of such representative cuts from 10 meV to 26 meV in Fig. S4. The solid lines in this figure are fits using a Gaussian centered at $(\frac{1}{2}, \frac{1}{2})$ to represent the scattering at the 2DMZC plus a linear background, which is a phenomenological fit for contributions from

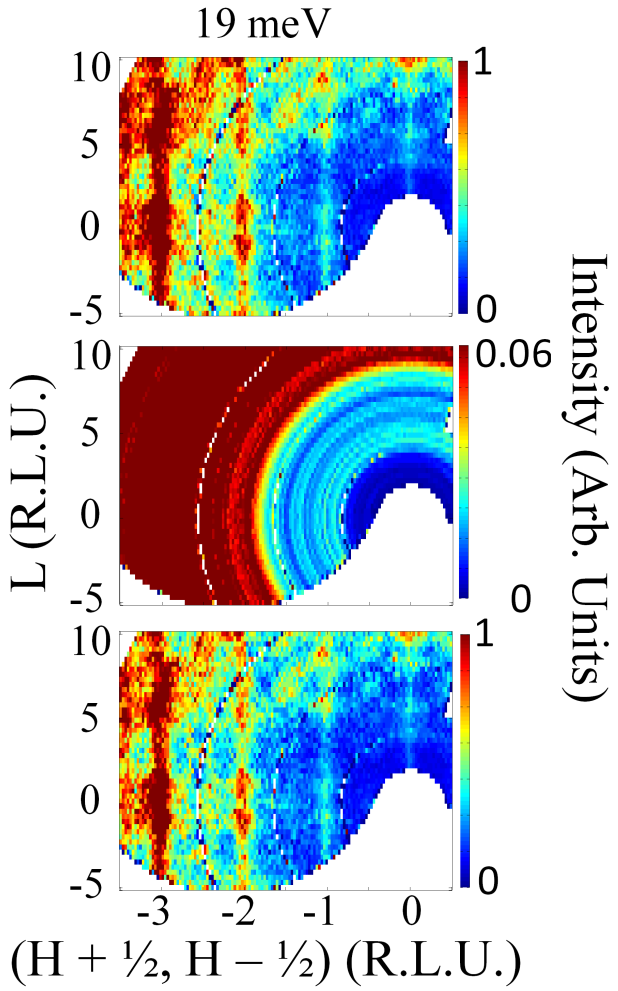

FIG. S3. $(H+\frac{1}{2}, H-\frac{1}{2})L$ maps produced identically to Fig. 3 of the main manuscript. These maps all present data at 19 meV. a) A normalized signal data set with no empty can subtraction is shown. b) A normalized empty sample can data set on an intensity scale 6% of that of either a) or c) is shown. c) A normalized signal minus background data set is shown on the same intensity scale as in a). This is the same data as presented in Fig. 3 of the main manuscript. All data sets shown were collected at 7 K.

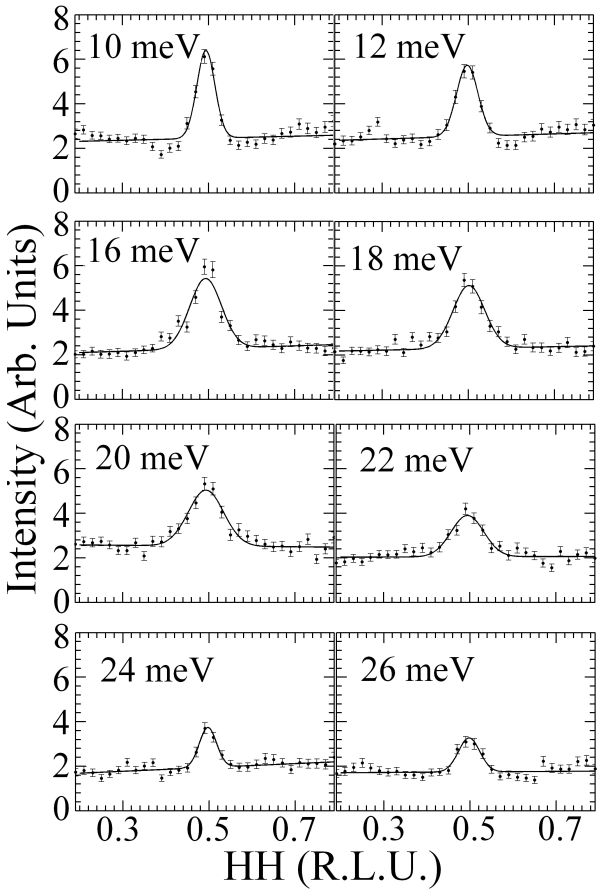

FIG. S4. Evolution of the integrated inelastic neutron scattering intensity near $(\frac{1}{2}, \frac{1}{2})$ as a function of energy as observed in a series of constant energy cuts integrating -4 to 4 in $< L >$, -0.1 to 0.1 in $< H\bar{H} >$ and ± 1 meV in energy. Solid lines are fits of the data, where the peaks are modeled as Gaussians and the background is modeled phenomenologically as a sloping linear background.

relatively dispersionless phonons. As can be seen in Fig. S4, the background is largely linear in HH, although it can display somewhat more complex wavevector structure. Nonetheless, we can phenomenologically model these trends and thereby isolate the nominal scattering centered on the $(\frac{1}{2}, \frac{1}{2})$ 2DMZC position.

Figure S5 a) shows an energy vs. $< HH >$ wavevector map featuring the $(\frac{1}{2}, \frac{1}{2})$ and $(-\frac{1}{2}, -\frac{1}{2})$ 2DMZC positions. This plot is similar to that shown in Fig. 1 of the main manuscript, however there we presented the inelastic scattering spectrum through 4 2DMZCs, as a function of $< H+1/2, H-1/2 >$ with systematically decreasing $|\mathbf{Q}|$ from left to right. We note that the reciprocal space direction shown in Fig. 1 of the main manuscript is parallel to $< HH >$. Here, Fig. S5 a) again highlights the structure that develops at several of the spin-phonon dispersion crossings in this system.

Figure S5 b) displays the resulting energy dependence of the integrated scattered intensity centered on $(\frac{1}{2}, \frac{1}{2})$, which we take to be the area of the Gaussian fits in Fig. S4. It shows the $(\frac{1}{2}, \frac{1}{2})$ scattering to fall dramatically between 5-10 meV before rising by factors of 3-4 between 15-20 meV. For context, the characteristic energy dependence of the integrated intensity for spin waves is expected to diminish as $\frac{1}{\hbar\omega}$.[1] The dashed line in Fig. S5 b) is the result of modeling the scattering away from any spin-phonon crossings by a phenomenological form of $E^{-1.2}$. This model provides a good description of the data at low energies and is suggestive of the energy dependence from spin excitations that exist away from the crossings with the various phonons. Fig. S5 b)

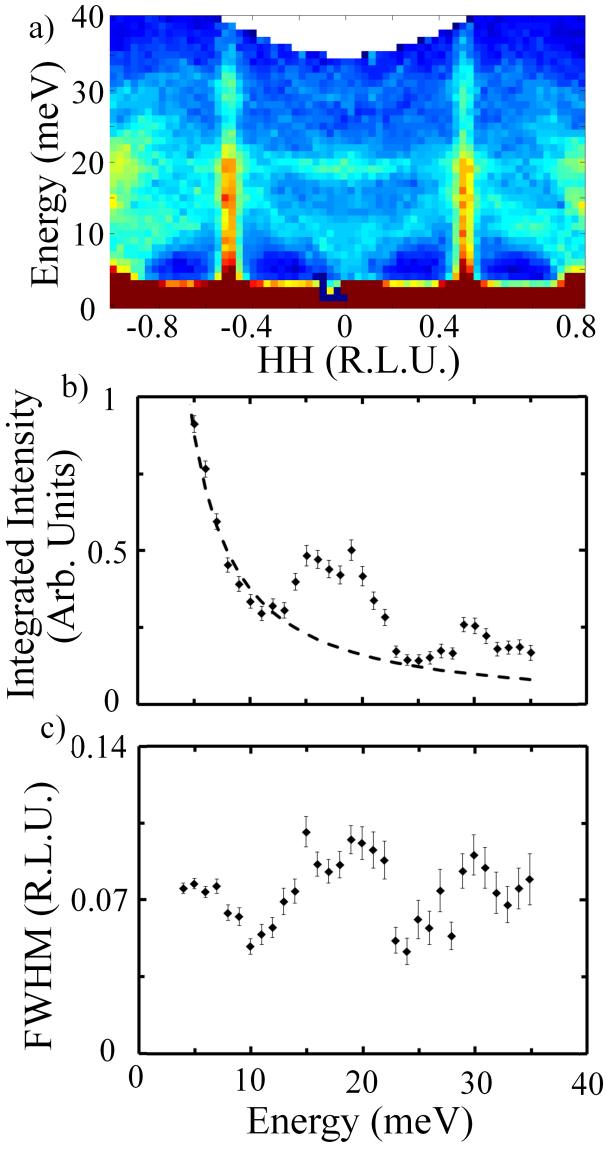

FIG. S5. a) An expanded view of the $(\frac{1}{2},\frac{1}{2})$ and $(-\frac{1}{2},-\frac{1}{2})$ 2DMZCs, integrating -4 to 4 in L, and -0.1 to 0.1 in $H\bar{H}$. This contour map again displays the rich structure that develops at the crossings of the dispersive spin excitations with the phonons in this system. b) Resultant integrated intensity at the 2DMZC $(\frac{1}{2},\frac{1}{2})$ positions from phenomenological modelling. The integrated intensity is the area of the Gaussians employed in the fits, as shown in Fig. S4. The dashed curve is a phenomenological curve of best fit, which we find to go as $E^{-1.2}$, likely due to the large L integration we use here. This curve is suggestive of the energy dependence resultant from spin excitations alone and serves to demonstrate the dramatic nature of the enhancement of the scattering at the spin-phonon crossings between 10 meV and 40 meV. c) Corresponding full width half maximum (FWHM) obtained from the Gaussian fits of the data from Fig. S4. These give the FWHM as measured along the HH direction. Error bars represent one standard deviation. In this case, the integration range reflects that we have employed an energy, L and $H\bar{H}$ integration, as described in the the text, in addition a fit along HH.

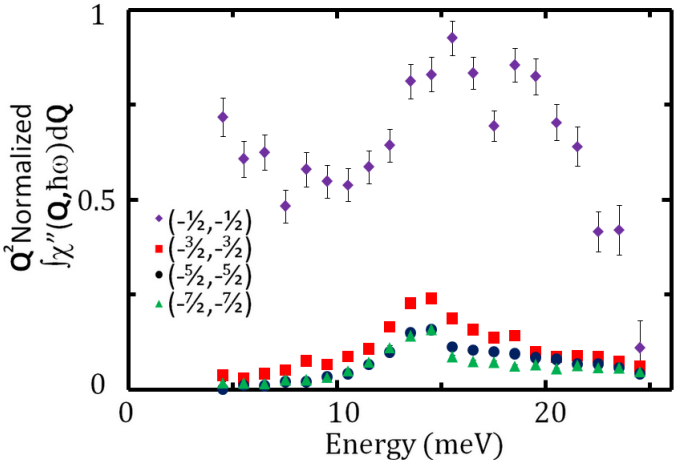

FIG. S6. Constant energy cuts of the $|\mathbf{Q}|^2$-normalized $\chi''(\mathbf{Q},\hbar\omega)$ at the 2DMZCs measured. These data sets are analogous to those shown in Fig. 7 b), with the same regions of $\mathbf{Q}$-integration, but no estimate or subtraction of a spin wave contribution to the spectal weight has been performed. The same large enhancement of $|\mathbf{Q}|^2$-normalized $\chi''(\mathbf{Q},\hbar\omega)$ is observed as in Fig. 7 b).

demonstrates, therefore, the surprisingly large scale of this enhancement. This enhancement occurs at all three spin-phonon crossings within this field of view: at $\approx$ 15 meV, $\approx$ 19 meV and $\approx$ 30 meV, which is where the low energy and relatively dispersionless optic phonon bands cross the 2DMZC. A simple estimate of the scattered intensity due to this enhancement suggests that at $(\frac{1}{2},\frac{1}{2})$ approximately 25% of the total scattered intensity below 40 meV arises from these spin-phonon crossings.

Figure S5 c) shows the corresponding full width half maximum (FWHM) obtained from the Gaussian fits of the scattering at the 2DMZC. Note that the FWHM first deceases by almost of factor of 2 between 5 meV and $\approx$10 meV, which corresponds to the hour-glass dispersion of the 2D incommensurate spin excitations. This is consistent with earlier work on the LSCO system, which shows that the "waist" of the hour-glass occurs around $\approx$11 meV for a doping of x = 0.035[3]. The FWHM also shows pronounced peaks at each of the three spin-phonon crossings below $\approx$40 meV.

We note that there is a high degree of consistency between the results of this analysis and that performed using an energy-independent background subtraction, as presented in Figs. 5 and 6 of the main manuscript.

III. COMPARISION OF $\chi''(\mathbf{Q},\hbar\omega)$ AT 2DMZCS WITHOUT A SPIN WAVE CORRECTION

In Section III c) of the main paper we compared $\chi''(\mathbf{Q},\hbar\omega)$ and the $|\mathbf{Q}|^2$-normalized $\chi''(\mathbf{Q},\hbar\omega)$ at the

2DMZCs measured, and the results of this analysis are presented in Fig. 7. This analysis involved the subtraction of an estimate for the spin wave contribution to $\chi''(\mathbf{Q}, \hbar\omega)$, derived from fitting the low energy (< 10 meV) spectrum to a phenomenological $\hbar\omega^{-1}$ form. Here we show the results of the $|\mathbf{Q}|^2$-normalized $\chi''(\mathbf{Q}, \hbar\omega)$ comparison at the 2DMZCs, but without performing the phenomenological correction for spin wave scattering. This is shown in Fig. S6, which should be compared with Fig. 7 b) of the main manuscript. Fig. S6 largely resembles Fig. 7 b), except for the much enhanced low energy spectral weight associated with the $(\text{-}\frac{1}{2}, -\frac{1}{2})$ 2DMZC. This is not surprising as the magnetic scattering, which doesn't scale in intensity as $|\mathbf{Q}|^2$, is strongest at the smallest $|\mathbf{Q}|$ 2DMZC. The same large enhancement of the $|\mathbf{Q}|^2$-normalized $\chi''(\mathbf{Q}, \hbar\omega)$, observed between 15 meV and 20 meV in Fig. 7 b), is observed in Fig. S6. This conclusion is therefore not influenced by the details of how the spectral weight from the low energy spin excitations are accounted for.

[1] G. Shirane, S. M. Shapiro, and J. M. Tranquada. *"Neutron Scattering with a Triple-Axis Spectrometer"*. Cambridge University Press, 2002.

[2] L. Pintschovius, D. Reznik, F. Weber, P. Bourges, D. Parshall, R. Mittal, S. L. Chaplot, R. Heid, T. Wolf, and D. Lamago. *arXiv:1404.0522*, 2014.

[3] M. Matsuda, M. Fujita, S. Wakimoto, J. A. Fernandez-Baca, J. M. Tranquada, and K. Yamada. *Phys. Rev. Lett.*, 101(19):197001, 2008.

Chapter 5

Neutron Scattering Studies of Spin-Phonon Hybridization and Superconducting Spin-Gaps in the High Temperature Superconductor $La_{2-x}(Sr, Ba)_xCuO_4$

This chapter presents measurements of the doping dependence of the enhancement features reported in the previous chapter, for both LBCO and LSCO. These results demonstrate that the enhancement feature found at 20 meV in the previous chapter pervade the phase diagram and occur at the same energy scale for all dopings. These results also demonstrate that the enhancements always occur at the crossing of the dispersive magnetic excitations with relatively dispersionless optic phonons common to all of these materials.

It is found that the enhancement features always occupy the same wave-vectors as the magnetic excitations, with the observed broadening of magnetic components being matched by an associated systematic broadening of the enhancement features. The temperature dependence is also explored across the phase diagram, and appears to occupy a consistent energy scale across the phase diagram. Further study is, however, needed to determine if the cross-over transition temperature is identical for all samples measured.

We also present analysis to present data from all samples on the same intensity scale. This demonstrates that the scattered intensity is roughly doping independent. It is therefore concluded that these enhancements are insensitive to doping, which more strongly suggests hybridization over pure magnetism as the origin of these features. However, this result does not conclusively rule out that hybridization may play a role in superconductivity. Since the magnetic spectral weight is known to deplete with doping, this implies that hybridization occupies an ever growing fraction of the total spectral weight. Therefore, hybridization must occupy a greater spectral weight, and consequently play a larger role in the dynamics at superconducting dopings than at non-superconducting dopings. However, further study remains necessary to determine the nature of the relationship between these phenomena.

Of additional interest, we also present observations of the sub-20 meV scattering in these materials. In particular, we report on the observation of a superconducting spin gap in both LSCO, as had been previously identified, and the new observation of a superconducting spin gap in LBCO. Such an observation settles long standing questions as to why such a gap was absent from LBCO. Our data further indicates that the onset of this gap is qualitatively the same in both LBCO and LSCO, as would be expected.

This work will be submitted to Physical Review B for publication in the next few days from the drafting of this thesis. The work is a collaboration of the following members. J. P. Carlo participated in the SEQUOIA measurements of the x = 0.095 (not presented) and 0.05 LBCO samples. J. Gaudet participated in the ARCS LSCO measurements. G. Van Gastel participated in the x = 0.035 SEQUOIA measurements (not presented). A. T. Savici assisted with data reduction. G. E. Granroth, A. I. Koleshnikov, D. Abernathy were instrument scientists for the SEQUOIA and ARCS measurements. L. Clark collaborated in determining the absolute normalization of the samples. Y. J. Kim, D. Ellis, Y. Zhao, H. Zhang, A. B. Kallin, E. Mazurek and H. A. Dabkowska grew the samples. B. D. Gaulin supervised the experiments, analysis and publication preparations. My contribution was to take a lead role in performing all the experiments, all the analysis and the publication preparations.

Neutron Scattering Studies of Spin-Phonon Hybridization and Superconducting Spin-Gaps in the High Temperature Superconductor $La_{2-x}(Sr,Ba)_xCuO_4$

J.J. Wagman,[1] J. P. Carlo,[1,2] J. Gaudet,[1] G. Van Gastel,[1] D. L. Abernathy,[3] M. B. Stone,[3] G.E. Granroth,[4] A. I. Koleshnikov,[5] A. T. Savici,[4] Y. J. Kim,[6] H. Zhang,[6] D. Ellis,[6] Y. Zhao,[7,8] L. Clark,[1] A.B. Kallin,[1] E. Mazurek,[1] H.A. Dabkowska,[9] and B.D. Gaulin[1,9,10]

[1]*Department of Physics and Astronomy, McMaster University, Hamilton, Ontario, Canada L8S 4M1*
[2]*Canadian Neutron Beam Centre, NRC, Chalk River Laboratories, Chalk River, Ontario, Canada K0J 1J0*
[3]*Quantum Condensed Matter Division, Oak Ridge National Laboratory, Oak Ridge, Tennessee 37831, USA*
[4]*Neutron Data Analysis and Visualization Division, Oak Ridge National Laboratory, Oak Ridge, Tennessee 37831, USA*
[5]*Chemical and Engineering Materials Division, Oak Ridge National Laboratory, Oak Ridge, Tennessee 37831, USA*
[6]*Department of Physics, University of Toronto, Toronto, Ontario, Canada M5S 1A7*
[7]*National Institute of Standards and Technology, Gaithersburg, Maryland 20899-6102, USA*
[8]*Department of Materials Sciences and Engineering, University of Maryland, College Park, Maryland 20742, USA*
[9]*Brockhouse Institute for Materials Research, McMaster University, Hamilton, Ontario, Canada L8S 4M1*
[10]*Canadian Institute for Advanced Research, 180 Dundas Street West, Toronto, Ontario, Canada M5G 1Z8*

We present time-of-flight neutron-scattering measurements on single crystals of $La_{2-x}Ba_xCuO_4$ (LBCO) with 0 $\leq$x$\leq$ 0.095 and $La_{2-x}Sr_xCuO_4$ (LSCO) with $x = 0.08$ and 0.11. This range of dopings spans much of the phase diagram relevant to high temperature cuprate superconductivity, ranging from insulating, three dimensional commensurate long range antiferromagnetic order for $x \leq 0.02$ to two dimensional (2D) incommensurate antiferromagnetism co-existing with superconductivity for $x \geq 0.05$. Previous work on lightly doped LBCO with $x = 0.035$ showed a clear resonant enhancement of the inelastic scattering coincident with the low energy crossings of the highly dispersive spin excitations and quasi-2D optic phonons. The present work extends these measurements across the phase diagram and shows this enhancement to be a common feature to this family of layered quantum magnets. Furthermore we show that the low temperature, low energy magnetic spectral weight is substantially larger for samples with non-superconducting ground states relative to any of the samples with superconducting ground states. Spin gaps, suppression of low energy magnetic spectral weight, are observed in both superconducting LBCO and LSCO samples, consistent with previous observations for superconducting LSCO.

I. INTRODUCTION

There are several important similarities between different families of high temperature superconductors, which can also be common to certain low temperature superconductors.[1] The most striking of these is the proximity of magnetism to superconducting ground states. Interestingly, the contiguous nature of these two ordered states has driven speculation that the two orders compete with each other, and also that the magnetism may be intimately involved in the mechanism for Cooper pair formation in cuprate, iron-based, heavy fermion and organic superconductors[2–8].

The 214 family of cuprate superconductors was the original family of high temperature superconductors to be discovered[9]. Both $La_{2-x}Ba_xCuO_4$ (LBCO) and $La_{2-x}Sr_xCuO_4$ (LSCO) are relatively easy to grow as large and pristine single crystals, although the growth of the $La_{2-x}Sr_xCuO_4$ branch of the family is easier at higher x. As a result, this system has been extensively studied by techniques which require large single crystals, such as inelastic neutron scattering[10]. However, advances in neutron scattering itself, and especially in time-of-flight neutron scattering at spallation neutron sources, have made it timely to revisit the spin and phonon dynamics in these systems, wherein sample rotation methods have allowed for the collection of comprehensive four dimensional data sets, spanning $\mathbf{Q}$ and $\hbar\omega$.

Both $La_{2-x}Ba_xCuO_4$ and $La_{2-x}Sr_xCuO_4$, LBCO and LSCO, respectively, lose their three dimensional commensurate (3D C) antiferromagnetic (AF) order quickly on doping with holes at finite x[11,12]. This occurs at $x = 0.02$ in both LSCO and LBCO. Quasi-two dimensional (2D) incommensurate short range frozen order replaces 3D C antiferromagnetism, with an onset at much lower temperatures, ~ 25 K, for x$\geq$0.02. As a function of increased doping, x, the wave-vector characterizing the 2D IC magnetism increases, consistent with the stripe picture introduced by Tranquada and co-workers[13]. Remarkably, the IC wave-vector rotates by 45 degrees, from so-called diagonal to parallel stripes at a doping level that is co-incident with the onset of a superconducting ground state, $x = 0.05$ in both LBCO and LSCO[14,15].

Independent of whether the AF order is C or IC, the quasi-2D spin excitations are known to be centered on two dimensional magnetic zone centers (2DMZCs), which are wave-vectors of the form $(\frac{1}{2}, \frac{1}{2}, L)$, and equiva-

lent wave-vectors. This notation implies a pseudotetragonal unit cell that is convenient and appropriate given the relatively small orthorhombicity present in these materials[16–19]. The quasi-2D spin excitations are also known to be highly dispersive and to extend to energies $\sim$ 200 - 300 meV depending on the precise level of doping[20–23]. Recent time-of-flight neutron scattering on lightly doped, $x = 0.035$, non-superconducting LBCO has revealed very interesting resonant enhancement of the magnetic spectral weight as a function of energy, that is co-incident with the low energy crossings of the highly dispersive spin excitations with weakly dispersive optic phonons[19]. The optic phonon most strongly associated with this resonant enhancement, at $\sim$ 19 meV, could be identified with a breathing mode of (mostly) the oxygen ions within the CuO_2 planes. This phonon eigenvector is both quasi-2D itself, and is expected to couple strongly to the magnetism, as its displacements flex the main Cu-O-Cu superexchange pathway within the ab plane.

In this paper, we extend these and related time-of-flight neutron scattering measurements to other dopings in the LBCO and LSCO family, including several samples with sufficiently high doping to have superconducting ground states. These results show that the same phenomenology of resonant enhancement of the magnetic spectral weight at the low energy crossings of the very dispersive spin excitations with the weakly dispersive optic phonons, primarily at $\sim$ 15 and 19 meV, is a common feature across the phase diagram studied, from $x = 0$ to $x = 0.11$. We further show a common form for the energy dependence of $\chi''(\mathbf{Q}, \hbar\omega)$ ~~seen~~ across this series at low temperatures, with non-superconducting samples showing greater weight at relatively low energies only, compared with samples with superconducting ground states. We also present evidence for a suppression of the low energy magnetic scattering within the superconducting ground state relative to the same scattering within the higher temperature normal state for both LBCO and LSCO. We interpret these results as the formation of superconducting spin gaps, consistent with previous reports for LSCO.

II. EXPERIMENTAL DETAILS

High-quality single crystals of $La_{2-x}(Sr, Ba)_xCuO_4$ were grown by floating zone image furnace techniques using a four-mirror optical furnace. The growths followed the protocols already reported for the non-superconducting samples[24–26].

LBCO samples at low doping, $x \leq 0.05$, such that they possess non-superconducting ground states, display orthorhombic crystal structures with space group $Bmab$[27,28] at all temperatures measured in these experiments. At higher doping, $x > 0.05$, such that both LBCO and LSCO samples possess superconducting ground states, both orthorhombic and tetragonal crystal structures are observed over the temperature ranges measured[29,30]. Despite this complexity in the structure of the materials studied, the distinction between the a and b lattice parameters within the orthorhombic structures is small, and in light of the relatively low $\mathbf{Q}$ resolution of our measurements, we choose to approximate all of these crystal structures by the high temperature $I4/mmm$ tetragonal structure that is displayed by the parent compound, La_2CuO_4. We will therefore adopt the tetragonal notation for all our samples at all temperatures measured[31,32] in this study. All crystal structures within these families are layered which gives rise to quasi-two dimensional magnetism over most of the phase diagram. Consequently, magnetic zone centers are centered around equivalent $(\frac{1}{2}, \frac{1}{2}, L)$ tetragonal wave-vectors, and appear extended along L. We will refer to these lines in reciprocal space as two dimensional magnetic zone centers (2DMZCs), and much of our focus in this paper will be on these features within reciprocal space.

Neutron scattering measurements were performed using the ARCS and SEQUOIA time-of-flight chopper spectrometers, which are both located at the Spallation Neutron Source at Oak Ridge National Laboratory[33,34]. Both are direct geometry chopper instruments and use the same ambient temperature moderator for their incident neutrons[35]. The single crystal samples were mounted in closed cycle refrigerators allowing measurements to probe the approximate temperature range from 5 to 300 K with a temperature stability of $\sim$ 0.1 K. All measurements were performed with single crystal samples aligned such that their *HHL* scattering plane was horizontal. We employed $E_i = 60$ meV incident energy neutrons for all measurements shown and employed single crystal sample rotation about a vertical axis. By coupling this single crystal sample rotation experimental protocol with the large, two dimensional detector arrays of ARCS and SEQUOIA, we obtained comprehensive four-dimensional master data sets in each experiment (3 $\mathbf{Q}$ and 1 energy dimensions), which we can project into different scattering planes by appropriate integrations of the data.

SEQUOIA was used to measure the $x = 0$ and 0.05 LBCO samples. In these measurements, we employed SEQUOIA's 700 meV high flux chopper to select the incident neutron energy, 60 meV, resulting in an energy resolution at the elastic position of $\sim$ 1 meV. Measurements swept out 141 degrees of single crystal sample rotation, collected in 1 degree steps. Measurements at ARCS were performed on the LBCO $x = 0.035$ and 0.095 and both LSCO samples. Here we employed ARCS' 100 meV chopper[36] to select $E_i = 60$ meV, and again the resulting energy resolution was $\sim$ 1 meV at the elastic position. These measurements swept out 140 degrees of single crystal sample rotation in one degree steps. All

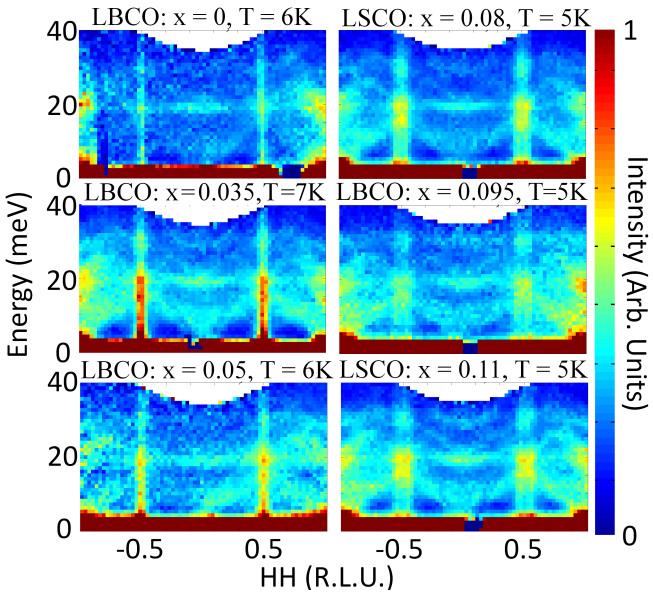

FIG. 1. Energy vs. HH maps for all samples measured, as labeled. The data shown employs the subtraction of an empty can data set[19,39], integration from -0.1 to 0.1 in $< H\bar{H} >$ and -4 to 4 in $< L >$. The vertical rod shaped features, emanating from $(\frac{1}{2},\frac{1}{2})$ positions are the dispersive magnetic excitations. All data have been normalized to be on the same absolute intensity scale as described in the text.

data reduction and analysis for this work were carried out using Mantid[37] and Horace[38], as appropriate.

III. CONTOUR MAPS OF THE SCATTERED NEUTRON INTENSITY

Our time-of-flight neutron data sets span all four dimensions of energy-reciprocal space. As a result, in order to view projections of the scattering in different scattering planes, we must integrate about out-of-plane directions, as appropriate. Scattering planes, or so-called slices, are obtained by integrating the master data set about two out-of-plane directions. Constant-energy or constant-**Q** cuts are obtained by integration of the master data set about three directions[19].

We first present energy vs. HH maps of the scattering for all the single crystals measured at base temperature - between 5 and 7 K. These are obtained by integrating from -0.1 to 0.1 in $H\bar{H}$ and from -4 to 4 in L, and are presented in Fig. 1 for all of our LBCO and LSCO samples, as labeled. We have also normalized each data set to the same absolute, but otherwise arbitrary, intensity scale by using a combination of normalization to incoherent elastic scattering and/or low energy acoustic phonon scattering at 6 meV, near the (0 0 16) Bragg peak[40].

From Fig. 1 we see several common features for all the samples. The most salient common feature is the highly dispersive rod-shaped inelastic scattering that emanates from both of $\mathbf{Q} = (\pm\frac{1}{2},\pm\frac{1}{2},L)$. These rods of inelastic scattering are the highly dispersive spin excitations. One notes a small drop off in this magnetic inelastic intensity with increased doping, although the LBCO $x = 0$ magnetic scattering appears weak due the effects of experimental resolution and signal integration. Nonetheless this is a relatively weak effect and the overall magnetic spectral weight at energies less than $\sim$ 40 meV is not significantly diminished for doping levels out to $x \sim 0.11$. In addition, an increase in the breadth of the magnetic scattering along **Q** is observed, which is consistent with a linear doping dependence of the incommensurate splitting of the magnetic excitations. Such a doping dependence is known to describe the incommensuration of the 2DMZCs[41]. It should be noted that the inelastic magnetic scattering is understood to exhibit an hour-glass shaped dispersion[42,43]. However, our relatively low **Q** resolution scattering is not sensitive to such hour-glass features and the magnetic scattering appears instead as dispersive rods emanating from the 2DMZCs. The incommensurate nature of the inelastic scattering is pronounced and obvious in Fig. 1 for all of the samples with superconducting ground states, which are those with $x > 0.05$. Several clear phonon branches can also be seen within this field of view. These are the quasi-2D phonons common to all of these materials, as previously discussed[19]. As we are employing a rather large integration in L ($\pm$ 4), we expect that three dimensional features will be averaged out by such an integration, while 2D features, dispersionless along L, will present more clearly in such a plot.

Common to all six maps in Fig. 1 is the strong enhancement of the inelastic scattering seen at the crossings of the dispersive spin excitations with the relatively dispersionless optic phonons. This enhancement has been previously discussed for the LBCO $x = 0.035$ sample[19]. Here we see a remarkably consistent phenomenology as a function of doping, for systems with both superconducting and non-superconducting ground states, and for both LBCO and LSCO. The enhanced inelastic scattering increases in breadth along **Q** consistent with an increased incommensuration of the magnetic inelastic scattering emanating from 2DMZCs as a function of doping, as is expected.

We now turn to constant energy slices of the HK plane in Fig. 2, again derived from our master 4 dimensional data set. To obtain this projection, we again integrate from -4 to 4 in L but now integrate by $\pm$ 1 meV in energy. We have done this for all six data sets shown at two energies - 7 meV, an energy at which the scattering at the lowest $|\mathbf{Q}|$ 2DMZCs is almost entirely comprised of magnetic scattering, and 19 meV, the energy for which the optic phonons in the 214 cuprates are quasi-2D in nature and where the enhanced scattered intensity is maximal. Here, we do not normalize each data set to a single abso-

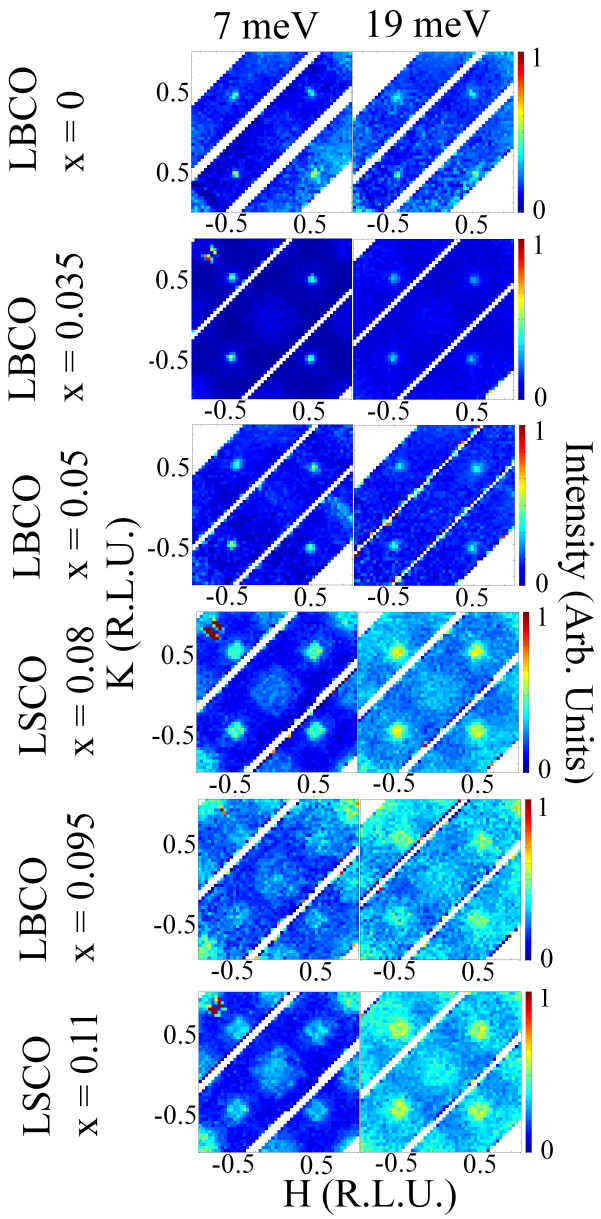

FIG. 2. Maps of the scattering in the HK plane for all samples measured, as labeled. The data shown employs integration from -4 to 4 in $< L >$ and $\pm$ 1 meV in energy, as labeled. Data have been normalized separately, as described in the text.

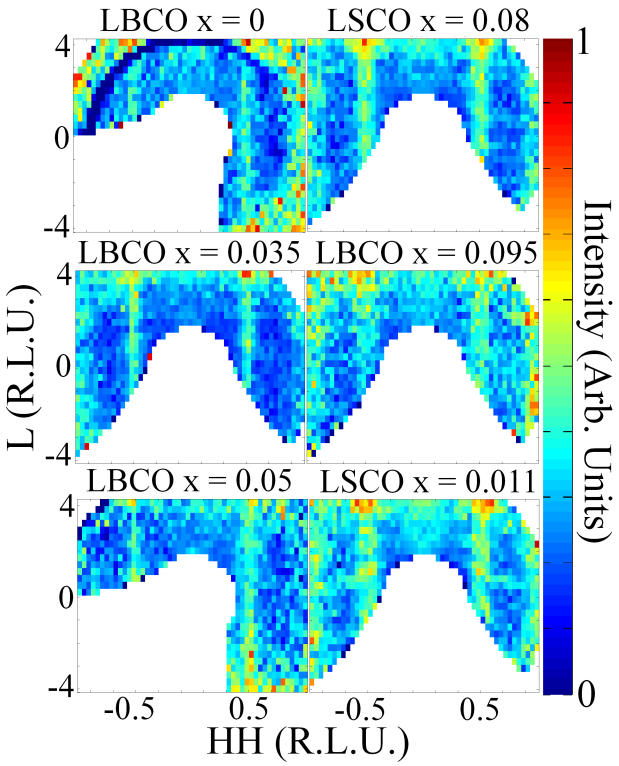

FIG. 3. Maps of the scattering in the HHL for all samples measured, as labeled. The data shown employs integration from -0.1 to 0.1 in $< H\bar{H} >$ and $\pm$ 1 meV about 19 meV. Data have been normalized to the same absolute arbitrary scale.

lute arbitrary energy scale. Instead, we normalize each data set such that the intensity scales at 7 meV appear qualitatively similar, and we then employ the same normalization for the corresponding 19 meV data sets.

Consider first the left column of Fig. 2. This shows the 7 meV data for all six samples measured. At this energy, there are no crossings of phonons with the spin excitations at the 2DMZCs. At the lowest $|\mathbf{Q}|$ 2DMZC we expect minimal contributions from phonon scattering such that the scattered intensity is magnetic in origin. The extent of the scattering within the HK plane increases with doping, x, although it is most noticeable for $x > 0.05$. We also note that the ratio of the magnetic scattering around the 2DMZC to the nearby background scattering, which is comprised of phonon scattering, decreases as a function of x, albeit only slowly. Some decrease in the magnetic scattering with increased x is expected, as magnetic moments are being removed from the samples. Such an effect should appear at least linearly with x[17,44,45]. Nonetheless, this data, and those shown in Fig. 1, make it clear that significant ~~and largely undiminished~~ dynamic magnetic spectral weight is present well into the $La_{2-x}(Sr,Ba)_xCuO_4$ phase diagram, and clearly coexists with superconductivity.

Turning to the HK slices at 19 meV, shown in the right column of Fig. 2, we see similar trends to those seen at 7 meV. We find that the extent of the scattering within the HK plane increases with doping in much the same way as is observed at 7 meV, and the relative strength of the scattering at 19 meV compared with 7 meV appears to increase with x.

Figure 3 focuses on this 19 meV scattering by projecting our 4 dimensional master data set into the HHL

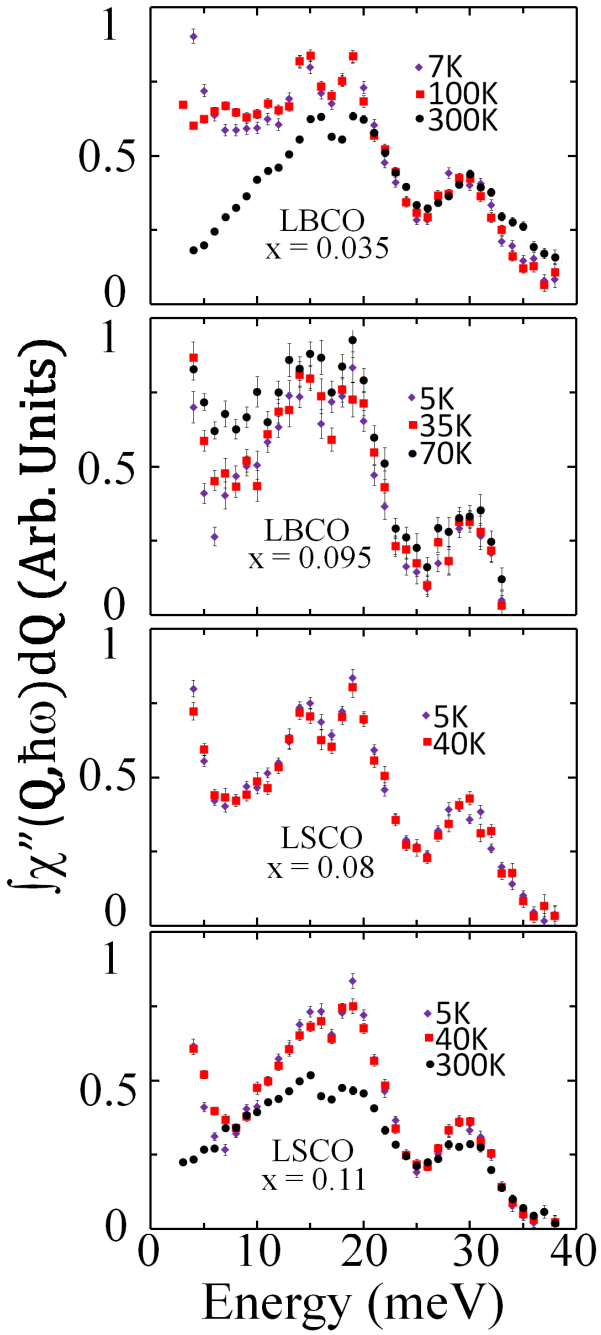

FIG. 4. Constant-energy cuts along the $(-\frac{1}{2},-\frac{1}{2})$ 2DZMC plotted at all measured temperatures for all samples. All data shown were integrated from -0.5 to 0.5 in L, -0.1 to 0.1 in $H\bar{H}$ and -0.6 to -0.4 in HH. The data has been normalized to the same absolute intensity scale, corrected for the Bose factor and employs a subtraction of a **Q** and energy independent background, as described in the text. Error bars represent one standard deviation.

scattering plane. In this figure, we again normalize using an absolute arbitrary intensity scale. We clearly see isotropic rods of scattering that extend along L for the 2DMZCs of the form $(\frac{1}{2},\frac{1}{2},L)$. Such rods of scattering are indicative of the 2D nature of the enhancements seen in Fig. 1. We clearly identify the increasing extent of the rods of scattering in the HH direction with x, and see that this occurs along the full rod of scattering along L.

IV. ANALYSIS AND DISCUSSION

Taken together, Figs. 1-3 show consistent phenomenology across the underdoped region of the 214 cuprate phase diagram, out to almost $x = \frac{1}{8}$. We now focus on a quantitative analysis of the energy dependence of the spectral weight emanating from the 2DMZCs and the resonant enhancement of this spectral weight coincident with crossings of the spin excitations and low-lying optic phonons, as previously reported for LBCO with x = 0.035[19]. We convert our measured S(**Q**,$\hbar\omega$) to the imaginary part of the susceptibility, or $\chi''(\mathbf{Q},\hbar\omega)$ using similar protocols to those used for the LBCO x = 0.035 analysis[19]. The relationship between S(**Q**,$\hbar\omega$) and $\chi''(\mathbf{Q},\hbar\omega)$ is given by:

$$S(\mathbf{Q},\omega,T) = [n(\hbar\omega)+1)] \times \chi''(\mathbf{Q},\omega,T) \qquad (1)$$

where

$$[n(\hbar\omega)+1)] = \frac{1}{1-e^{-\frac{\hbar\omega}{k_B T}}} \qquad (2)$$

is commonly referred to as the Bose factor[46]. To compare the dynamic susceptibility appropriately, one must remove the background contributions to the scattered intensity. We employ the same form of the background subtraction as was previously used for LBCO, x=0.035[19]. For each sample, we first employ an integration from -4 to 4 in L and -0.1 to 0.1 in $\bar{H}H$. From there, we further integrate in HH from $\pm$0.2 to $\pm$0.4 and $\pm$0.6 to $\pm$0.8 in HH to give us a measure of the background away from the 2DZMCs but bounded by the nearby acoustic phonon, as can be seen in Fig. 1 for all of our data sets. Having accounted for the experimental background, we remove the Bose factor from our data and normalize our data sets to an absolute scale. We then quantitatively compare the energy dependence of the **Q**-integrated (around the 2DMZC) $\chi''(\mathbf{Q},\omega,T)$ as a function of doping, x in Figs. 4 and 5.

We focus on the lowest $|\mathbf{Q}|$ 2DZMC $\mathbf{Q} = (-\frac{1}{2},-\frac{1}{2})$ position, and employ a narrow integration of -0.5 to 0.5 in L to minimize contributions from one phonon creation processes. We also compare data sets taken on ARCS

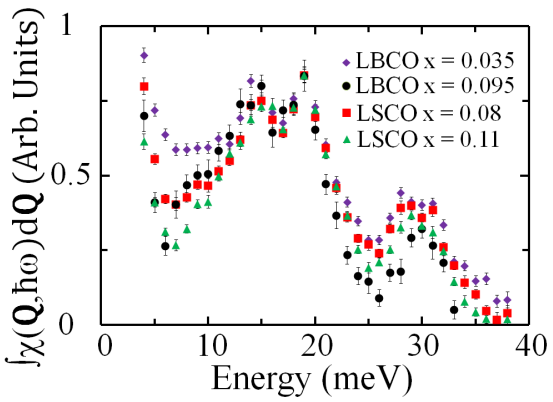

FIG. 5. Constant-energy cuts along the $(-\frac{1}{2},-\frac{1}{2})$ direction, as shown in Fig. 4, for the lowest temperature data sets collected on each sample. Here, all data shown have normalized to the same arbitrary intensity scale. Error bars represent one standard deviation.

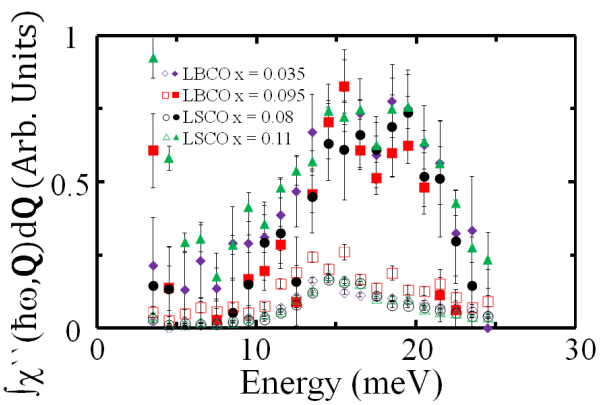

FIG. 6. $|Q|^2$ normalized integrated $\chi''(\hbar\omega,\mathbf{Q})$ for all ARCS data sets, as described in the text. A narrow L integration of ± 0.5 R.L.U. about the $(-\frac{1}{2},-\frac{1}{2},0)$ and $(-\frac{5}{2},-\frac{5}{2},0)$ 2DMZCs is employed for all samples measured. Closed symbol data sets correspond to data from $\mathbf{Q}=(-\frac{1}{2},-\frac{1}{2})$, while open symbol data sets correspond to data from $\mathbf{Q}=(-\frac{5}{2},-\frac{5}{2})$

only, as there are four such data sets that span the key range of the 214 cuprate phase diagram, and these allow us the most "like-with-like" comparison of our data sets.

Figure 4 shows the integrated dynamic susceptibility, $\chi''(\mathbf{Q},\hbar\omega)$, for all four samples measured on ARCS and at all temperatures investigated. These are all of our samples with superconducting ground states and one sample with a non-superconducting ground state (LBCO $x = 0.035$). All of these data sets show very similar parametric behavior above ~ 10 meV. We find that the effects of temperature do not significantly affect the scattering above 10 meV until the temperature reaches on the order of 300 K. At 300 K $\chi''(\mathbf{Q},\hbar\omega)$ is noticeably reduced especially below ~ 15 meV. The bottom three panels of Fig. 4 all show the integrated dynamic susceptibility $\chi''(\mathbf{Q},\hbar\omega)$ for underdoped LBCO and LSCO samples with superconducting ground states. In addition these plots all show data sets at T = 5 K, which is well below each sample's respective superconducting T_C, and at T = 35 K or 40 K, which are around 5 K above each sample's respective T_C.

Figure 5 shows the integrated dynamic susceptibility, $\chi''(\mathbf{Q},\hbar\omega)$ at low temperatures for all four samples shown in Fig. 4, but now overlaid such that the similarities and differences between low temperature $\chi''(\mathbf{Q},\hbar\omega)$ as a function of doping, x, can be explicitly seen. Normalizing the $\chi''(\mathbf{Q},\hbar\omega)$ to agree at all dopings in the resonant enhancement energy regime, 15 - 20 meV, we see that the integrated dynamic susceptibility, $\chi''(\mathbf{Q},\hbar\omega)$ at low temperatures agree in detail remarkably well at all energies from ~ 10 meV to 25 meV, for the LBCO and LSCO samples with superconducting ground states, $x = 0.08$, 0.095 and 0.11. The LBCO sample with a non-superconducting ground state, $x = 0.035$, agrees with the other samples very well above ~ 12 meV, but shows enhanced magnetic spectral weight at energies below ~ 12 meV. The overall phenomenology is clear; the integrated dynamic susceptibility, $\chi''(\mathbf{Q},\hbar\omega)$ at low temperatures is very similar for underdoped LBCO and LSCO at all doping levels measured, with the proviso that there is enhanced low energy (< 12 meV) magnetic spectral weight for the non-superconducting $x = 0.035$ sample.

The quantitative agreement between the integrated dynamic susceptibility, $\chi''(\mathbf{Q},\hbar\omega)$ at low temperatures and below ~ 35 meV across over such a large range of doping in both LBCO and LSCO is remarkable. Combined with the earlier observation from Figs. 1-3 that the breadth in Q of the enhancements track with the incommensuration about the 2DMZC, while staying centred on the energies of the low lying optic phonons, we are led to an interpretation of the enhancement which depends on both the spin and phonon degrees of freedom. Such an effect would likely involve a hybridization of quasi-2D spin degrees of freedom with optic phonons, as opposed to a solely magnetic origin.

As was done previously for LBCO x = 0.035[19], we can compare the strength and form of $\chi''(\mathbf{Q},\hbar\omega)$ as a function of $\mathbf{Q}$ at 2DMZCs for which the nuclear structure factor is identical (within the $I4/mmm$ space group). The structure factors are identical at wave vectors of the form $(\frac{H}{2},\frac{H}{2},0)$ and in Fig. 6, we compare $\chi''(\mathbf{Q},\hbar\omega)$ integrated around the $(-\frac{1}{2},-\frac{1}{2},0)$ and $(-\frac{5}{2},-\frac{5}{2},0)$ wave vectors. We observe the same large enhancements to $\chi''(\mathbf{Q},\hbar\omega)$ near 15 meV and 19 meV around $(-\frac{1}{2},-\frac{1}{2},0)$ as were seen in Figs. 4 and 5. Were this enhancement due solely to phonons, it would scale as $|\mathbf{Q}|^2$. We have scaled the measured $\chi''(\mathbf{Q},\hbar\omega)$ by $|\mathbf{Q}|^2$ in Fig. 6, and clearly the $|\mathbf{Q}|2$ scaled $\chi''(\mathbf{Q},\hbar\omega)$ is much stronger near $(-\frac{1}{2},-\frac{1}{2},0)$ than near $(-\frac{5}{2},-\frac{5}{2},0)$. This eliminates the possibility that the enhancement is due to phonons alone, or due to a simple superposition of phonons and

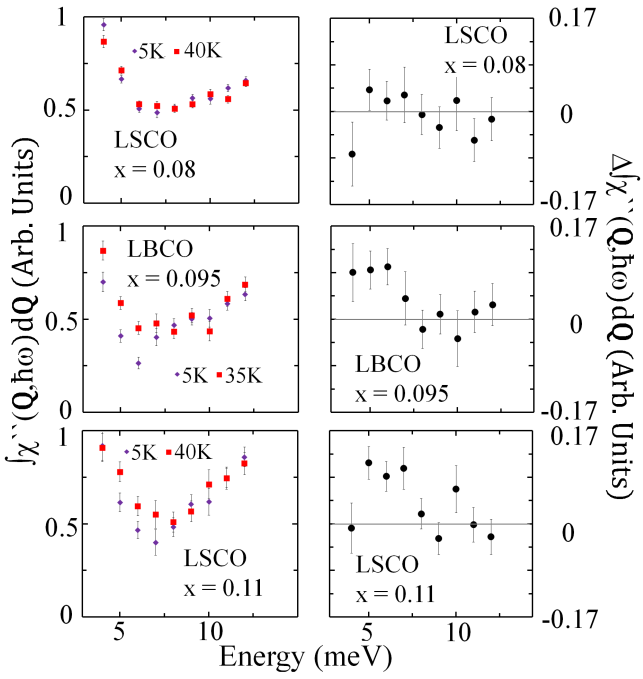

FIG. 7. Left Column: Integrated $\chi''(\mathbf{Q},\hbar\omega)$ for the three samples with superconducting ground states. These data have been integrated from -4 to 4 in L, from -0.1 to 0.1 in $H\bar{H}$ and from -0.6 to -0.4 in HH. Only a $\mathbf{Q}$ and energy independent background has been subtracted from the data set. Right Column: Difference plots between the high temperature (35 K or 40 K) and the low temperature (5 K) data sets shown in the left column of this figure. Data sets from the same sample (in the right or left column) employ the same arbitrary intensity scale. Error bars represent one standard deviation.

spin excitations whose spectral weight monotonically decreases with energy. Fig. 6 shows that such a conclusion follows for all concentrations of LBCO and LSCO studied.

Finally, we address the issue of whether or not a spin gap, a suppression in the magnetic spectral weight at low energies, occurs in underdoped LBCO and LSCO on reducing temperature and entering the superconducting state. As can be seen in Fig. 4, the presence of a spin gap will be a subtle effect. As the magnetic scattering is quasi-2D, we perform a similar analysis to that which produced Figures 4 and 5, but now employing a larger -4 to 4 integration in L, to better capture the two dimensional magnetic scattering. The resulting integrated dynamic susceptibility, $\chi''(\mathbf{Q},\hbar\omega)$ is shown in Fig. 6 for our three samples with superconducting ground states, for energies below $\sim$ 10 meV, and for temperatures just above (35 K or 40 K) and well below (5 K), each sample's superconducting T_C. Data in the left hand column of Fig. 6 shows the integrated dynamic susceptibility, $\chi''(\mathbf{Q},\hbar\omega)$ for the three crystals, while that in the right hand column of Fig. 6 shows the corresponding difference in integrated dynamic susceptibility between the superconducting (T = 5 K) and normal states (T = 35 K or 40 K).

In this context, a spin gap is identified as excess integrated dynamic susceptibility, $\chi''(\mathbf{Q},\hbar\omega)$, occurring at low energies in the higher temperature normal state, as compared to the lower temperature superconducting state. While the effect of the spin gap is subtle, our data is consistent with a spin gap of $\sim$ 8 meV for x = 0.11, falling to $\sim$ 2 meV or lower for $x = 0.08$. Presumably, the spin gap energy should fall to zero at the low x onset of superconductivity in these families, which is $x = 0.05$. We note that the superconducting spin gap we observe in LBCO $x = 0.095$ is similar but $\sim$ 1 meV lower than that displayed in LSCO $x = 0.11$. Our results show consistency between the LBCO and LSCO families, as expected as their physical properties are so similar. The observation of a spin gap in LBCO resolves a long-standing puzzle that LBCO had not previously shown a spin gap, while LSCO had[47].

For the LSCO $x = 0.08$ sample, we see greater scattered intensities below 8 meV within the superconducting ground state, while LSCO $x = 0.11$ presents greater scattered intensities in the normal state below 8 meV. We interpret this data as consistent with previous reports of superconducting spin gaps in these materials. For LSCO $x = 0.11$, the spin gap energy scale appears to be consistent with previous reports, with a gap energy around 8 meV[48,49]. While there does not appear to be a gap in the presented LSCO $x = 0.08$ data, we believe this to be a result of the gap energy being below 2 meV. Given the energy resolution of our experiment, we believe that the enhanced low temperature scattering is instead due to quasi-elastic scattering from the ordered magnetic ground state.

V. CONCLUSIONS

We have carried out comprehensive inelastic neutron scattering measurements using single crystal sample rotation and time of flight techniques on samples of the underdoped 214 cuprate superconductors, LBCO and LSCO, for doping levels between $x = 0$ and $x = 0.11$. All of these samples show a resonant enhancement of the inelastic spectral weight at 2DMZCs and at energies which correspond to crossings of the highly dispersive spin excitations with weakly dispersive optic phonons. These results are quantitatively similar to those previously reported for non-superconducting LBCO with $x = 0.035$, but which are now extended well into the superconducting part of the LBCO and LSCO phase diagrams. This enhancement is therefore a generic property of these families of quasi two dimensional, single layer copper oxides.

While it is possible that the enhanced spectral weight

as a function of energy at 2DMZCs is a purely magnetic effect, as was postulated earlier for LSCO with $x = 0.085$ and 0.016[50,51], its occurence at the confluence in $\mathbf{Q}$ and energy of dispersive spin excitations with optic phonons, and its doping independence, at least for $x < 0.12$, makes a hybridized spin-phonon resonance much more plausible. Furthermore, the eigenvector of the ~ 19 meV optic phonon for which this enhancement is largest is known to be a quasi-two dimensional oxygen breathing mode, with ionic displacements primarily within the CuO_2 planes, as reported previously for LBCO with $x = 0.035$. Such an eigenvector flexes the Cu-O bonds most responsible for strong antiferromagnetic superexchange, and such a phonon would be expected to couple strongly to magnetism in LBCO and LSCO.

If the requirements for this resonant enhancement are indeed dispersive spin excitations and quasi-two dimensional optic phonons capable of coupling strongly to the spin degrees of freedom, then we do expect this same phenomenology to persist across the copper oxide phase diagram, to samples with superconducting ground states, as we are reporting. This opens up the very real possibility that such an enhancement should exist in other families of high T_C oxides, and the more speculative possibility that such a hybridized spin-phonon excitation plays a role in superconducting pairing.

We further show that the quantitative form of the low temperature, integrated dynamic susceptibility, $\chi''(\mathbf{Q}, \hbar\omega)$ at the 2DMZC is very similar as a function of doping, at least out to $x = 0.11$ in both LBCO and LSCO. The main changes that occur on doping is the suppression of magnetic spectral weight for energies less than ~ 12 meV at low, non-superconducting dopings compared with higher, superconducting dopings and the development of a superconducting spin gap for $x > 0.05$ for both LBCO and LSCO.

ACKNOWLEDGMENTS

We would like to acknowledge useful conversations had with N. Christensen, E. Taylor, J. P. Carbotte, T. Timusk, J. Tranquada, I. Zaliznyak and D. Fobes. We would also like to acknowledge T. E. Sherline and L. DeBeer Schmidt for technical assistance with the measurements on SEQUOIA, J. Niedziela and D. Maharaj for technical assistance with the ARCS measurements and E. McNeice for assistance with sample growth. Research using ORNL's Spallation Neutron Source was sponsored by the Scientific User Facilities Division, Office of Basic Energy Sciences, U.S. Department of Energy. Work at McMaster was funded by NSERC of Canada.

[1] L. Taillefer. *Annual Review of Condensed Matter Physics*, 1:51–70, 2010.
[2] P. W. Anderson. *Science*, 235:1196, 1987.
[3] V. J. Emery and S. A. Kivelson. *Nature*, 374:434, 1993.
[4] C. Varma. *Nature*, 468:184, 2010.
[5] N. D. Mathur, F. M. Grosche, S. R. Julian, I. R. Walker, D. M. Freye, Haselwimmer R. K. W., and G. G. Lonzarich. *Nature*, 394:39, 1998.
[6] S. Sachdev, M. A. Metlitski, and M. Punk. *Journal of Physics Condensed Matter*, 24:294205, 2012.
[7] A. T. Savici, A. Fukaya, I. M. Gat-Malureanu, T. Ito, P. L. Russo, Y. J. Uemura, C. R. Wiebe, P. P. Kyriakou, G. J. MacDougall, M. T. Rovers, G. M. Luke, K. M. Kojima, M. Goto, S. Uchida, R. Kadono, K. Yamada, S. Tajima, T. Masui, H. Eisaki, N. Kaneko, M. Greven, and G. D. Gu. *Phys. Rev. Lett.*, 95:157001, Oct 2005.
[8] A. T. Savici, Y. Fudamoto, I. M. Gat, T. Ito, M. I. Larkin, Y. J. Uemura, G. M. Luke, K. M. Kojima, Y. S. Lee, M. A. Kastner, R. J. Birgeneau, and K. Yamada. *Phys. Rev. B*, 66(1):014524, 2002.
[9] J.G. Bednorz and K.A. Muller. *Z. Phys. B.*, 64(189), 1986.
[10] S. Wakimoto, H. Zhang, K. Yamada, I. Swainson, Hyunkyung Kim, and R. J. Birgeneau. *Phys. Rev. Lett.*, 92(21):217004, 2004.
[11] J. J. Wagman, G. Van Gastel, K. A. Ross, Z. Yamani, Y. Zhao, Y. Qiu, J. R. D. Copley, A. B. Kallin, E. Mazurek, J. P. Carlo, H. A. Dabkowska, and B. D. Gaulin. *Phys. Rev. B*, 88:014412, 2013.
[12] B. Keimer, N. Belk, R. J. Birgeneau, A. Cassanho, C. Y. Chen, M. Greven, M. A. Kastner, A. Aharony, Y. Endoh, R. W. Erwin, and G. Shirane. *Phys. Rev. B*, 46(21):14034–14053, 1992.
[13] J. M. Tranquada, B. J. Sternlieb, J. D Axe, Y. Nakamura, and S. Uchida. *Nature*, 375(6532):561–563, 1995.
[14] S. R. Dunsiger, Y. Zhao, B. D. Gaulin, Y. Qiu, P. Bourges, Y. Sidis, J. R. D. Copley, A. Kallin, E. M. Mazurek, and H. A. Dabkowska. *Phys. Rev. B*, 78(9):092507, 2008.
[15] J. M. Tranquada. *AIP Conf. Proc.*, 1550:114, 2013.
[16] R. J. Birgeneau, C. Stock, J. M. Tranquada, and K. Yamada. *Journal of the Physical Society of Japan*, 75(11):111003, 2006.
[17] M. Fujita, K. Yamada, H. Hiraka, P. M. Gehring, S. H. Lee, S. Wakimoto, and G. Shirane. *Phys. Rev. B*, 65:064505, Jan 2002.
[18] K. Yamada, C. H. Lee, K. Kurahashi, J. Wada, S. Wakimoto, S. Ueki, H. Kimura, Y. Endoh, S. Hosoya, G. Shirane, R. J. Birgeneau, M. Greven, M. A. Kastner, and Y. J. Kim. *Phys. Rev. B*, 57:6165–6172, 1998.
[19] J. J. Wagman, D. Parshall, M. B. Stone, A. T. Savici, Y. Zhao, H. A. Dabkowska, and B. D. Gaulin. *Phys. Rev. B*, 91:224404, Jun 2015.
[20] M. Fujita, H. Hiraka, M. Matsuda, M. Matsuura, J. M. Tranquada, S. Wakimoto, G. Xu, and K. Yamada. *Journal of the Physical Society of Japan*, 81(1):011007, 2012.
[21] J. M. Tranquada, G. Xu, and I. A. Zaliznyak. *Journal of Magnetism and Magnetic Materials*, 350:148, 2014.
[22] R. Coldea, S. M. Hayden, G. Aeppli, T. G. Perring, C. D. Frost, T. E. Mason, S.-W. Cheong, and Z. Fisk. *Phys.*

Rev. Lett., 86:5377–5380, 2001.

[23] N. S. Headings, S. M. Hayden, R. Coldea, and T. G. Perring. *Phys. Rev. Lett.*, 105:247001, 2010.

[24] M. Fujita, H. Goka, K. Yamada, J. M. Tranquada, and L. P. Regnault. *Phys. Rev. B*, 70(10):104517, 2004.

[25] H. A. Dabkowska and A. B. Dabkowski. *"Crystal Growth of Oxides by Optical Floating Zone Technique. Experimental Approach to Defects Determination"*. Springer Handbook of Crystal Growth, Defects and Characterization. Springer-Verlag, 2010.

[26] D. S. Ellis, Kim. J., J. P. Hill, S. Wakimoto, R. J. Birgeneau, Y. Shvyd'ko, D. Casa, T. Gog, K. Ishii, K. Ikeuchi, A. Paramekanti, and Y.-J. Kim. *PRB*, 81:085124, 2010.

[27] P. Böni, J. D. Axe, G. Shirane, R. J. Birgeneau, D. R. Gabbe, H. P. Jenssen, M. A. Kastner, C. J. Peters, P. J. Picone, and T. R. Thurston. *Phys. Rev. B*, 38(1):185–194, 1988.

[28] M. A. Kastner, R. J. Birgeneau, G. Shirane, and Y. Endoh. *Rev. Mod. Phys.*, 70:897–928, 1998.

[29] B. Keimer, A. Aharony, A. Auerbach, R. J. Birgeneau, A. Cassanho, Y. Endoh, R. W. Erwin, M. A. Kastner, and G. Shirane. *Phys. Rev. B*, 45:7430–7435, 1992.

[30] Y. Zhao, B. D. Gaulin, J. P. Castellan, J. P. C. Ruff, S. R. Dunsiger, G. D. Gu, and H. A. Dabkowska. *Phys. Rev. B*, 76(18):184121, 2007.

[31] S. Katano, J. A. Fernandez-Baca, S. Funahashi, N. Mori, Y. Ueda, and K. Koga. *Physica C*, 214:64 – 72, 1993.

[32] Chul-Ho Lee, Kazuyoshi Yamada, Yasuo Endoh, Gen Shirane, R. J. Birgeneau, M. A. Kastner, M. Greven, and Y-J. Kim. *Journal of the Physical Society of Japan*, 69(4):1170–1176, 2000.

[33] D. L. Abernathy, M. B. Stone, M. J. Loguillo, M. S. Lucas, O. Delaire, X. Tang, J. Y. Y. Lin, and B. Fultz. *Review of Scientific Instruments*, 83, 2012.

[34] G. E. Granroth, A. I. Kolesnikov, T. E. Sherline, J. P. Clancy, K. A. Ross, J. P. C. Ruff, B. D. Gaulin, and S. E. Nagler. *Journal of Physics Conference Series*, 251:12058, 2010.

[35] J.R. Haines, T.J. McManamy, T.A. Gabriel, R.E. Battle, K.K. Chipley, J.A. Crabtree, L.L. Jacobs, D.C. Lousteau, M.J. Rennich, and B.W. Riemer. *Nuclear Instruments and Methods in Physics Research Section A: Accelerators, Spectrometers, Detectors and Associated Equipment*, 764:94, 2014.

[36] M. B. Stone, J. L. Niedziela, D. L. Abernathy, L. DeBeer-Schmitt, G. Ehlers, O. Garlea, G. E. Granroth, M. Graves-Brook, A. I. Kolesnikov, A. Podlesnyak, and B. Winn. *Review of Scientific Instruments*, 85, 2014.

[37] O. Arnold, J.C. Bilheux, J.M. Borreguero, A. Buts, S.I. Campbell, L. Chapon, M. Doucet, N. Draper, R. Ferraz Leal, M.A. Gigg, V.E. Lynch, A. Markvardsen, D.J. Mikkelson, R.L. Mikkelson, R. Miller, K. Palmen, P. Parker, G. Passos, T.G. Perring, P.F. Peterson, S. Ren, M.A. Reuter, A.T. Savici, J.W. Taylor, R.J. Taylor, R. Tolchenov, W. Zhou, and J. Zikovsky. *Nuclear Instruments and Methods in Physics Research Section A: Accelerators, Spectrometers, Detectors and Associated Equipment*, 764:156, 2014.

[38] $http://horace.isis.rl.ac.uk/Main_Page$.

[39] L. Pintschovius, D. Reznik, F. Weber, P. Bourges, D. Parshall, R. Mittal, S. L. Chaplot, R. Heid, T. Wolf, and D. Lamago. *arXiv:1404.0522*, 2014.

[40] G. Xu, Z. Xu, and J. M. Tranquada. *Review of Scientific Instruments*, 84:083906, 2013.

[41] P. A. Lee, N. Nagaosa, and X.-G. Wen. *Review of Modern Physics*, 78:17, 2006.

[42] M. Matsuda, G. E. Granroth, M. Fujita, K. Yamada, and J. M. Tranquada. *Phys. Rev. B*, 87:054508, 2013.

[43] M. Matsuda, M. Fujita, S. Wakimoto, J. A. Fernandez-Baca, J. M. Tranquada, and K. Yamada. *Phys. Rev. Lett.*, 101(19):197001, 2008.

[44] M. Enoki, M. Fujita, T. Nishizaki, S. Iikubo, D. K. Singh, S. Chang, J. M. Tranquada, and K. Yamada. *Phys. Rev. Lett.*, 110:017004, 2013.

[45] S. Wakimoto, R. J. Birgeneau, Y. S. Lee, and G. Shirane. *Phys. Rev. B*, 63:172501, Mar 2001.

[46] G. L. Squires. *"Introduction to the Theory of Thermal Neutron Scattering"*. Dover Publications, 1978.

[47] J. M. Tranquada. *"Neutron Scattering Studies of Antiferromagnetic Correlations in Cuprates" in Handbook of High Temperature Superconductivity, edited by J. R. Schrieffer and J. S. Brooks.* Springer, New York, 2007.

[48] N. B. Christensen, D. F. McMorrow, H. M. Rønnow, B. Lake, S. M. Hayden, G. Aeppli, T. G. Perring, M. Mangkorntong, M. Nohara, and H. Takagi. *Phys. Rev. Lett.*, 93:147002, 2004.

[49] B. Lake, G. Aeppli, T. E. Masone, A. Schroder, D. F. McMorrow, K. Lefmann, M. Isshiki, M. Nohara, H. Takagi, and S. M. Hayden. *Nature*, 400:43, 1999.

[50] B. Vignolle, S.M. Hayden, D.F. McMorrow, H.M. Ronnow, B. Lake, C.D. Frost, and T.G. Perring. *Nature (London)*, pages 163–167, 2007.

[51] O. J. Lipscombe, S. M. Hayden, B. Vignolle, D. F. McMorrow, and T. G. Perring. *Phys. Rev. Lett.*, 99(6):067002, 2007.

Part V

Conclusions

5.1 Two Dimensional Incommensurate and Three Dimensional Commensurate Magnetic Order and Fluctuations in $La_{2-x}Ba_xCuO_4$

The results of this chapter spanned the phase diagram for sub-superconducting dopings of LBCO. This comprehensive study included detailed measurements of the ordered magnetic structures and low-lying ($\leq$ 1 meV) magnetic excitations in LBCO. Below are some final thoughts on a few of the more notable observations from this chapter.

A first interesting result is conclusive evidence of the co-existence of 3D C AF and 2D IC AF order. More importantly, the triple axis measurements presented in Fig. 1 of this chapter evidence that 2D IC AF develops at the expense of 3D C AF. This is seen in the noticeable downturn in the 3D C AF elastic scattered intensity below 25 K for the x = 0.0125 sample. We can securely identify the dimensionality of these orders from the data shown in Fig. 2 of this chapter, which provides clear evidence of rods of scattering developing below 35 K. However, what these results do not inform upon is precisely how these two orders can co-exist within the same crystal. While it is in principle possible from this data to determine the volume fractions of these respective orders using a determination of the magnetic moment of the system combined with absolute normalization of the data to incoherent scattering, such information would not distinguish between the two most plausible scenarios that naturally explain such a co-existence. The first scenario one can imagine is where part of the 3D C AF ordered correlations along the c-axis begin to fluctuate dynamically on a sufficiently long time scale that the fluctuations appear as elastic to the neutron. Alternatively, it could also be the case that there is a physical separation between regions of 2D IC AF order and regions of 3D C AF order in the crystal. A resolution of this outstanding issue would be appropriate for study by NMR and/or μSR. However, in either case, the competitive nature of these orders is clear and their co-existence confirmed by this study.

A second interesting result is the apparently linear doping dependence of the incommensurability of the static 2D IC AF correlations. As discussed, some authors have suggested that the linear doping dependence of these features appear only above some threshold doping. However, these results are more consistent with a linear doping dependence pervading the lowest dopings of the LBCO phase diagram. Such a picture

would then suggest a possible cause for the null observation of 2D IC AF order for the x = 0 parent compound shown in Fig. 2 of this chapter. In this scenario, the 2D IC AF order would become 2D C AF order as $\delta = 0$. It is not hard to imagine that a relatively short-ranged 2D signal might be nearly impossible to resolve superimposed upon a long range 3D C AF signal. This is because the latter long-range order provides a significantly stronger scattering signal than the former short-range order. However, this is only one of a number of possible explanations. Further study would be necessary to resolve this issue conclusively.

These results also indicate the high degree of similarity between the magnetic structures and excitations of LBCO and LSCO. This is an important verification as it implies that discoveries made in one system likely inform upon the physics of the other. Further, were these two systems to appear dissimilar then we would have to conclude that holes alone could not be the sole driving force behind the doping dependent phenomena of these materials. For if the two systems behaved distinctly despite being isostructural and in identical electronic configurations then some other driver would need to be present to explain the discrepancy. Indeed, it is the similarity of these two systems that motivated an expectation that a superconducting spin gap should exist in LBCO given that such a gap existed in LSCO.

Turning to the excitations, there are two main results reported in this work.

The first result is the systematic depletion of the lowest energy dynamic susceptibility as a function of doping. This result appears to be a precursor to the superconducting spin gaps observed at higher dopings. Since these superconducting spin gaps provide a clear correlation between the magnetic excitations and superconductivity, then we can speculate that perhaps the magnetic excitations in 214 Cuprates are generally intimately tied to superconductivity itself. Indeed, magnetic excitations have been long held as a top candidate for the pairing mechanism of high temperature superconductivity. This result provides a further tantalizing suggestion of the close ties between magnetism and superconductivity.

The second result is the apparently universal temperature dependence of the total integrated susceptibility below 1 meV. We find that the excitations present no true transition, but instead show a cross-over effect at a temperature scale on the order of the highest 3D C AF T_N relevant to L(B,S)CO. It would be interesting to see if the precise cross-over temperature presented any doping dependence. It would also be interesting to explore the behavior of superconducting samples in a similar context,

although such a study would be complicated by superconducting spin gap effects and hence may not be possible.

Lastly, this data enabled us to posit a phase diagram based solely upon neutron order parameter measurements. It is fascinating to note that such a novel phase diagram captures much of the complexity of other high temperature superconducting phase diagrams. This brings us again to one of the key themes of this work: magnetism and superconductivity are highly correlated.

5.2 Hybridization of Two Dimensional Spin Excitations and Phonons in $La_{1.965}Ba_{0.035}CuO_4$

This chapter presents the most exhaustive and comprehensive characterization of the large enhancements of the integrated scattered intensity found in 214 cuprates. While it is not until the following chapter that data is presented that conclusively demonstrates that the features reported upon here are universal to 214 cuprates, this study in of itself strongly suggests the likely critical importance that these enhancements occur at the dispersion crossing of highly dispersive quasi-2D magnetic excitations with less dispersive quasi-2D phonons. As such phonons necessarily appear in all 214 materials, and the significant likelihood of similar magnetic excitations manifesting throughout the 214 system, in view of this study it was expected that similar 20 meV features should appear in all samples of LBCO and LSCO measured.

Using modern neutron scattering spectrometers, identifying these excitations can be performed simply, which highlights the significant advances that have occurred in neutron scattering in recent years. As best seen in Fig. 1 of this chapter, robust features appear at all equivalent 2D magnetic zone centers near 20 meV, which corresponds to spin excitations crossing with low lying optic phonon modes.

However, as Fig. 7 of this chapter indicates, the $\mathbf{Q}$ dependence displayed in Fig. 1 can be misleading. A proper characterization finds that the enhancements at the lowest $|\mathbf{Q}|$ 2DMZCs are to be interpreted as arising from something more than a simple confluence of the scattered intensity from phonon scattering with hour-glass magnetic scattering. Such a characterization also suggests that such a simple confluence is likely the underlying driver for the enhancements seen at higher $|\mathbf{Q}|$, whose scattered intensity presents classic-phonon like $|\mathbf{Q}|^2$ dependence.

Like the magnetism reported in the previous chapter, the relevant temperature scale for these features is on the order of the highest 3D C AF T_N relevant to 214 cuprates. Further, like the magnetic and lattice excitations that likely hybridize to create these prominent scattering effects, the 20 meV features present as dynamic rods of scattering extended along L. This indicates that the features themselves are also quasi-2D. Taken together, these data then seem to suggest a hybridization origin over a purely magnetic origin. Such a scenario seems natural given the nature of the phonons involved at the spin-phonon crossings.

However, these results alone do not inform upon the ties of these enhancements to superconductivity. As these results correspond to a non-superconducting sample and appear quite similar to previous reports of such a feature in superconducting samples, a simple direct link to doping dependent high temperature superconductivity seems unlikely at best. However, we cannot ignore the clearly significant spectral weight occupied by these excitations. It is clear that a large fraction of the electrons in these materials must participate in these excitations. Given the necessity of at least some tie between these features with magnetism, be it direct or via hybridization, and a strong suggestion of ties between magnetism and superconductivity brought forward in the previous chapter, it seems likely that some connection between these enhancement features and superconductivity should exist.

5.3 Neutron Scattering Studies of Spin-Phonon Hybridization and Superconducting Spin-Gaps in the High Temperature Superconductor $La_{2-x}(Sr, Ba)_xCuO_4$

This last chapter expands upon the previous chapter to determine the universal presence of enhancement features occurring at the spin-phonon crossings that generally appear in 214 cuprates. Indeed, as the features appear both qualitatively and quantitatively similar across the phase diagram, it seems quite unlikely that a purely magnetic origin can explain these phenomena. It is therefore likely that these features are owing to hybridization.

As a first point, this study notably returns to the theme of the similarities between

LBCO and LSCO by resolving the long-standing problem of the superconducting spin gap of LBCO. Given that high quality LBCO single crystals are difficult to produce and the weak nature of the signals in these systems, it is not surprising that this gap could not be resolved in the absence of powerful neutron sources like those now available. Moreover, as the magnetic excitations in this system are 2D in nature, studies of these gaps are better suited to modern time-of-flight instruments than triple-axis spectrometers, the latter of which being limited to view a single point in E-**Q** space at a time.

However, the main focus of this chapter is hybridization. It should be first pointed out that despite the apparent doping independence of hybridization, there is still a case for ties between hybridization and superconductivity. This is because scattering from other magnetic excitations in the system occupy smaller and smaller fractions of the total spectral weight available. Therefore, hybridization only becomes more significant of an effect with doping. Consequently, one cannot understand the high temperature superconductivity problem without at least some appreciation of the hybridization problem. For example, hybridization is a well known cause of features like charge density order in other systems. As well, it cannot be ignored that 20 meV is a well-suited energy scale for driving Cooper pairing. This latter point may suggest that hybridization could play an indirect role in superconductivity whereby hybridization, which appears doping independent, is capable of cooperating with some other doping dependent interaction.

It would therefore be interesting to pursue further study of hybridization in overdoped LSCO. LSCO is likely preferable as a) samples of overdoped LSCO exist while overdoped LBCO does not, and b) it would be interesting to see if hybridization remains as constant as it does for underdoped LBCO and LSCO. It may well be that hybridization can serve as a litmus for variations in the magnetic character of these materials. As well, from a hybridization picture, we should expect to find evidence of hybridization in other cuprate superconductors as well as other materials with similar structural and magnetic properties, such as nicklates and cobaltates.

5.4 Final Thought

Simply, the study of the magnetic excitations and hybridization features of 214 cuprates is fascinating. These effects are yet more examples of amazing phenomena that reside in

cuprates. Understanding their implications in full is rewarding both in of itself as well as well as in the context of trying to solve one of the great questions in science today: how do we make a room temperature superconductor? The study and exploration of these dynamic correlations is an experience I will always treasure.

Bibliography

[1] G. L. Squires. *"Introduction to the Theory of Thermal Neutron Scattering"*. Dover Publications, 1978 (cit. on pp. 6–9, 11, 13, 14, 17).

[2] G. Shirane, S. M. Shapiro, and J. M. Tranquada. *"Neutron Scattering with a Triple-Axis Spectrometer"*. Cambridge University Press, 2002 (cit. on pp. 6, 7, 11, 14, 19).

[3] J. J. Wagman. *Neutron Scattering Studies of Underdoped Single Crystal* $La_{2-x}Ba_xCuO_4$. McMaster University, 2010 (cit. on p. 6).

[4] D. Griffiths. *Introduction to Elementary Particles, Second Edition Revised*. 2008 (cit. on pp. 6, 8).

[5] *http://www.physics.mcgill.ca/ dominic/papers201x/GdFeAsO*$_J AP_1 15_2 014_1 7D705.pdf$. Taken from the Internet, 2015 (cit. on p. 7).

[6] A. Duncan. *"Neutron Moderation Lab Manual"*. https://www.physics.mcmaster.ca/phys3h03/, 2015 (cit. on p. 8).

[7] R. Shankar. *"Principles of Quantum Mechanics 2nd Edition*. Springer Science+Business Media Inc., 1994 (cit. on pp. 10, 11, 37).

[8] C. Kittel. *"Introduction to Solid State Physics 8th Edition"*. John Wiley and Sons Inc., 2005 (cit. on p. 12).

[9] D. J. Jackson. *Classical Electrodynamics Third Edition*. John Wiley Sons Inc., 1998 (cit. on p. 13).

[10] *https://neutrons.ornl.gov/sites/default/files/Instrument*$_h b3.pdf$. Image taken from the Internet, 2015 (cit. on pp. 18, 19).

[11] *http://www.ncnr.nist.gov/instruments/dcs/*. Image taken from Internet, 2015 (cit. on p. 21).

[12] J. F. Annett. *Superconductivity, Superfluids and Condensates*. Oxford University Press, 2004 (cit. on pp. 30, 37, 38).

[13] J. Bardeen, L. N. Cooper, and J. R. Schrieffer. In: *Phys. Rev.* 108.5 (1957), pp. 1175–1204 (cit. on p. 30).

[14] J.G. Bednorz and K.A. Muller. In: *Z. Phys. B.* 64.189 (1986) (cit. on p. 30).

[15] M. R. Norman. In: *arXiv:1302.3176* (1985) (cit. on pp. 30, 35).

[16] B. Keimer, N. Belk, R. J. Birgeneau, A. Cassanho, C. Y. Chen, M. Greven, M. A. Kastner, A. Aharony, Y. Endoh, R. W. Erwin, and G. Shirane. In: *Phys. Rev. B* 46.21 (1992), pp. 14034–14053 (cit. on pp. 30, 35–38).

[17] N. Doiron-Leyraud, C. Proust, D. Leboeuf, J. Levallois, J.-B. Bonnemaison, R. Liang, D. A. Bonn, W. N. Hardy, and L. Taillefer. In: *Nature* 447 (2007), p. 565 (cit. on pp. 30, 33).

[18] J. J. Wagman, G. Van Gastel, K. A. Ross, Z. Yamani, Y. Zhao, Y. Qiu, J. R. D. Copley, A. B. Kallin, E. Mazurek, J. P. Carlo, H. A. Dabkowska, and B. D. Gaulin. In: *Phys. Rev. B* 88 (2013), p. 014412 (cit. on pp. 31, 52).

[19] J. M. Tranquada. In: *arXiv:cond-mat/0512115* (2005) (cit. on pp. 32, 41).

[20] J. Singleton. *Band Theory and Electronic Properties of Solids*. Oxford University Press, 2001 (cit. on pp. 31, 37).

[21] L. Taillefer. In: *Annual Review of Condensed Matter Physics* 1 (2010), pp. 51–70 (cit. on pp. 31, 37, 39).

[22] Y. Zhao, B. D. Gaulin, J. P. Castellan, J. P. C. Ruff, S. R. Dunsiger, G. D. Gu, and H. A. Dabkowska. In: *Phys. Rev. B* 76.18 (2007), p. 184121 (cit. on pp. 34, 35).

[23] S. Katano, J. A. Fernandez-Baca, S. Funahashi, N. Mori, Y. Ueda, and K. Koga. In: *Physica C* 214 (1993), pp. 64–72 (cit. on p. 35).

[24] P. Böni, J. D. Axe, G. Shirane, R. J. Birgeneau, D. R. Gabbe, H. P. Jenssen, M. A. Kastner, C. J. Peters, P. J. Picone, and T. R. Thurston. In: *Phys. Rev. B* 38.1 (1988), pp. 185–194 (cit. on p. 35).

[25] M. Fujita, K. Yamada, H. Hiraka, P. M. Gehring, S. H. Lee, S. Wakimoto, and G. Shirane. In: *Phys. Rev. B* 65.6 (2002), p. 064505 (cit. on p. 35).

[26] Chul-Ho Lee, Kazuyoshi Yamada, Yasuo Endoh, Gen Shirane, R. J. Birgeneau, M. A. Kastner, M. Greven, and Y-J. Kim. In: *Journal of the Physical Society of Japan* 69.4 (2000), pp. 1170–1176 (cit. on pp. 35, 39).

[27] J. M. Tranquada, D. E. Cox, W. Kunnmann, H. Moudden, G. Shirane, M. Suenaga, P. Zolliker, D. Vaknin, S. K. Sinha, M. S. Alvarez, A. J. Jacobson, and D. C. Johnston. In: *Phys. Rev. Lett.* 60.2 (1988) (cit. on p. 35).

[28] N. S. Headings, S. M. Hayden, R. Coldea, and T. G. Perring. In: *Phys. Rev. Lett.* 105 (2010), p. 247001 (cit. on pp. 38, 40).

[29] S. Blundell. *"Magnetism in Condensed Matter*. Oxford University Press, 2001 (cit. on pp. 38, 40).

[30] R. Coldea, S. M. Hayden, G. Aeppli, T. G. Perring, C. D. Frost, T. E. Mason, S.-W. Cheong, and Z. Fisk. In: *Phys. Rev. Lett.* 86 (23 2001), pp. 5377–5380 (cit. on pp. 38, 40, 41, 47).

[31] K. Yamada, C. H. Lee, K. Kurahashi, J. Wada, S. Wakimoto, S. Ueki, H. Kimura, Y. Endoh, S. Hosoya, G. Shirane, R. J. Birgeneau, M. Greven, M. A. Kastner, and Y. J. Kim. In: *Phys. Rev. B* 57 (10 1998), pp. 6165–6172 (cit. on p. 38).

[32] K. Machida and M. Ichioka. In: *Journal of the Physical Society of Japan* 68 (1999), pp. 2168–2171 (cit. on p. 38).

[33] N. W. Ashcroft and N. D. Mermin. *Solid State Physics*. Brookes Cole, 1976 (cit. on p. 39).

[34] V. J. Emery and S. A. Kivelson. In: *Nature* 374 (1993), pp. 434–437 (cit. on p. 39).

[35] JM Tranquada, BJ Sternlieb, JD Axe, Y. Nakamura, and S. Uchida. In: *Nature* 375.6532 (1995), pp. 561–563 (cit. on p. 39).

[36] S. R. Dunsiger, Y. Zhao, B. D. Gaulin, Y. Qiu, P. Bourges, Y. Sidis, J. R. D. Copley, A. Kallin, E. M. Mazurek, and H. A. Dabkowska. In: *Phys. Rev. B* 78.9 (2008), p. 092507 (cit. on pp. 40, 41).

[37] B. Lake, G. Aeppli, K. N. Clausen, D. F. McMorrow, K. Lefmann, N. E. Hussey, N. Mangkorntong, M. Nohara, H. Takagi, T. E. Mason, and A. Scrhoder. In: *Science* 291.1759 (2001) (cit. on pp. 40, 41).

[38] S. R. Dunsiger, Y. Zhao, Z. Yamani, W. J. L. Buyers, H. A. Dabkowska, and B. D. Gaulin. In: 77 (2008), p. 224410 (cit. on p. 40).

[39] S. Sachdev, M. A. Metlitski, and M. Punk. In: *Journal of Physics: Condensed Matter* 24 (2012), p. 294205 (cit. on p. 40).

[40] M. Matsuda, M. Fujita, S. Wakimoto, J. A. Fernandez-Baca, J. M. Tranquada, and K. Yamada. In: *Phys. Rev. Lett.* 101.19 (2008), p. 197001 (cit. on pp. 40–42).

[41] S. M. Hayden, G. Aeppli, H. A. Mook, T. G. Perring, T. E. Mason, S.-W. Cheong, and Z. Fisk. In: *Phys. Rev. Lett.* 76 (8 1996), pp. 1344–1347 (cit. on p. 40).

[42] J. M. Tranquada. In: *AIP Conf. Proc.* 1550 (2013), p. 114 (cit. on pp. 40, 41).

[43] J. M. Tranquada, G. Xu, and I. A. Zaliznyak. In: *Journal of Magnetism and Magnetic Materials* 350 (2014), p. 148 (cit. on pp. 41, 47).

[44] N. B. Christensen, D. F. McMorrow, H. M. Rønnow, B. Lake, S. M. Hayden, G. Aeppli, T. G. Perring, M. Mangkorntong, M. Nohara, and H. Takagi. In: *Phys. Rev. Lett.* 93 (2004), p. 147002 (cit. on pp. 41, 47).

[45] R. J. Birgeneau, C. Stock, J. M. Tranquada, and K. Yamada. In: *Journal of the Physical Society of Japan* 75.11 (2006), p. 111003 (cit. on p. 41).

[46] S. Wakimoto, K. Yamada, J. M. Tranquada, C. D. Frost, R. J. Birgeneau, and H. Zhang. In: *Phys. Rev. Lett.* 98 (24 2007), p. 247003 (cit. on p. 41).

[47] M. Fujita, H. Hiraka, M. Matsuda, M. Matsuura, J. M. Tranquada, S. Wakimoto, G. Xu, and K. Yamada. In: *Journal of the Physical Society of Japan* 81.1 (2012), p. 011007 (cit. on p. 41).

[48] M. Enoki, M. Fujita, T. Nishizaki, S. Iikubo, D. K. Singh, S. Chang, J. M. Tranquada, and K. Yamada. In: *Phys. Rev. Lett.* 110 (2013), p. 017004 (cit. on p. 43).

[49] V. Thampy, M. P. M. Dean, N. B. Christensen, L. Steinke, Z. Islam, M. Oda, M. Ido, N. Momono, S. B. Wilkins, and J. P. Hill. In: *Phys. Rev. B* 90 (2014-09), p. 100510 (cit. on p. 43).

[50] C. Stock, W. J. L. Buyers, R. Liang, D. Peets, Z. Tun, D. Bonn, W. N. Hardy, and R. J. Birgeneau. In: *Phys. Rev. B* 69 (1 2004), p. 014502 (cit. on p. 43).

[51] C. Stock, R. A. Cowley, W. J. L. Buyers, R. Coldea, C. Broholm, C. D. Frost, R. J. Birgeneau, R. Liang, D. Bonn, and W. N. Hardy. In: *Phys. Rev. B* 75 (2007), p. 172510 (cit. on pp. 43, 44).

[52] C. Stock, R. A. Cowley, W. J. L. Buyers, C. D. Frost, J. W. Taylor, D. Peets, R. Liang, D. Bonn, and W. N. Hardy. In: *PRB* 82 (2010), p. 174505 (cit. on p. 43).

[53] O. J. Lipscombe, S. M. Hayden, B. Vignolle, D. F. McMorrow, and T. G. Perring. In: *Phys. Rev. Lett.* 99.6 (2007), p. 067002 (cit. on pp. 43, 45, 47).

[54] B. Vignolle, S.M. Hayden, D.F. McMorrow, H.M. Ronnow, B. Lake, C.D. Frost, and T.G. Perring. In: *Nature* (2007), p. 163 (cit. on pp. 43, 46, 47).

[55] M. Matsuura, M. Fujita, H. Hiraka, M. Kofu, H. Kimura, S. Wakimoto, T. G. Perring, C. D. Frost, and K. Yamada. In: *Phys. Rev. B* 86 (2012), p. 134529 (cit. on p. 47).

[56] J. J. Wagman, D. Parshall, M. B. Stone, A. T. Savici, Y. Zhao, H. A. Dabkowska, and B. D. Gaulin. In: *Phys. Rev. B* 91 (2015-06), p. 224404 (cit. on p. 68).